9-1-2018

# Three-Dimensional Wall Effects in a Scramjet Cavity Flameholder

Evan P. Oren


# Three-Dimensional Wall Effects of a Scramjet Cavity Flameholder

THESIS

Evan P. Oren, 1st Lt, USAF

AFIT/GAE/ENY/MS-18-S-068

**DEPARTMENT OF THE AIR FORCE**
**AIR UNIVERSITY**

***AIR FORCE INSTITUTE OF TECHNOLOGY***

**Wright-Patterson Air Force Base, Ohio**

AFIT/GAE/ENY/MS-18-S-068

# THREE-DIMENSIONAL WALL EFFECTS OF A SCRAMJET CAVITY FLAMEHOLDER

-

THESIS

Presented to the Faculty

Department of Aeronautics and Astronautics

Graduate School of Engineering and Management

Air Force Institute of Technology

Air University

Air Education and Training Command

in Partial Fulfillment of the Requirements for the

Degree of Master of Science in Aeronautical Engineering

Evan P. Oren, B.A.E.

1st Lt, USAF

August 28, 2018

AFIT/GAE/ENY/MS-18-S-068

# THREE-DIMENSIONAL WALL EFFECTS OF A SCRAMJET CAVITY FLAMEHOLDER

-

THESIS

Evan P. Oren, B.A.E.
1st Lt, USAF

Committee Membership:

Maj J. R. Komives
Chair

Dr. D. M. Peterson
Member

Dr. K. C. Gross
Member

Dr. M. D. Polanka
Member

# Abstract

Scramjets, or supersonic combustion ramjets, are a key component for the development of powered hypersonic vehicles. The flameholding strategy used in this engine creates a recirculation region by creating a cavity in one side of the combustor. This highly unsteady region is difficult to interrogate through conventional means. A novel optical observation technique called hyperspectral imaging has been developed to examine the scramjet combustion chamber. The hyperspectral camera is capable of generating an interferogram at hundreds to thousands of wavelengths. These data are integrated across the line-of-sight with no information on three-dimensional (3D) location of origin. A model must be used to extrapolate spatially-resolved two-dimensional (2D) data to a three dimensional domain. With no *a priori* data to inform otherwise, the current model assumes that the scramjet flowfield is uniform in the spanwise direction. This does not agree with understanding of compressible flow theory of shock dominated and turbulent flows. This work simulates a non-reacting scramjet combustor using hybrid Reynolds-Averaged Navier Stokes (RANS)/Large Eddy Simulation (LES). The spanwise character is analyzed through instantaneous and time-averaged statistics. It is shown that the flow is not well approximated as two-dimensional, especially in the cavity where fuel is transported and mixed with air. Complete time histories of spanwise lines were collected and total time-averaged means were compared against 200 $\mu$s windowed means. These time windows correspond with the time it takes the hyperspectral camera to create a single scan. Turbulent time scales are calculated and their ramifications on the collection process of the hyperspectral camera are considered. The viscous-dampened region in the cavity has integral timescales on the order of the collection time of each interferogram.

*To my family and friends, without whom my time at AFIT could not have been a success.*

# Acknowledgements

There are many I would like to thank for their steadfast support through the accomplishment of this thesis. From AFIT's faculty I'd like to thank my advisor, Major Jeffrey Komives, for providing guidance, education, and leadership on both engineering and officership. I would also like to thank Dr. Kevin Gross for expanding my knowledge of experimental physics and supplying the experimental input that helped guide this study. I'd also like to acknowledge my lab mate, Nicholas Marco, for both research-related and friendly conversation. From AFRL, I'd like to thank both Dr. David Peterson for his assistance and advice on the execution of my simulations, as well as Dr. Timothy Ombrello for always being willing to answer questions on the experimental setup and process. I would like to thank the University of Minnesota for the use of US3D, the Department of Defense High Performance Computing Modernization Program for the use of Topaz, and AFRL and AFOSR for the research topic and financial support.

Evan P. Oren

# Table of Contents

Page

# List of Figures

# List of Tables

# List of Symbols

THREE-DIMENSIONAL WALL EFFECTS OF A SCRAMJET CAVITY FLAMEHOLDER

-

# I. Introduction

## 1.1 Supersonic Combustion Ramjets

The advantages offered by hypersonic vehicles is of particular interest to the United States Air Force. A key component for the successful implementation of this goal is reliable air-breathing engines capable of operating at these velocities. Scramjets, or supersonic combustion ramjets, have seen recent significant development[11, 12]. Combustion in a supersonic environment is itself a difficult problem. The chemical times associates with combustion are much longer than the residence time of a practically-sized combustor when the core flow is supersonic, resulting in a very low Damköhler number. The Damköhler number is the ratio of flow time scales to chemical time scales. Some measures must be taken to increase the Damköhler number to achieve continuous combustion. This can either be done by decreasing chemical time scales or increasing flow time scales. The magnitude of changes to chemical time possible are limited in size, so the easier method is to increase the flow time scales. One of the common methods to do this is to recess a cavity off of the core flow to create a recirculation region. A schematic of this concept is shown in Figure 1. Fuel can then either be injected upstream of, or directly into, the cavity in order to start the mixing of fuel and air. A cavity allows constant combustion in the vicinity of unburned fuel provided by the upstream or cavity injection, enabling continuous

combustion to occur.

## 1.2 Hyperspectral Camera

This recirculation region adds a high degree of unsteadiness to the flow, both in the shear layer between the cavity and the core flow, and in the cavity itself. This is a complex environment that requires experimental analysis to fully understand, but interrogation of the internal supersonic flows native to scramjets is difficult for many reasons. Lack of access to the flow area of interest, the durability of *in situ* probes and the unavoidable interference to the flow field these produce all make accurate measurement challenging. Using optical methods avoids several of these issues, but optical methods have their own set of problems. Laser spectroscopy is useful for producing data on mixing and combustion processes, but requires a large, complicated experimental footprint to be spatially-resolved. Infrared (IR) imaging is a simple method useful for providing statistics on radiation in a variety of flow regimes, but does not provide spectral information across all relevant wavelengths. This means IR data is incapable of specifying the major influences on radiative emissions from the combustor cavity.

A measurement technique capable of providing spatially-resolved, wide-band spectra in the cavity with the ease of a point-and-shoot camera is highly desirable. With some understanding of spectroscopy, the data should be immediately useful for analysis of the scene. Information on how the flowfield absorbs, emits, and scatters radiation can be used to both locate reaction species and characterize other scalar fields. A novel measurement technique called Hyperspectal imaging (HSI) attempts to fill this measurement capability gap by combining IR imaging and spectrometry.

The hyperspectral camera (HSC) leverages the use of a Michelson interferometer to create interferograms at every pixel in the frame at hundreds to thousands of

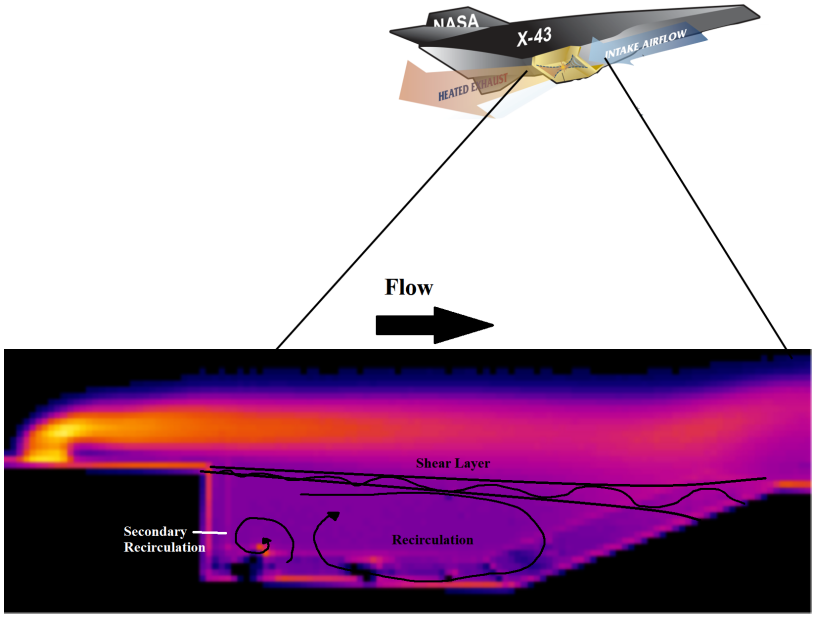


**Figure 1. Image looking spanwise through an example scramjet from a hypersonic vehicle. The scramjet combustor cavity flow direction as shown here is opposite from the orientation of the vehicle.**

wavelengths. The goal is to deconvolve this data into individual radiances (such as in Figure 2), which, with knowledge of values such as temperature and pressure in the cavity, can be used to map concentrations of reactant constituents and gain a better understanding of where and how fuel burns in the scramjet. The challenge is the data produced by a HSC are essentially two-dimensional (2D) line-of-sight integrated measurements of radiant emissions that have passed through, or are sourced from, the cavity. Three-dimensional (3D) understanding of the scramjet is desired, so a model must be used to make inferences on the 3D nature of the flame with data that are spatially resolved in only two dimensions. The assumptions for the current model are shown in Table 1. With no *a priori* data to inform otherwise, one of these assumptions is that the combustor cavity can be approximated as spanwise-homogeneous. The assumption of spanwise homogeneity in this environment does not conform well with knowledge of compressible fluid dynamics and boundary layer theory, especially

when considering the low local Reynolds number environment within the recirculation region of the cavity flameholder. Viscous effects dominate this region over inertial forces, and will likely exhibit large-scale inhomogeneity in the span.

This study will simulate a non-combusting scramjet cavity flameholder, specifically the Air Force Research Lab's (AFRL) research cell 19, using high fidelity Computational Fluid Dynamics (CFD). The combustion chamber and its dimensions are shown in Figure 3. This is the same geometry used in previous studies that targeted simulation suitability and accuracy[6, 8]. This work is an extension to the effort to improve both experimental observations through insight gained from high fidelity CFD and refine the CFD methodology through comparison to experimental measurements. The general techniques for the simulation of this domain have been validated, and non-mixing flow has been analyzed. Injection with no combustion is the next step before progressing to simulations of a burning in a scramjet cavity flameholder.

The data provided by this work will be used to draw conclusions on the following questions:

- Is the spanwise homogeneous assumption used by the experimental model valid?
- Are there specific regions of the domain in which the spanwise homogeneous assumption is valid?
- How do the timescales in the cavity affect the experimental data gathering and processing?
- Are there additional assumptions in the experimental model that are not valid?

Finally, data will be processed that may serve as preliminary *a priori* information required to adapt the model for inhomogeneous conditions in the scramjet combustor.

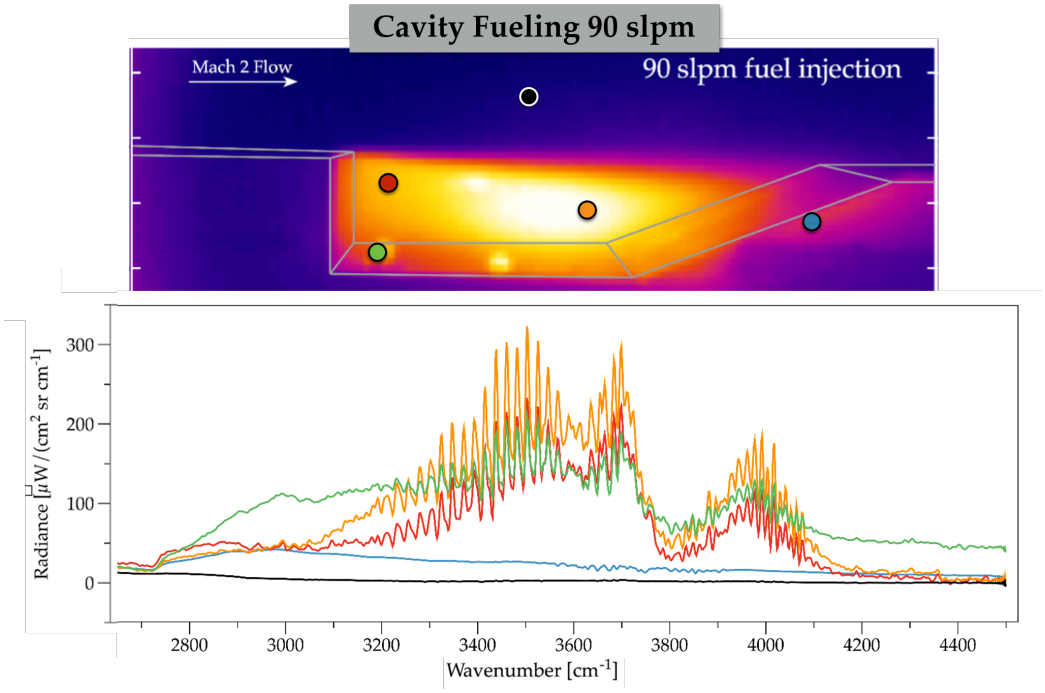


**Figure 2. Radiances plotted against wavenumber captured by the HSC at various points in the cavity[1].**

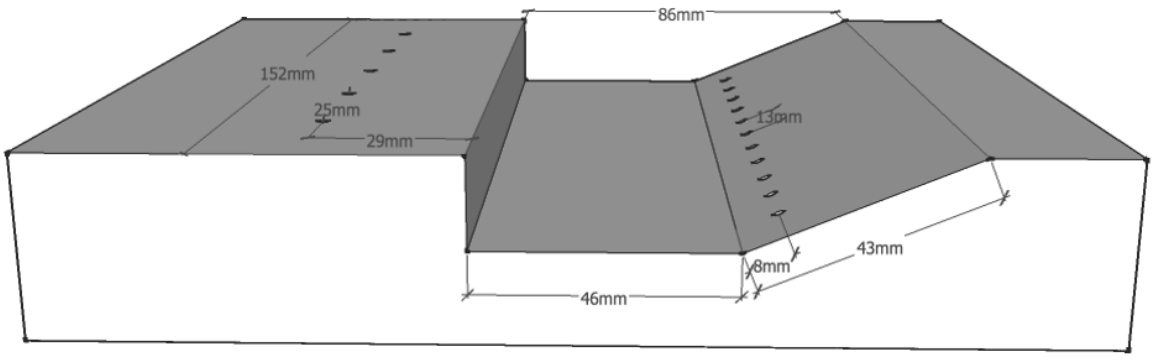


**Figure 3. Combustor section of research cell 19, including the cavity and ramp and the location of the 5 upstream injectors and the 11 cavity injectors on the ramp. The cavity height, h, is 0.0165 meters.**

# II. Literature Review

High supersonic and hypersonic vehicles are a topic of much interest in the aerospace community. These vehicles have many potential applications; weapon systems, space planes, and rapid transport systems being just a few. A whole class of engines designed for high speed combustion, known as scramjets (or supersonic combustion ramjets) have been developed and tested for this purpose of powering these systems. This type of engine comes with its own set of challenges. The highly turbulent flow in scramjet cavity flameholders, combusting or otherwise, is a significant obstacle to better understanding the dynamics of this critical technology. The pattern and magnitude of mixing will directly affect the amount of fuel burned, thrust produced, and the conditions which the engine must contain. One of the many tools currently being developed to assist in understanding this chaotic environment is Large Eddy Simulation (LES). For background information, scramjets concepts and applications are examined and turbulence and turbulence modeling in its many forms are discussed. More in-depth information is given on LES and Hybrid-RANS LES, more specifically the formulation used here (Improved Delayed Detached Eddy Simulation), and its uses and limitations. Along with this is the summary of previous studies on scramjets using various computational tools paired with experimental results. Finally, current developments in flow feature observation and why they motivate accurate three-dimensional simulation techniques is discussed.

## 2.1 Supersonic Combustion and Scramjets

One of the largest roadblocks to high supersonic and hypersonic vehicles is stable combustion at design velocity. Despite often passing through several shocks after entering the vehicle, core flow will still be supersonic and will be too cold for auto-

ignition of most viable fuel-air mixtures. The ability to hold a flame in a regime in which the characteristic flow time is much lower than the characteristic chemical time becomes pivotal in making this technology viable. A rapid increase in volume through use of a cavity causes a recirculation region to form and this can be used to anchor a flame and increase residence times[13]. The fueling of these cavities can be done either passively, through upstream injection, or actively by direct cavity injection[14]. Just creating a recirculation zone is a simple enough concept, but that region must contain a useful mixture of air and fuel as well as temperature hot enough to maintain combustion. To design a cavity and injection strategy that are effective at not only maintaining a recirculation zone, but also continuing combustion requires some understanding of the turbulent environment that exists in this type of flow regime. That requires some knowledge of turbulence and the intelligent selection of tools to interrogate this particular flow.

## 2.2 Turbulence

Understanding the basic physics behind the formation and propagation of turbulence is key to selection of simulation methods, turbulence models, and the analysis of the resulting data. Laminar flow properties can be solved with a high degree of confidence using empirical relations derived from observation of flows and study of the Navier-Stokes equations. Although turbulent flows are also governed by the same equations, the way in which the theory is applied is much different. The velocity field in a turbulent flow is stochastic in nature. This means that its value has a certain degree of unpredictability. However, though the velocity fields in a turbulent flow appear random, there is still recognizable structure. This structure is clearly discernible in Figure 4, which shows the density of the Direct Numerical Simulation (DNS) of a turbulent boundary layer performed by Pirozzoli and Bernardini[2]. The turbulent

structures are shown here to consist of a range of scales, with larger scales giving way to smaller and so on until the turbulence dissipates. This supports the assertion that turbulence is essentially made up of a wide spectrum of energy containing eddies that successively transfer energy down to smaller scales as they decay to heat. This is often referred to as an energy cascade. The energy cascade is a net effect, meaning that instantaneously energy can be transmitted either to larger scales or smaller scales, but will collectively trend towards the smaller scales and eventually dissipation.

**Turbulent Energy Cascade.**

The energy cascade shows the progression of energy transfer from the large scale, energy-containing eddies down to the isotropic and homogeneous Kolmogorov scales[15]. This cascade is divided into three main regions: the energy-containing range, the inertial subrange, and the dissipation range. The energy-containing range is made up of large scale eddies that contain the bulk of the turbulent kinetic energy. The inertial subrange contains the breakdown of large eddies into smaller scales, but where inertial effects still dominate. The dissipation range is viscosity-dominated and where the vast majority of viscous dissipation occurs. Kolmogorov's second similarity hypothesis states that in the inertial subrange and below, turbulent structures have broken down to be universal in form, therefore being independent of the geometry

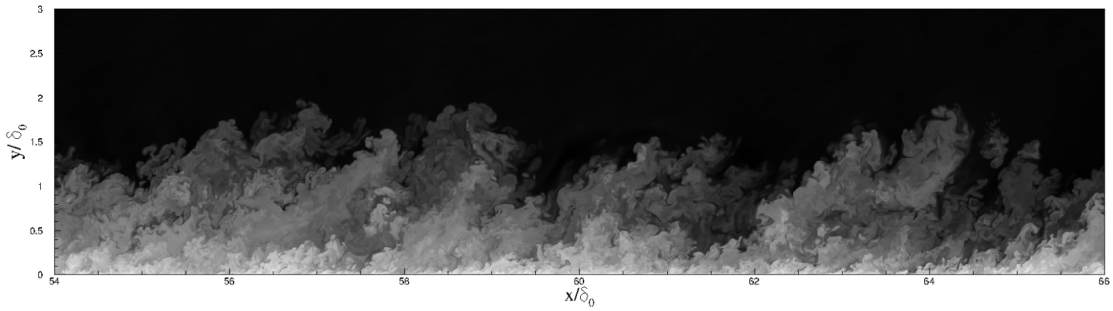


**Figure 4. Density from the Direct Numerical Simulation of a turbulent boundary performed by Pirozzoli and Bernardini.[2]**

and structure of the energy-containing eddies, and are uniquely determined by the rate of energy transfer from larger scales[16]. This is an important assumption that is often leveraged in various turbulence simulation techniques. The energy cascade can be described by:

$$E(K) = C\epsilon^{2/3}K^{-5/3} \tag{1}$$

This shows the energy spectrum being a function only of dissipation rate $\epsilon$ and wave number $K$. This function is shown in Figure 5.

Knowledge of how energy is distributed throughout the length scales of turbulence allows intelligent selection of turbulence models. Understanding which scales are important to resolve and which ones can be modeled for different levels of model fidelity is critical when considering the methodology behind high fidelity CFD.

**Wall-bounded Turbulence and the Law of the Wall.**

One characteristic of turbulence is that as the flowfield approaches a wall, the fluctuations become more restricted in size. The large energy containing eddies become accordingly smaller and the viscous dissipation increases as a function of proximity to the wall[17]. In the near-wall region, the turbulent boundary layer solution can actually be broken into two parts. These parts are the viscous sublayer and the logarithmic layer. The defect layer is not represented by either part of the universal law of the wall. The viscous sublayer is the closest section of the boundary layer to the wall and is described in Equation 2. This, and the related equations in this section, are valid for the time-averaged flowfield.

$$u^+ = y^+ \tag{2}$$

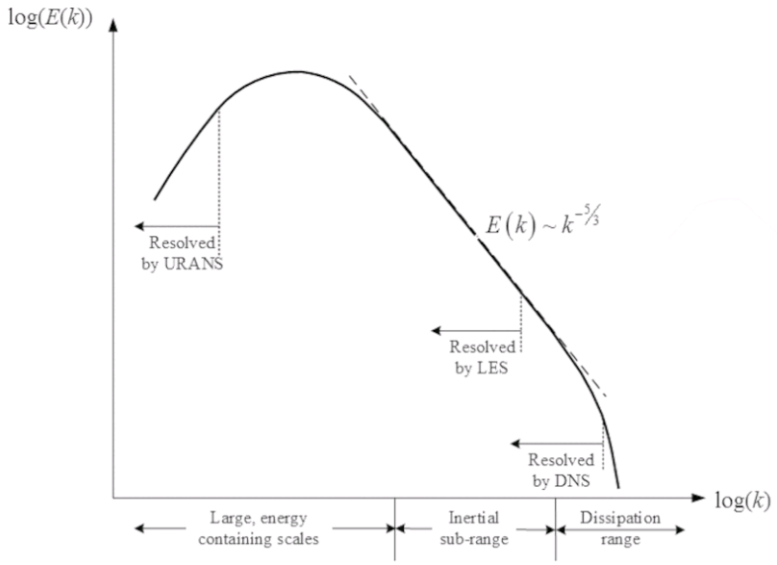


**Figure 5. A typical example of the energy cascade for turbulence[3].**

where $u^+$ is the dimensionless wall velocity calculated by:

$$u^+ = \frac{u}{u_\tau} \tag{3}$$

where $u_\tau$ is called the shear velocity. Shear velocity is given by taking the square of the wall shear divided by the density, as in Equation 4.

$$u_\tau = \sqrt{\frac{\tau_w}{\rho}} \tag{4}$$

The dimensionless wall distance, $y^+$, is non-dimensionalized by the shear velocity and the kinematic viscosity, $\nu$, as shown in Equation 5.

$$y^+ = \frac{y u_\tau}{\nu} \tag{5}$$

The log layer is described by the logarithmic law of the wall. This is a self similar solution where shear stress is approximately constant throughout the boundary layer but it is far enough from the wall where direct viscous forces are negligible[18]. This

logarithmic law is empirically determined and is given in Equation 6.

$$u^+ = \frac{1}{\kappa} \ln y^+ + C \tag{6}$$

where $\kappa$ is the von Karman constant, and is equal to about 0.41. $C$ is an empirically-calculated constant but is usually about 5.1.

There exists a buffer layer between the viscous sublayer and the log layer where neither solution exactly captures the behavior of the boundary layer, but instead it is more similar to a blend of the two. This is shown clearly in Figure 6 and typically occurs around $y^+ = 10$.

### 2.3 Turbulence Modeling

Ideally, Direction Numerical Simulation (DNS) would be used to obtain the most accurate solution possible using the Navier-Stokes equations. This requires the resolution of all energy containing scales at all locations in the entire domain. With the computational cost of DNS scaling approximately with $Re^{\frac{9}{4}}$ this quickly becomes intractable for anything but the most simple aerodynamics problems[19]. Spalart et al. estimated that, assuming Moore's law holds, the earliest DNS of a whole aircraft body will be possible is 2080[20]. This obligates other, more tenable methods to solve practical aerodynamic problems. The opposite end of the turbulence modeling spectrum from DNS is using the Reynolds-averaged Navier-Stokes (RANS) equations. In short, RANS is a temporal average of the flow, where a model is used to take into account the unsteady effects so only the mean flow needs to be fully resolved. The key is the Reynolds decomposition which separates the expected values of a a quantity (in this case the temporal mean) from any fluctuations away from this expected value:

$$u = \bar{u} + u' \tag{7}$$

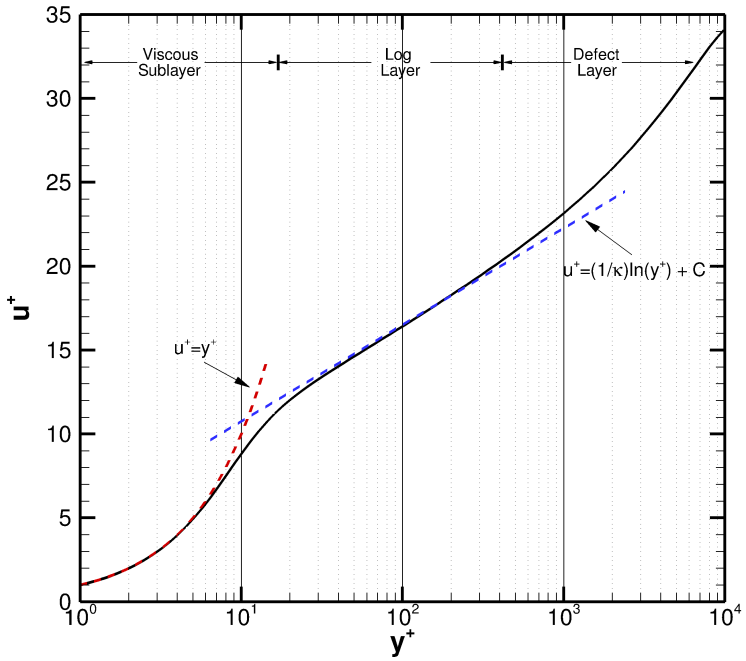


**Figure 6. Typical velocity profile and the Law of the Wall[4].**

The result is the ability to solve for the time-averaged values separately from the fluctuating values. Substituting the Reynolds decomposition back into the original Navier-Stokes equations results in the aforementioned RANS equations, which have several new unclosed terms. One of these is $\rho\overline{u_i'u_j'}$. This is known as the Reynolds stress, and it is the component of the total stress tensor that accounts for the turbulent fluctuations in momentum. These new terms pose new challenges, as there are no longer enough equations to solve for every unknown, so either as many equations as new terms must be added to compensate, or approximations must be made to reduce the number of equations required. Additionally, any new equations used to close the new terms must be model equations, as first principles cannot yield any new equations alone. Usually some combination of these two is used, along with knowledge of the flow in question, to model this Reynolds stress. The ultimate results is a vast reduction of the computational cost, but the solution is a heavy function of the model

used. Each model must be selected and tuned carefully for the problem to which it is being applied.

LES lies in the middle ground between DNS and RANS. The large, energy-containing eddies are fully resolved while the smallest are modeled. LES still experiences many of the same limitations as DNS; however, the effects are much reduced and the relatively small grids allow the method to simulate much larger problems typically seen in research applications. Though pure LES on some complex domains has been made possible through the constant, exponential increase in computational power, Pope asserts that the most challenging applications will still lack the necessary computational power[21]. Some Hybrid RANS/LES methods have been developed to further reduce the computational expense, and these are discussed below. A breakdown of the "hierarchy" of turbulence modeling is shown in Figure 7. Simulation fidelity decreases as level increases on the chart. Direct Numerical Simulation is the highest fidelity solution of the Navier-Stokes equations, where all turbulence scales are resolved. Moving further down the chart means more and more of the smaller scales are modeled instead of resolved. Hybrid RANS/LES methods would be placed between Levels 1 and 2.

**Large Eddy Simulation (LES).**

LES leverages the assumption that only the largest scales of turbulent fluctuations need be resolved because the small scales are universal in nature[5]. This universality allows these small scales to be modeled far more accurately. The use of LES also assumes that most of the Reynolds stresses that characterize turbulent flow are carried by the large scale eddies[4]. Properly executed LES can be expected to be more accurate than a RANS simulation for any regime where unsteadiness is a factor, but cost significantly less than DNS[16].

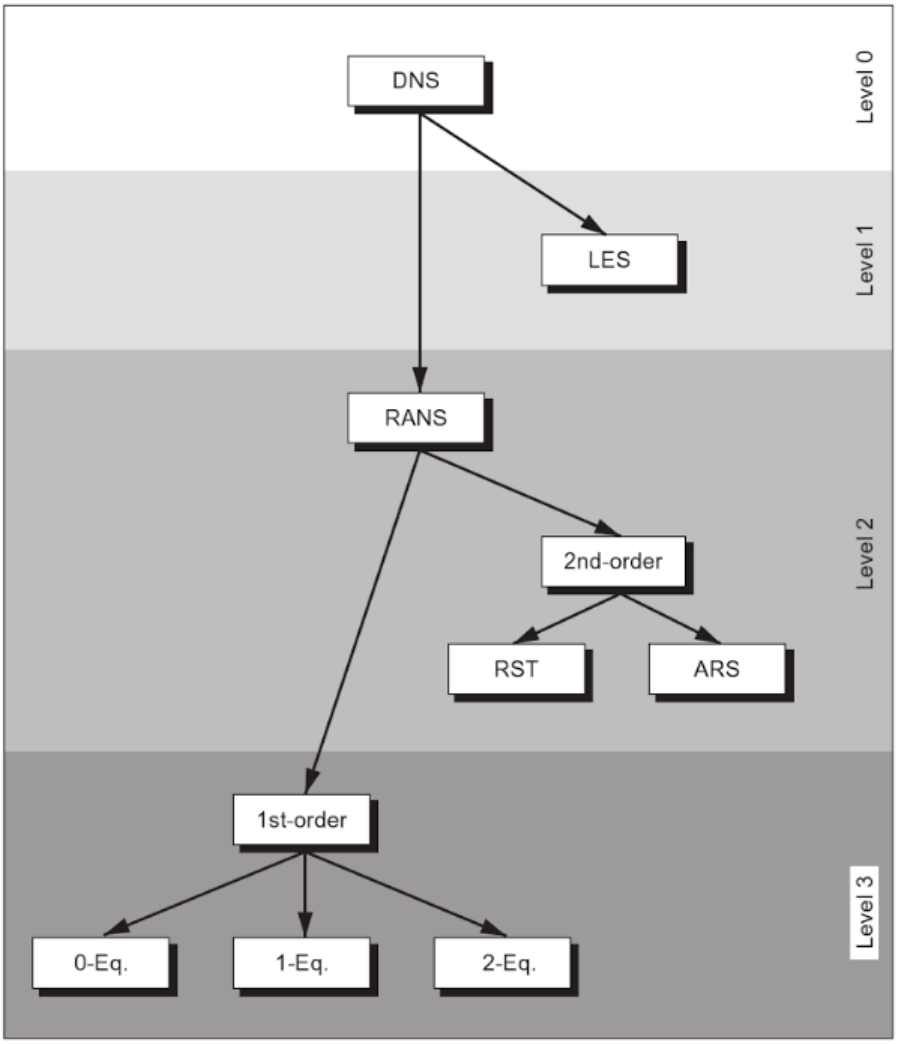


**Figure 7. Hierarchy of turbulence models. Fidelity decreases with increasing levels.[5]**

**Mathematical Formulation of LES.**

The Navier-Stokes (NS) equations written in divergence form is shown in Eq. (8),

$$\frac{\partial U}{\partial t} + \frac{\partial F_1}{\partial x_1} + \frac{\partial F_2}{\partial x_2} + \frac{\partial F_3}{\partial x_3} = 0 \tag{8}$$

where U is the vector of conserved variables and $F_j$ are the flux vectors.

$$U = \begin{pmatrix} \rho \\ \rho u_1 \\ \rho u_2 \\ \rho u_3 \\ E \end{pmatrix}, F = \begin{pmatrix} \rho u_j \\ \rho u_1 u_j + p\delta_{1j} - \sigma_{1j} \\ \rho u_2 u_j + p\delta_{2j} - \sigma_{2j} \\ \rho u_3 u_j + p\delta_{3j} - \sigma_{3j} \\ (E+P)u_j - \sigma_{kj}u_k - q_j \end{pmatrix} \tag{9}$$

where the heat flux vector, $q_j$, and the viscous stress tensor, $\sigma$, are given by

$$q_j = \hat{\kappa}\frac{\partial T}{\partial x_j} \tag{10}$$

$$\sigma_{ij} = 2\hat{\mu}S_{ij} + \lambda\frac{\partial u_k}{\partial x_k}\delta_{ij} \tag{11}$$

Here $S_{ij}$ is the rate of strain tensor and is defined as

$$S_{ij} = \frac{1}{2}\left(\frac{\partial u_i}{\partial x_j} + \frac{\partial u_j}{\partial x_i}\right) \tag{12}$$

and $\lambda$ is the bulk viscosity, given by the Stokes hypothesis to be

$$\lambda = -\frac{2}{3}\mu \tag{13}$$

The equation of state used with this formulation of the NS equations is written as

$$p = \rho RT \tag{14}$$

and the expression for pressure with respect to energy is given by

$$p = (\gamma - 1)\rho\left[E - \frac{u_i u_i}{2}\right] \tag{15}$$

**Spatial Filter.**

LES breaks all variables into two parts: a filtered part, $\overline{U}$, and a sub-filter part given by $U$'. The filtered part represents the low-frequency large eddies that will ultimately be resolved by the LES. The sub-filter portion contains the high-frequency turbulent content that is ostensibly isotropic and homogeneous enough to be modeled with minimal error. These two parts can be combined with a simple sum:

$$U = \overline{U} + U' \tag{16}$$

This division of flow variables is accomplished through a spatial filter[5]. This filtering is done through Eq. (17).

$$\overline{U}(\vec{r}_0, t) = \int \overline{U}(\vec{r}, t) G(\vec{r}_0, \vec{r}, \Delta) d\vec{r} \tag{17}$$

where $G$ is the filter function and $\Delta$ is the filter width, given by:

$$\Delta = (\Delta_1 \Delta_2 \Delta_3)^{1/3} \tag{18}$$

$\Delta_j$ is the filter width in the $j$-th direction. Any scales above this filter width are to be resolved by the LES, while any below this filter width are known as sub-grid scales (SGS) and will be modeled.

Favre, or density-weighted, averaging should be applied in conjunction with the

spatial filter if the Compressible NS equations are to be solved with LES. This type of averaging specifically targets fluctuations in density. This results in the $U$ vector being decomposed into

$$U = \tilde{U} + U'' \tag{19}$$

where $\tilde{U}$ is the vector of Favre-averaged terms, which can be shown as:

$$\tilde{U}(\vec{r}_0, t) = \frac{\overline{\rho U}}{\overline{\rho}} = \int \rho(\vec{r}, t) U(\vec{r}, t) G(\vec{r}_0, \vec{r}, \Delta) d\vec{r} \tag{20}$$

and $U''$ is the vector of fluctuating values. This results in a group of Favre-averaged shear and heat flux terms as well as a term for the divergence of SGS heat flux, the divergence of SGS heat diffusion, SGS pressure-dilatation and SGS viscous dissipation.

Thanks to the works of Smagorinsky, Schumann, Vreman, Deardorff, and Lilly, there are many ways to model the SGS stresses that are not resolved[22, 23, 24, 25, 26]. As discussed earlier, the turbulence scales resolved by LES shrink near the wall and the resolution required to resolve them can be restrictive. Methods around this issue are discussed below.

**Detached and Delayed Detached Eddy Simulation (DES & DDES).**

In 1997, Spalart et al. evaluated the suitability of wall-resolved LES (WR-LES) for practical engineering problems and found that the resolution requirements for objects with multiple surfaces, and therefore multi-directional boundary layers, are too restrictive for the day's computational capabilities[20]. This is still true for many types of problems, especially in shock-dominated compressible flows with massive separation and wall-bounded turbulence (such as a scramjet cavity flameholder). The

main hurdle for WR-LES is that this type of simulation needs high enough resolution to resolve the high-speed inward motion of eddies as well as the low-speed mass ejections of the eddy content near the wall[27]. As Reynolds number and proximity to the wall increase, these features get smaller and more difficult to resolve. This motivated the formulation of Detached Eddy Simulation (DES), a type of hybrid RANS/LES in which RANS is used to model the boundary layer while LES handles the separated regions[28].

The key concept behind the formulation of DES is using a RANS turbulence model as the SGS model of LES. While not strictly required, the SA model was used in the original formulation of DES and the method selected for this study uses a form of SA. For these reasons, any further discussion of DES or its subsequent developments will use the SA model as an example.

RANS models leverage the Boussinesq approximation to estimate the effect of turbulence as effectively just an increase in momentum diffusion. This is enumerated in the eddy viscosity term, $\widetilde{\nu}$. If the RANS length scale for wall distance is replaced with something that is proportional to $\Delta$, it can be shown that the eddy viscosity is proportional to the product of $\Delta^2$ and the rate of strain tensor, $S_{ij}$ when turbulence production and destruction are balanced. Specifically for SA, $\widetilde{d}$ replaces $d$ in the SA eddy viscosity destruction term such that:

$$\widetilde{d} \equiv \min(d, C_{DES}\Delta) \tag{21}$$

As $d \to 0$, $\widetilde{d}$ becomes $d$ and SA is used as a RANS model, but when $\Delta \ll d$, then it is used as a SGS model. Traditionally, $\Delta$ is defined as the largest grid spacing in any direction, or:

$$\Delta \equiv \max(\Delta_x, \Delta_y, \Delta_z) \tag{22}$$

This works because grids in the near-wall region are usually highly anisotropic, where ultimately $d \ll \Delta$. The result is that switching between SA-RANS and LES with SA as the SGS model is determined solely by the grid. In highly refined grids, this can become an issue as this method experiences non-physical activation of the LES in the boundary layer. This occurs commonly in shallow separations or areas of high grid density[29]. When the latter occurs, it is known as grid-induced separation.

$$r \equiv \frac{\nu_t}{S\kappa^2 d^2} \tag{23}$$

The issue of improper model toggling leads to the formulation of Delayed Detached Eddy Simulation (DDES). The solution to ensuring the use of RANS inside, and only inside, the boundary layer is to have a switch based on the locations of the edge of the boundary layer[30]. One equation models, such as SA, do not have an internal length scale that can be used to find the boundary layer edge, however SA has an intermediate parameter, $r$, that relates the model length scale to distance from the wall and shown en. The parameter $r$ can be modified to a *delayed* $r_d$ such that:

$$r_d \equiv \frac{\widetilde{\nu}}{\sqrt{U_{i,j}U_{i,j}\kappa^2 d^2}} \tag{24}$$

The new parameter $r_d$ is then used in the switching function:

$$f_d \equiv 1 - \tanh([8r_d]^3) \tag{25}$$

This function is designed to be 1 when $r_d \ll 1$ (or regions clearly outside the boundary layer) and 0 everywhere else in addition to being insensitive to $r_d > 1$ in the near wall region. This is then implemented through the DES wall distance limiter $\widetilde{d}$ through:

$$\widetilde{d} \equiv d - f_d \max(0, d - C_{DES}\Delta) \tag{26}$$

This ensures that LES is not used in regions of ambiguous grid sizing where the required cell density to resolve the eddy content is not guaranteed.

**Improved Delayed Detached Eddy Simulation (IDDES).**

With the continual improvement of computational power, resolving more of the energy-containing eddies becomes more tractable as time progresses. This motivates the use of DES as a wall-layer model for LES as opposed to using RANS to model the whole boundary layer. The increased resolution closer to the wall allows more complete capturing of the small, but vital, near-wall dynamics; however, an issue presents itself now that two different models are used inside the boundary layer. The result is a mismatch inside the logarithmic-layer as the two models don't return the same answer. This log-layer mismatch can contribute as much as a 10-15% mis-prediction in skin friction[31]. Shur et al. proposed a modification to DDES known as Improved Delayed Detached Eddy Simulation, or IDDES[32] to address this issue. IDDES employs the use of a "branch" that is specifically designed operate as Wall-Modeled LES (WMLES) if there is a significant region of resolved fluctuations. It blends the RANS and LES length scales together with:

$$l_{\text{WMLES}} = f_{\text{B}}(1 + f_e)l_{\text{RANS}} + (1 - f_{\text{B}})l_{\text{LES}} \tag{27}$$

where $f_B$ is the new blending function used to smoothly combine the RANS and LES in the boundary layer. This blending function is defined as:

$$f_{\text{B}} = \min[2\exp(-9\alpha^2), 1.0], \alpha = 0.25 - d_w/h_{\max} \tag{28}$$

In addition to the blending between the RANS and LES solutions, there is also a "elevating-function," $f_e$, to prevent over-reduction of the Reynolds stresses in the

RANS model when the RANS and LES models are blended[32]. The function is passive in two situations. The first is when the grid is already suitable for full WR-LES. The second being when the final blended IDDES model "effectively performs as the background RANS model[32]." The final IDDES model is a result of blending the WMLES and the DDES branches. This is done through another blending function that is essentially a modification of the blending function from DDES.

$$\widetilde{f}_{\mathrm{d}} = \max[1 - f_{\mathrm{dt}}, f_{\mathrm{B}}] \tag{29}$$

Where,

$$f_{\mathrm{dt}} = 1 - \tanh((8r_{\mathrm{dt}})^3) \tag{30}$$

The final blending function is implemented in another length-scale combination, this time between DDES and WMLES scales.

$$l_{hyb} = \widetilde{f}_{\mathrm{d}}(1 + f_e)l_{\mathrm{RANS}} + (1 - \widetilde{f}_{\mathrm{d}})l_{\mathrm{LES}} \tag{31}$$

### 2.4 Past Scramjet Simulations

Many simulations have been performed of scramjet cavity flameholders and with the goal of gaining insight into the mechanics of the flowfield. Better models can be developed when experimental data is used to refine assumptions and model selection.

Peterson and Hassan[6] simulated reacting and non-reacting flow through the flameholder using the same type of Hybrid/RANS LES method used in this study, IDDES. The results were then compared to Particle Image Velocimetry (PIV) data for two velocity components to verify flow structure agreement. Also examined were measurements of fuel concentration obtained through Laser-Induced Break-down Spectroscopy (LIBS), and heat release distribution through path-integrated chemilumi-

nescence. The computational mesh was formed using a periodic domain. Peterson and Hassan reported overall good qualitative agreement with velocity field values from PIV for both the reacting and non-reacting case, as shown in Figure 8. Similarly, the simulated values of fuel concentration displayed close visual similarity to observed experimental values for the non-reacting case; however, more uncertainty was shown when considering the reacting case. Likewise, reasonably comparable results are shown when examining experimentally-obtained chemiluminescence and heat release from the simulation.

Baurle[7] implemented a high fidelity scale-resolving hybrid RANS/LES model to fine tune the use of a RANS simulation in order to strive for better agreement between simulated and experimental results. These were then compared to velocity fields obtained through PIV and fuel concentration measurements from laser-induced breakdown spectroscopy. Side-wall effects were completely neglected, so the computational grid used for the simulations was a small periodic section extending from the center plane of an injection port to the center of two adjacent ports. This periodic approach is used in many other efforts to date, and is shown in Figure 9. Concerning the PIV data, RANS simulation results generally reflected the experimental data with reasonable accuracy. However, the calculated velocity field was more sensitive to the rate of fueling than was shown by the experimental data, causing a larger deviation

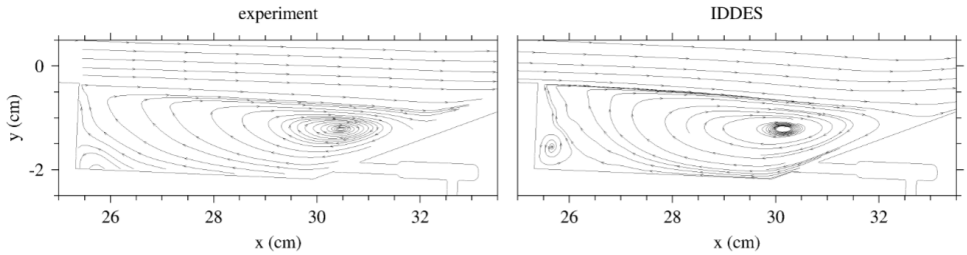


**Figure 8. Streamlines calculated from mean velocity for both the experiments and Peterson's simulations.[6]**

as the fuel mass flow rate was increased.

Peterson and Hassan[8] used a fine-grid Implicit Large Eddy Simulation (ILES) for both the non-reacting and reacting cavity flameholder with a span-wise periodic grid. This was accompanied by a rigorous boundary condition development performed by simulating flat plate flow until similarity solutions for mean velocity and velocity fluctuations are produced and the skin friction matches accepted empirical estimations. In order to reduce computational cost to a reasonable level, Reynolds number was reduced by a factor of 10 from expected experimental values. The results showed that shear layer growth is largely independent of the combustion process and that adding combustion reduces the velocity fluctuations in the vicinity of the cavity floor, shown in Figure 10.

Okhovat[33] collected radiative measurements with an infrared camera in order to characterize the distribution of combustion species. Bandpass filters were then used to determine the spatial distributions of these species during combustion. The experimental data obtained were then compared against a RANS simulation of the cavity flameholder run on a two-dimensional grid with 4.7 million grid points. The author visually showed good agreement between simulated and experimental results for general location of water vapor in the cavity at all fueling rates. Numerically calculated hydrocarbon mole fraction distributions did not show the same good correlation and tended to show little spatial location consistency with the empirical data.

As a general trend, velocity fields were predicted with reasonable quantitative accuracy at the center of the cavity flameholder when a properly refined grid was used with a LES or hybrid RANS/LES method. While qualitative agreement is shown concerning the location and overall distribution of some combustion species, others are inconsistent and cannot be used to effectively investigate the nature of the flowfield. The experimental results show these distributions as levels of measured

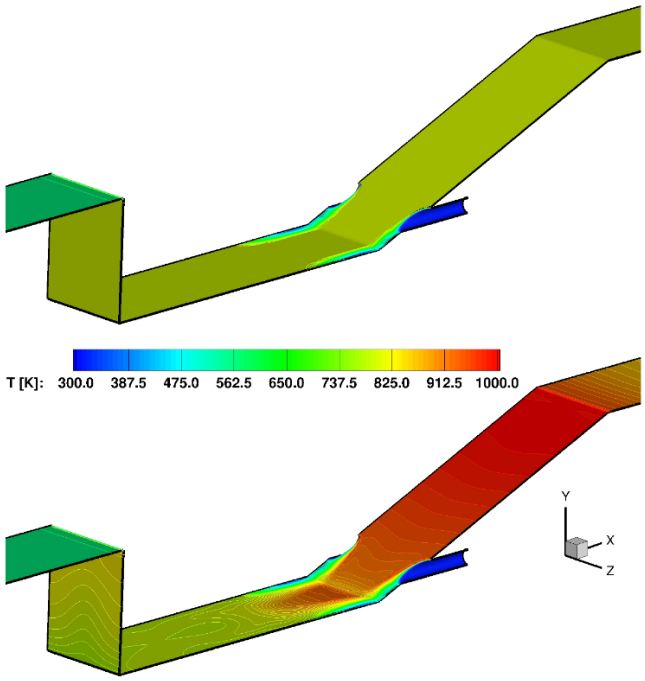


**Figure 9. Surface temperature for two different boundary conditions. Shows the periodic domain used by Baurle and that is similar to many of the other studies done to date[7].**

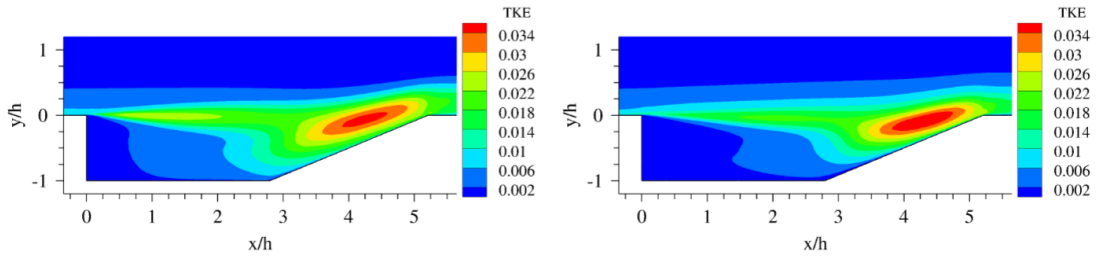


**Figure 10. Time Averaged, Resolved Turbulent Kinetic Energy for both the non-reacting and reacting cases.[8]**

radiance at specific wavelengths. The issue becomes determining the cause in the change in radiance; either an increase in number of radiating particles or an increase in temperature, and therefore an increase in the likelihood that each particle radiates. Temperature then becomes a critical flow property to obtain, as radiation scales with $T^4$.

## 2.5 Hyperspectral Imaging

The collection of information from physical experiments is subject to many restrictions. These include, but aren't limited to, physical access to the flow regime in questions, fragility of the sensor required for certain data, or the probe's direct interference with, and therefore alteration of, the flow being examined. Supersonic and hypersonic flows are even more difficult as the facilities required to contain high speed flows often exacerbates these issues.

This motivates the development of optical measurement techniques to avoid or mitigate these restrictions, but these methods have their own limitations. Usually these limits are with the nature of the data that can be gathered with each method. Particle Imaging Velocimetry (PIV), such as that done by Tuttle et al., leverages seed particles to map the velocity in two- or three-dimensional vector fields; however, usually velocity is the only primitive available (sometimes temperature is available)[10]. This means concentrations of reaction constituents are out of reach without the addition of other measurement techniques. Laser-based spectroscopy provides insight into the characteristics of combustion and mixing by providing broadband spectra, but requires a prohibitively-complex setup to procure the spatially-resolved data to shed insight on the turbulent characteristics[34, 1], but without wide-band spectrally-resolved data, cannot be used to fully deconvolve the radiation into its source species.

A relatively new method called Hyperspectral Imaging (HSI) (device setup shown

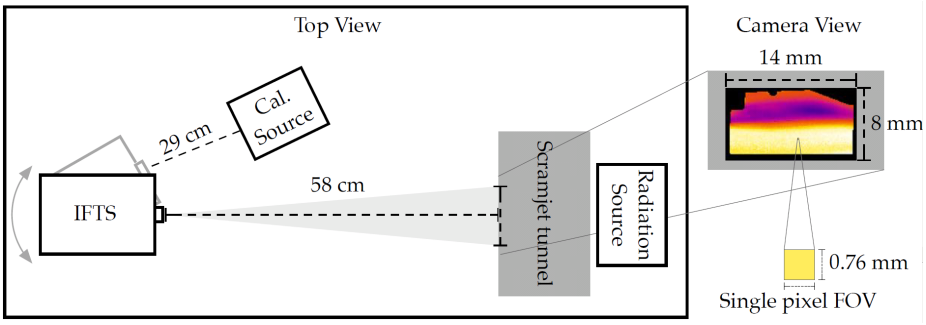


**Figure 11. Schematic of the experiment configuration the Imaging Fourier Transform Spectrometer. The blackbody radiation source used to calibrate the camera is labeled "Cal. Source" and "Radiation Source" is the blackbody source used when taking absorption measurements[9].**

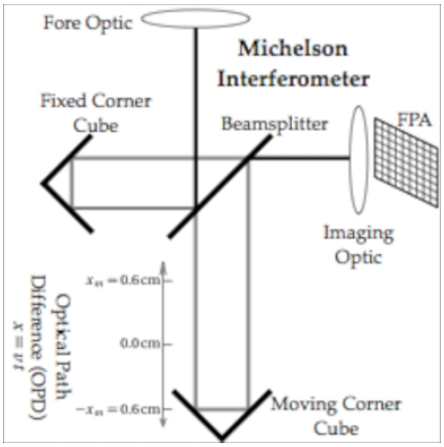


**Figure 12. Schematic of Michelson Interferometer as part of the Hyperspectral camera.**

in Fig 11) combines the use of IR imaging with spectroscopy through the coupling of a high speed focal-plane array and a Michelson interferometer, shown in Figure 12. The light collected through the hyperspectral camera (HSC) aperture is split and reflected back to an intersection by two mirrors. One of these mirrors is on a track and moves to cause different parts of the intersecting light waves to interfere. This creates data that are stored as a block constituted of images taken at hundreds to thousands of wavelengths. A high fidelity, spatially resolved, wide-band spectra image block can be recorded with a single measurement. Simply put, the camera creates an interferogram at every pixel. A Fourier transform allows the extraction of informa-

tion such as the chemical concentrations, radiant intensity, and emissivity of the gas. In addition, a high frequency, broadband IR capture allows the use of more traditional flow diagnostics, such as PIV, to gain information on bulk flow and turbulent statistics. This method has been used to examine smokestack emissions[35], laminar flames[36], a subsonic turbulent flame[37], and most recently a preliminary investigation of the scramjet cavity flameholder of interest to this study[9]. Figure 13 shows a diagram of the hyperspectral camera and two example pixels from the scramjet flameholder on the left[38]. On the right are the interferograms plotted across the Optical Path Difference (OPD) that are the direct result from the Michelson interferometer component. One interferogram is produced at every pixel for every complete scan through the OPD. Spectral resolution is increased or decreased by increasing or decreasing the length of the OPD. The spectra resulting from the Fourier transform of the interferograms are shown plotted across the number of sample points along the OPD.

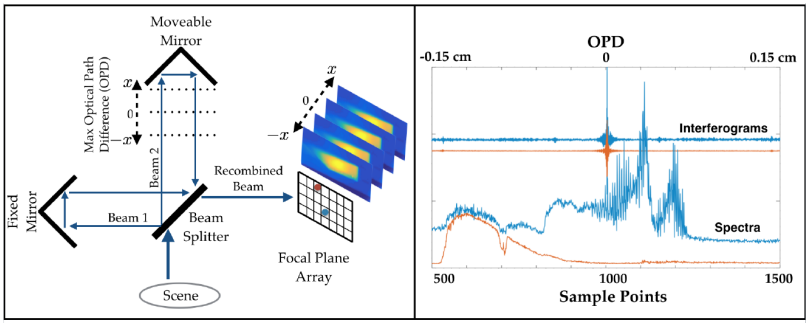


**Figure 13. Left: Diagram depicting the camera setup with the Optical Path Difference (OPD) and two example pixels. Right: Interferograms and resultant spectra from the Fourier transform.**

The broad band spectral data generated in the manner described above are spatially resolved in two dimensions. The data are used to extract flow features such as temperature and species concentrations; however, just as with much of CFD, the solution is a heavy function of model selection. The assumptions of the current model are shown in Table 1. A more detailed breakdown of these assumptions is shown in

Figure 14. A full scan with the HSC takes a few seconds, so it is assumed that the flowfield is statistically stationary. The three-dimensionality of the windows is neglected and instead they are assumed to be uniform and any background radiation is assumed to be negligible.

**Table 1. HSI Modeling Assumptions**

| | |
|---|---|
| 1 | Assume the scene is temporally constant. |
| 2 | Treat flow as two-dimensional in nature. |
| 3 | Window transmission effects simplified. |
| 4 | Ignore background and outer back window. |
| 5 | Treat front window as single temperature. |

Figure 14 shows the breakdown of the total radiance, $L$, into contributions from the calculated spectral radiances from multiple sources along the path of observation. Each spectral radiance calculation is based on a measured $\epsilon$. The flame's spectral radiance is calculated using a single value for temperature, which is assumed to be uniform across the cavity. This does not agree with understanding of compressible flow theory and turbulence. The photons collected by the HSC must pass through at least one sidewall boundary layer, as well as any turbulent features in between that are not accurately estimated as two-dimensional.

To get an idea of how this assumption may effect the interpretation of the hyperspectral measurements, the effect assuming spanwise uniformity on observed transmittance can be examined. Beer's law relates the absorption of electromagnetic radiation to the properties of the medium it is passing through[38]. It states that for one attenuating species the transmission function for some path:

$$\tau = e^{-\int_{s_1}^{s_2} N(s)\sigma ds} \tag{32}$$

where $\sigma$ is the attenuation cross section and $N(s)$ is the path dependent number density of the attenuating fluid (fuel in this example). The spanwise homogeneous

assumption reduces this transmittance equation to:

$$\tau = e^{-N\sigma l} \tag{33}$$

where $l$ is the total span length and the number density is no longer a function of spanwise position. It is important to recognize that $\sigma$ is a function of temperature, making transmittance of the gas a non-linear function of temperature and gas density. Large variations in the spanwise character of temperature, whether through sidewall boundary layers or turbulent structures, will have a disproportionate effect on the transmission of the fuel, and therefore the amount of radiation from the black body source that is observed by the hyperspectral camera. More knowledge of the flow regime's spanwise character is needed to analyze the effect the approximation of spanwise uniformity. High fidelity CFD techniques are of particular use for providing this information because of their ability to examine any and all parts of the domain for all flow properties.

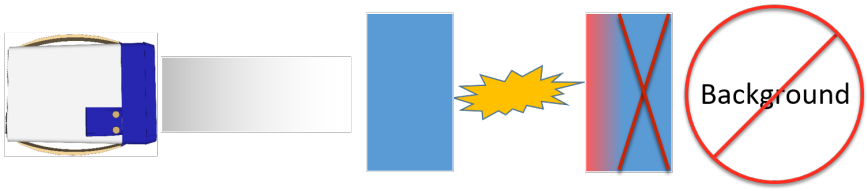


$$L = \tau_{atm}\left[\tau_w\left[\tau_f \varepsilon_w B_w(T_1) + \varepsilon_f B(T_f)\right] + \varepsilon_w B(T_2)\right] + \varepsilon_{atm} B(T_{atm})$$

**Back Window**

$$B_w(\mathbf{T_1}) = \frac{2h\nu^3}{c^2}\frac{1}{e^{h\nu/k_B\mathbf{T_1}} - 1} \qquad \varepsilon_w = \text{measured} \qquad \tau_w = \mathbf{1} - \varepsilon_w$$

**Flame**

$$B(\mathbf{T}_f) = \frac{2h\nu^3}{c^2}\frac{1}{e^{h\nu/k_B\mathbf{T}_f} - 1} \qquad \varepsilon_f = \mathbf{1} - e^{\frac{P}{k_B T_f} l\xi\sigma}$$

**Front Window**

$$B_w(\mathbf{T}_w) = \frac{2h\nu^3}{c^2}\frac{1}{e^{h\nu/k_B\mathbf{T}_w} - 1} \qquad \varepsilon_w = \text{measured}$$

**Atmosphere**

$$B(\mathbf{T}_{atm}) = \frac{2h\nu^3}{c^2}\frac{1}{e^{h\nu/k_B\mathbf{T}_{atm}} - 1} \qquad \varepsilon_{atm} = \text{measured}$$

**Figure 14. Top down view of experimental setup and the total radiance equation used to account for all collected photons at a given pixel.**

# III. Methodology

Most CFD methods follow the same general path of execution. A flow in question through (or over) a designated geometry is chosen. Then, typically through an iterative process, a mesh is created that captures the flow features in the fluid volume. Boundary conditions are set and CFD is performed on the generated grid. Data is collected during each simulation needed and post-processed to result in useful information on the flow in question. This data must be verified before any conclusions can be drawn from examination or comparison of the results. Verification is accomplished through evaluating the suitability of the grid for the problem and ensuring it properly resolves the solution. In addition to grid resolution, timestep resolution is also examined due to the semi-implicit time advancement used in this study.

## 3.1 Geometry and Flow Conditions

The geometry selected for examination is the scramjet flameholder cavity. All experimental data[9, 10] used for comparison purposes in this study comes from AFRL's Research Cell 19, so the geometry used for the simulation matches its configuration. Figure 15 shows the total domain broken into its three major segments, the facility nozzle, the isolator, and the combustor. The domain was created using the computer-aided design software SolidWorks 2016.

Flow conditions were based on nozzle design conditions and inflow of every domain downstream of the nozzle was determined by the previous outflow. The nozzle inflow conditions are shown in Table 2. These conditions result in a unit freestream Reynolds number of about $27 \times 10^6 \frac{1}{m}$, or a $Re_\delta$ of 242,000 based on the boundary layer thickness at the beginning of the combustor of 0.09 cm. This very high Reynolds number is one of the major contributing factors to the very large size of this simulation.

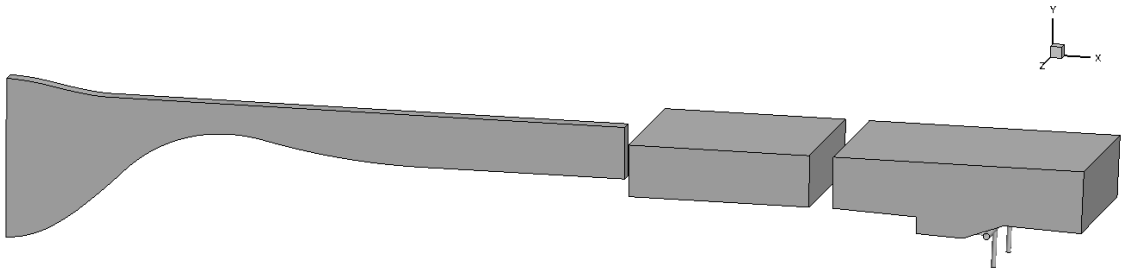

**Figure 15. Total domain from left to right: facility nozzle, isolator, and combustor with plenum.**

**Table 2. Simulation Conditions**

| $T_0$(K) | $P_0$(kPA) | Target Mach | Unit Re (1/m) |
|---|---|---|---|
| 589 | 483 | 2.0 | $27.0\times10^6$ |

### 3.2 Discretization

All computational meshes were created using a combination of Link3D and Pointwise. Link3D is multi-block structured grid design software leveraging the use of topological design combined with a parallel elliptic smoother to produce structured meshes suitable for hypersonic flows. Pointwise is a detailed-focused grid generation software used to merge and modify the grids in this study.

The total simulation mesh was created in four parts: the nozzle, the isolator, the combustor cavity, and the plenum-injector assembly. The combustor cavity was merged with the plenum after both were created using Link3D. A side view of the cavity with wall and shear layer clustering is shown in Figure 16. The entirety of the cavity between the wall clustering and shear layer clustering is made up of isotropic cells. The shear layer has a large effect on the mixing and turbulent character in the cavity so it is very important to resolve.

Figures 17 - 19 show the plenum from multiple angles. Four singularities are used

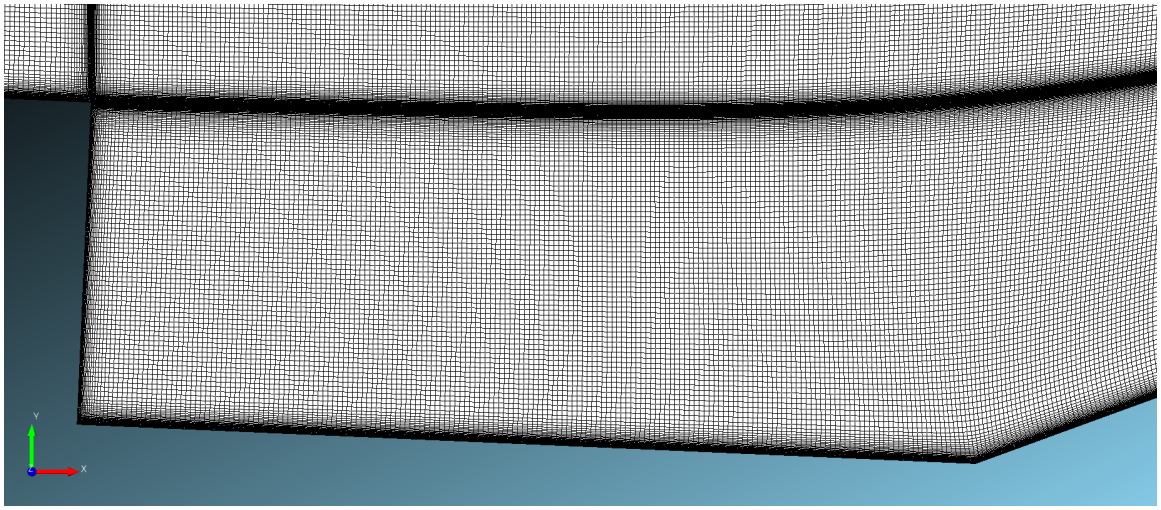

**Figure 16. XY plane of the cavity grid with wall and shear layer clustering.**

to curve the grid lines around the circular segments, such as the inflow and injector tubes, to retain orthogonality on the edges of the circles. The interface between the plenum and the combustor section is shown in Figure 20. Spanwise derefinement and grid stretching is used near the outflow of the cavity, shown in Figure 21, to save computational cost and reduce the influence of the subsonic part of the boundary layer near the wall interacting with the supersonic outflow condition.

A RANS simulation of a half span cavity was completed and used as a basis for expected wall shear values. This knowledge was used to estimate the required spacing for both the isotropic grid spacing and boundary layer resolution. The grid spacings are shown in Table 3 and resultant grid sizes are shown in Table 4. These were chosen based on previous experience and LES community best practices[39, 40].

**Table 3. IDDES Spacing Requirements**

| $y(y^+ = 1)$ | $\Delta x^+$ | $\Delta x$ | $\Delta y^+$ | $\Delta y$ | $\Delta z^+$ | $\Delta z$ |
|---|---|---|---|---|---|---|
| $2.5 \times 10^{-6}$ m | $100\Delta y_1^+$ | $2.5 \times 10^{-4}$m | $100\Delta y_1^+$ | $2.5 \times 10^{-4}$ m | $100\Delta y_1^+$ | $2.5 \times 10^{-4}$ m |

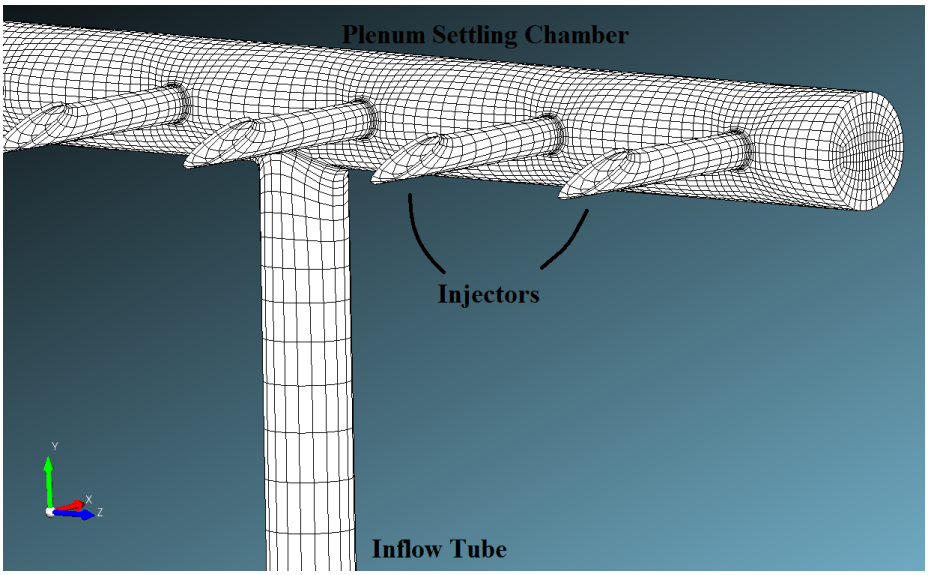


**Figure 17. Isometric image from the upstream side of the plenum.**

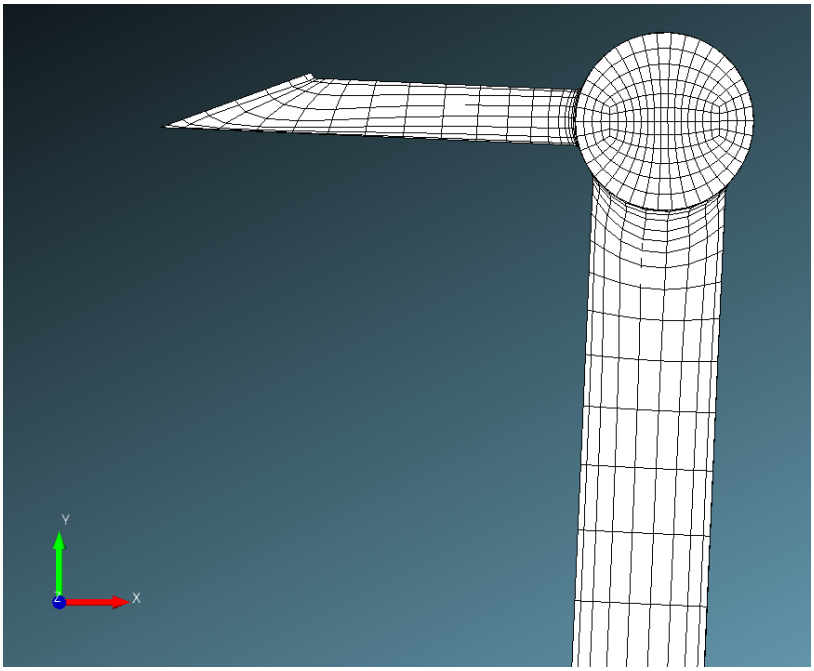

**Figure 18. XY plane of the plenum. Slightly coarsened for clarity.**

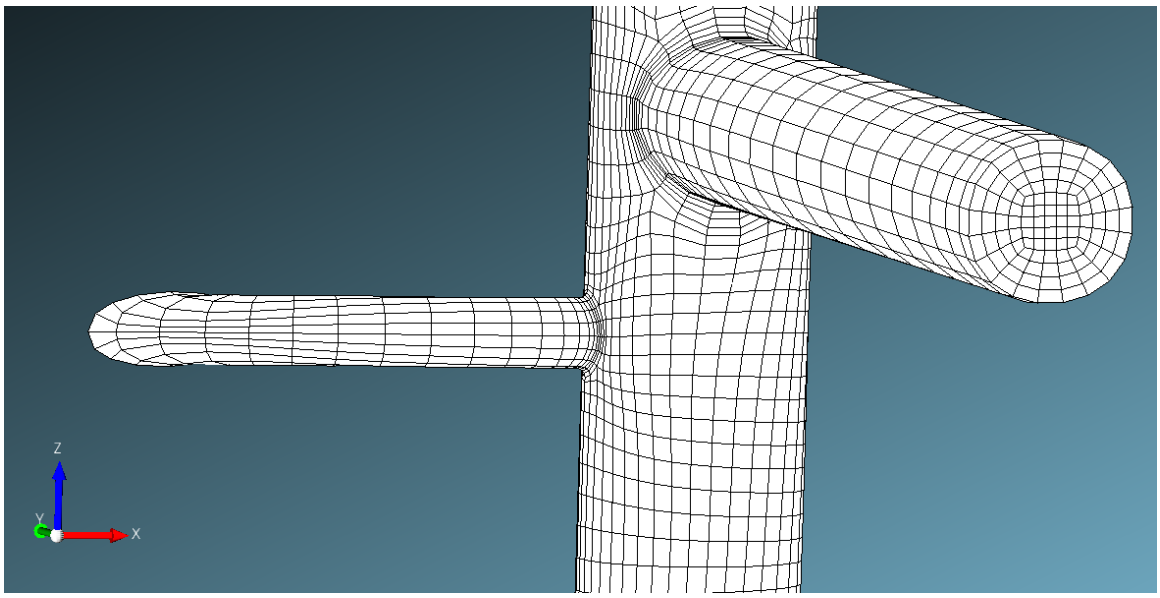


**Figure 19. Image of the plenum from the negative $y$ direction. Slightly coarsened for clarity.**

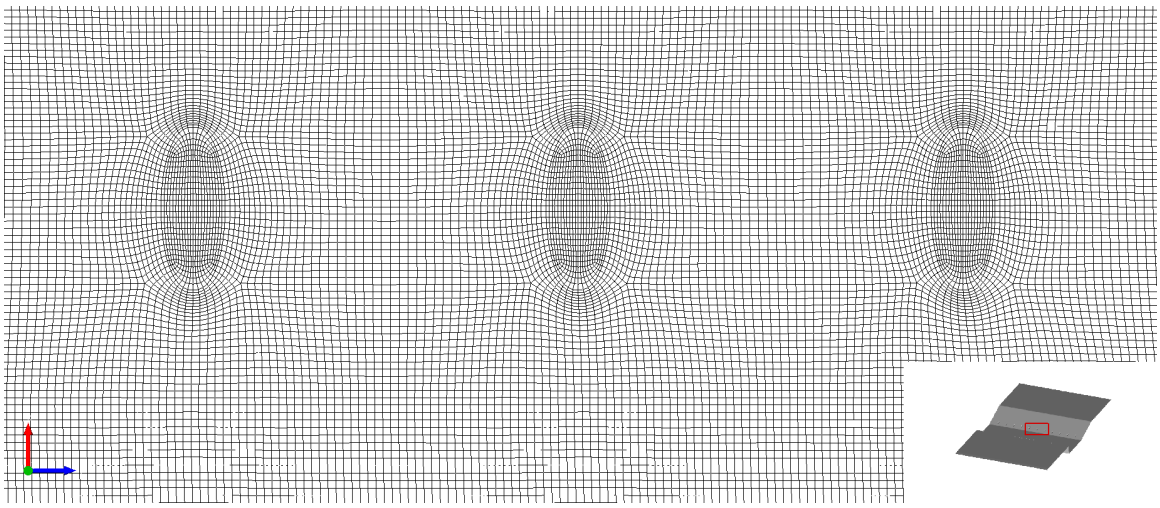

**Figure 20. Injector ports on the surface of the ramp.**

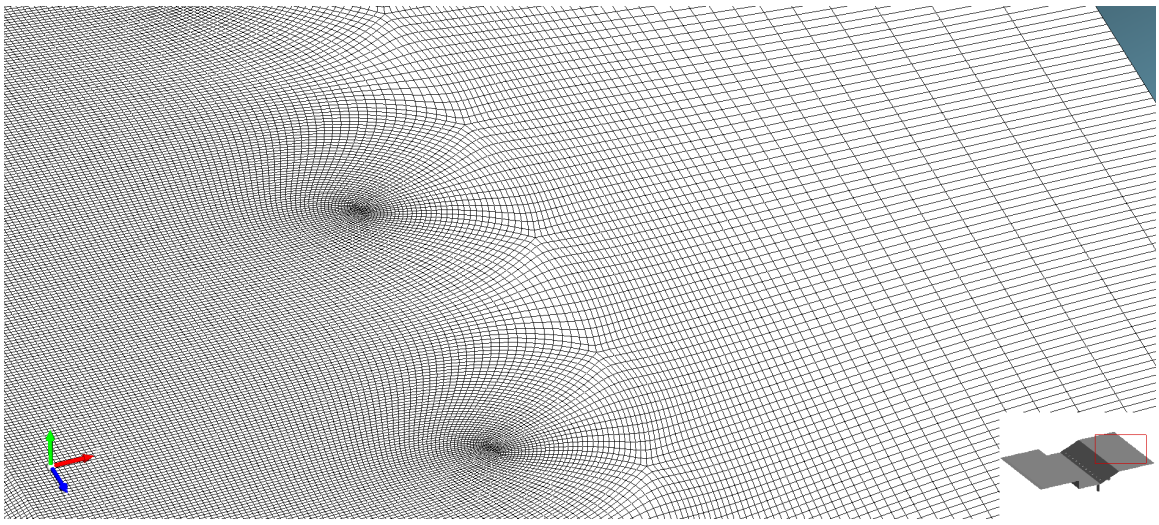

**Figure 21. Spanwise derefinement near the outflow of the cavity.**

**Table 4. Grid Sizing**

| Domain | Streamwise$_{max}$ | Spanwise$_{max}$ | Transverse$_{max}$ | $N_{cells}$ (mil) |
|---|---|---|---|---|
| Nozzle (2D) | 615 | 1 | 287 | 10 |
| Isolator | 712 | 692 | 286 | 140 |
| Combustor | 864 | 659 | 360 | 160 |

### 3.3 Boundary Conditions

The nozzle is simulated as two-dimensional using the aforementioned conditions in Table 2. Symmetry is enforced in the spanwise direction while viscous walls are used on the top and bottom surfaces. The statistics collection times were on the order of a few milliseconds, so the combustor wall does not have time to relax to the flow temperature. This makes isothermal walls with temperature based on the adiabatic conditions a reasonably accurate assumption. Adiabatic conditions were simulated to obtain mean temperatures on each wall and the isothermal conditions were informed by the results. The outflow is treated as supersonic with some grid stretching near the exit to reduce non-physical interaction of the boundary layer with the outflow plane causing pressure fluctuations to propagate upstream and affect the solution. The combustor boundary conditions are shown in Figure 22.

The domain is broken into three separate simulations to save on computational cost, and because of this, something must be done to simulate boundary layer development to accurately represent the turbulent boundary layer that will naturally develop in the research cell.

**Turbulent Inflow.**

To reproduce the development of a turbulent boundary layer as the flow proceeds through the facility and into the combustor, a multi-step process was used to provide a reasonable facsimile to use as the inflow to the combustor section. First, a digital filter was used to create a synthetic boundary layer for the isolator inflow. An overview of the digital filtering technique used here is given by Gonzalez et. al.[41]. This digital filter uses a one-dimensional line of solution from the exit of the nozzle and knowledge of typical boundary layer Reynolds stress profiles to distribute appropriately sized fluctuations throughout the primitive field on a spanwise plane of inflow. These digitally filtered fluctuations are simply a block of x-y fluctuations in a time series. An example of three instantaneous snapshots of the digitally filtered fluctuations is shown in Figure 23. The fluctuations here are consistent with the prescribed Reynolds stress profiles. The planes of fluctuations produced are just a fraction of the full inflow,

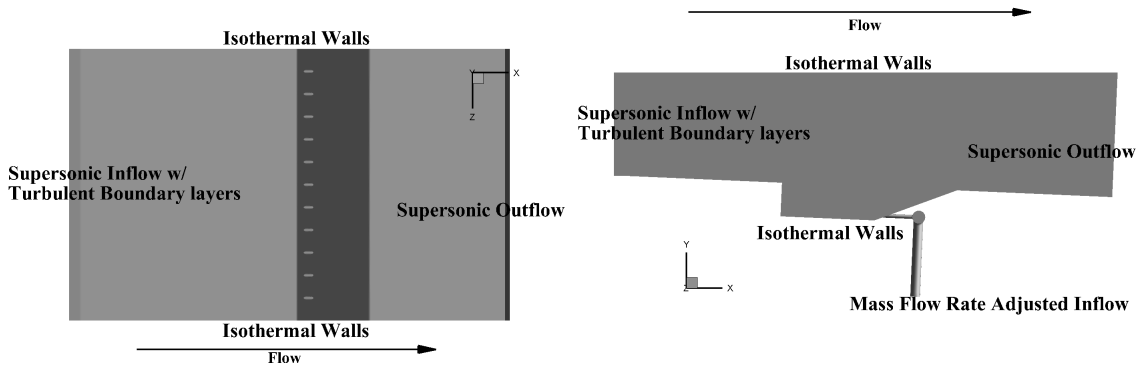


**Figure 22. Two perspective image of the boundary conditions around the combustor section of the geometry.**

so they must be rotated and translated to cover all walls. There is a blending function in the corners based on wall distance for the overlapping planes.

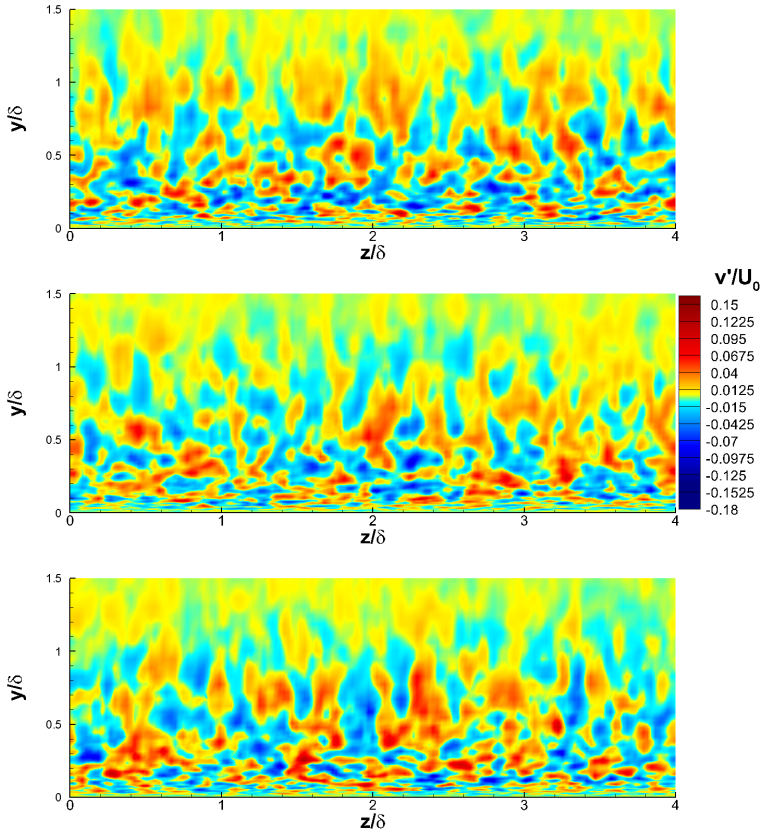


**Figure 23. Three different instantaneous snapshots of spanwise slices of digital filter turbulent boundary layer inflow generation. In general magnitude they are similar but the distribution is sufficiently different for initiating turbulent boundary development.**

These digitally filtered fluctuations are sufficient to begin the development of a turbulent boundary layer. The boundary layer is allowed to equilibrate as it flows through the isolator. After start up transients have blown through, an extraction plane is established near the outflow of the isolator for the purpose of saving the state of the solution over time. This plane is a few boundary layer thicknesses from the outflow so no non-physical interactions with the supersonic outflow are included in the extracted solution. The solution is saved every 10 timesteps for 2ms of simulation time. Figure 24 shows the results of this extraction at three different times. These

planes of solution containing four equilibrated boundary layers are then used as the inflow for the combustor section. The extraction is not every timestep, so multiple planes must be loaded into the solver simultaneously and a linear interpolation is performed between planes to preserve turbulent timescales and simulate boundary layer evolution over time without the heavy memory load of saving every timestep for a sufficient amount of time. This is the same method used by Peterson in several of his studies[39, 6]. Peterson compared this shortened domain against an extended length inflow that gives a turbulent boundary layer time to develop[8]. The extended inflow grid had more than twice as many cells as the shortened grid, but the difference in the time-averaged resolved TKE and velocity in the cavity was negligible.

Two rates of gaseous methane injection were simulated, 55 and 70 standard liters per minute. These flow rates were achieved through on-the-fly pressure adjustments at the inflow of the tubes leading into the bottom of the plenum[6]. There is some fluctuation as pressure waves reflect around the plenum, but it is a small percentage of the total flow rate as shown in Figure 25. These pressure waves come from interaction of the injection with the unsteadiness in the cavity.

## 3.4 US3D

The analysis software used for this study was US3D, a fully unstructured finite-volume compressible Navier-Stokes solver extensively validated for hypersonic flows[42, 43, 44, 45]. The simulations were divided into RANS for the nozzle, and IDDES for the isolator and combustor.

### IDDES.

Inviscid fluxes were evaluated at 4th-order using the kinetic-energy consistent scheme of Subbareddy and Candler[44]. Time was advanced using the 2nd-order

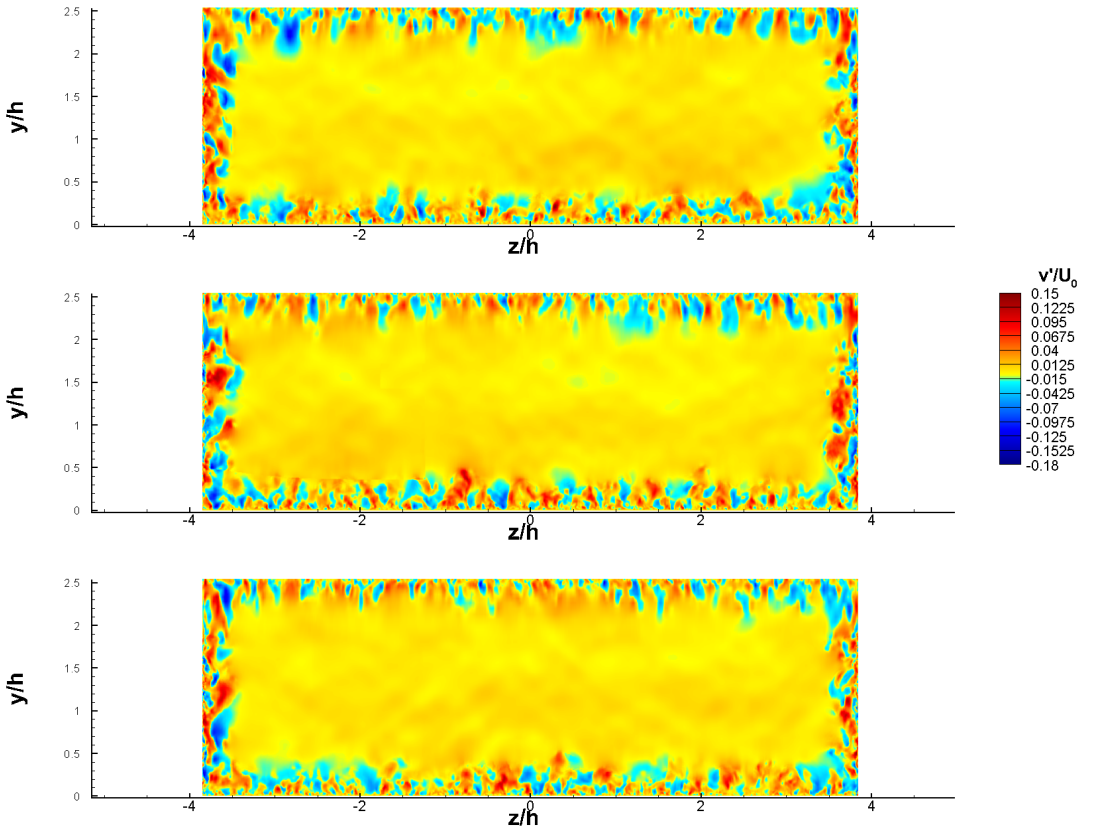


**Figure 24. Three different instantaneous extracts of spanwise slices at the end of the isolator. This shows fluctuating transverse velocity scaled by inflow velocity. The boundary layer has developed to the approximate thickness at the beginning of the combustor (0.09 cm). A series of snapshots like this are used as the inflow condition for the combustor.**

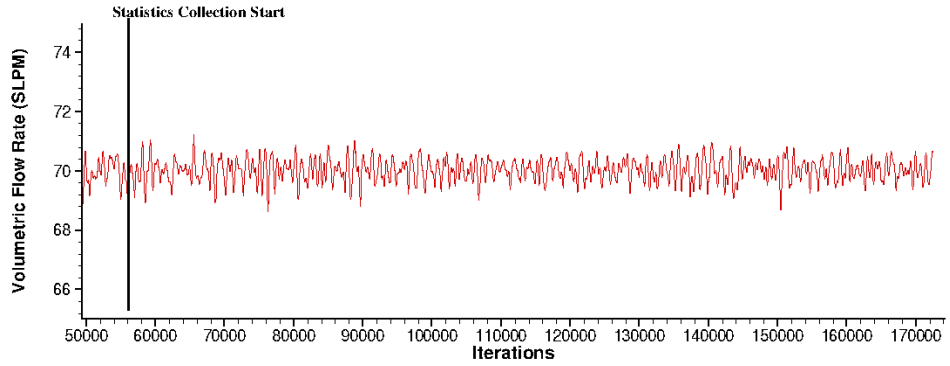


**Figure 25. Volumetric flow rate of gaseous methane into the plenum as a function of iteration number. Statistics start at iteration 56300, which is well after the injection rate becomes statistically stationary around the targeted mean.**

semi-implicit Crank-Nicholson scheme. The subgrid-scale RANS model used by this implementation of IDDES is the Spalart-Allmares turbulence model with density corrections by Catris[46].

### 3.5 Timestep Convergence

While an explicit method would be preferred due to the unsteadiness driving the character of the flowfield, this requires a timestep too low (on the order of $1 \times 10^{-9}$) to be feasible with current computational processing ability. Therefore, a time resolution study must be performed to observe what effect, if any, using a semi-implicit method with a Courant-Friedrichs-Lewy (CFL) number of greater than one has on the results. The CFL number is a multiplier of the maximum stable explicit timestep and describes how large a timestep increase an implicit method is providing. The test matrix for this study is shown in Table 5. All timestep studies were performed on the data grid, and 1 $ms$ of statistics were taken for each grid. This equates to about 4 convective flow times. This is more limited in length than other parts of this study due to the increased cost of a reduced timestep run on a full grid, as well as by the computing time available.

**Table 5. Time Resolution Test Matrix**

| Timestep Resolution | Timestep (s) | Avg. CFL |
|---|---|---|
| Coarse | $8 \times 10^{-8}$ | 20 |
| Medium | $4 \times 10^{-8}$ | 10 |
| Fine | $2 \times 10^{-8}$ | 5 |

#### Timestep Convergence Results.

The use of an implicit method requires an examination of what is lost when time is advanced faster than the character would allow in an explicit method. Three different

timestep sizes were examined and statistics were taken in each case. Figure 26 shows the skin friction coefficient plotted against $x$ scaled by the cavity height, $h$. The results look similar to altering the grid resolution, with all three agreeing on with the locations of local extrema, but with slightly differing magnitudes. This study is even more sensitive to the problem of high integral time scale, because with the finest timestep being twice as expensive as the one used with the data gathering runs, less simulation time was completed in order to finish the time resolution study. Again, the differences in local maximums and minimums all lie within a reasonable level and the concern is low that the timestep is a major contributing factor to variability in results.

The large influence that temperature has on radiation, and temperature's variability due to turbulence, makes it an important consideration when evaluating the effect of the grid on resolved turbulent effects. Figure 27 shows the root mean square of temperature fluctuations scaled by the mean temperature. Varying the timestep has very little effect on the temperature fluctuations. The peaks in the shear layer and near the cavity floor change by less than 10%.

The time resolution study shows that the coarse timestep may be sufficient for resolving the turbulent scales in this flowfield. All three timestep sizes showed very similar results for both time-averaged skin friction coefficient and time-averaged temperature fluctuations. The medium timestep size was used to collect data. This is done to avoid the possibility of failing to resolve high frequency content in the cavity that may not be captured by this resolution study if the largest timestep is used. The medium timestep is sufficiently large for the simulation times to remain tractable.

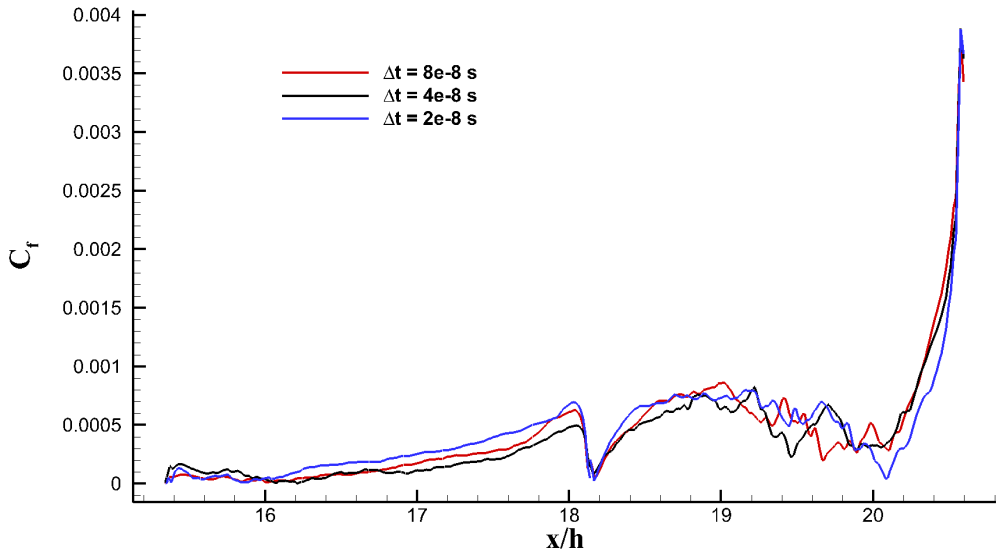


**Figure 26. Skin friction coefficient, $C_f$, calculated using the time-averaged wall shear. The red line is the coarse timestep ($8 \times 10^{-8}$) , the black line is the medium and data collection timestep ($4 \times 10^{-8}$), and the blue line is the fine timestep ($2 \times 10^{-8}$).**

### 3.6 Grid Convergence

Standard practice for all CFD simulations is to perform a grid convergence study to ensure that the solution is not a strong function of the grid used. Three different spacings were used in this study. The size of the grids involved in performing full span IDDES of this geometry necessitate only one direction (either spanwise (z), streamwise (x), or transverse (y)) being altered at a time. Even a small refinement in every direction would make the grid too large to run, and a derefinement would quickly lose too much resolution to preserve any accuracy in performing LES and make comparing refinement levels difficult. In every case, the two orthogonal directions to the altered dimension remain at data grid density. Grids with finer resolution than the data grid were attempted, but due to software and computing stability issues in handling grids this large (near 240 million cells each) this was not possible. The test matrix is shown in Table 6. The values in this table represent the isotropic cells away

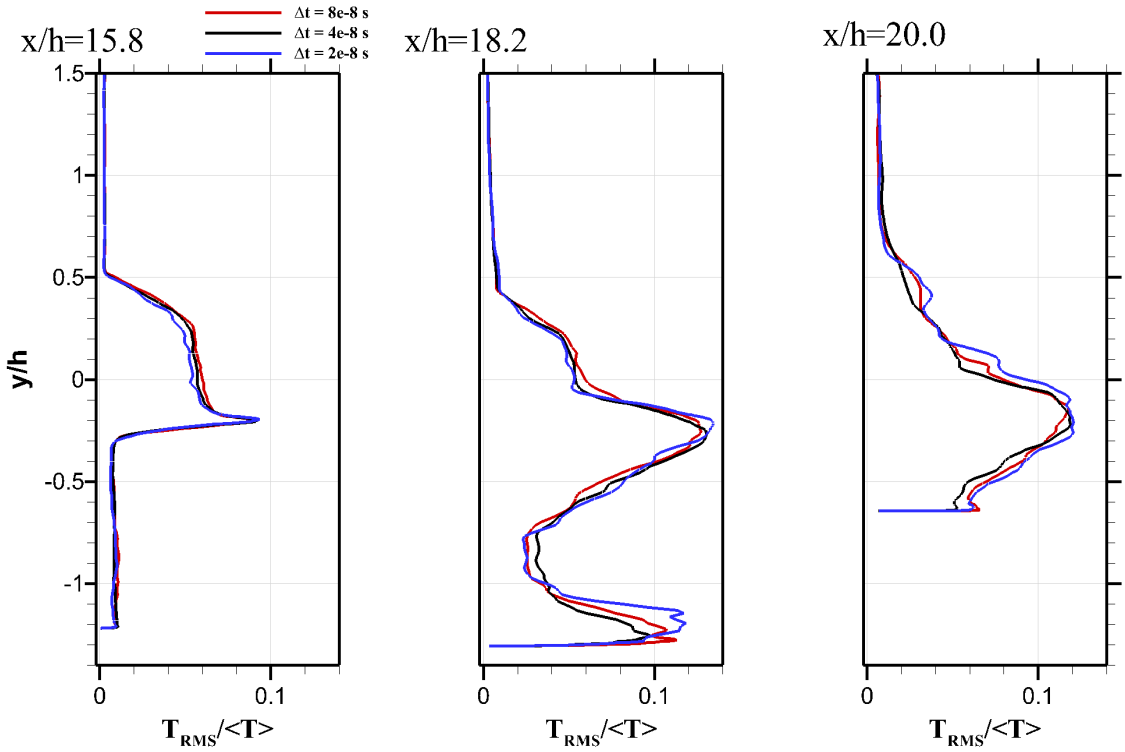


**Figure 27.** **Time-averaged root mean square of Temperature fluctuations scaled the time-averaged Temperature at three $x$ stations. The red line is the coarse timestep $(8 \times 10^{-8})$ , the black line is the medium and data collection timestep $(4 \times 10^{-8})$, and the blue line is the fine timestep $(2 \times 10^{-8})$.**

from the boundary layer clustering. Statistics were gathered for 2 $ms$ on each grid, or about 8 convective flow times.

**Table 6. Grid Convergence Test Matrix**

| Grid | $\Delta x^+$ | $\Delta y^+$ | $\Delta z^+$ | $N_{cells}$ (mil) |
|---|---|---|---|---|
| Span-Coarse | 100 | 100 | 150 | 103.9 |
| Span-Medium | 100 | 100 | 125 | 127.0 |
| Stream-Coarse | 150 | 100 | 100 | 105.8 |
| Stream-Medium | 125 | 100 | 100 | 127.1 |
| Transverse-Coarse | 100 | 150 | 100 | 105.0 |
| Transverse-Medium | 100 | 125 | 100 | 127.5 |
| Data Grid (Fine) | 100 | 100 | 100 | 159.0 |

There are many possible ways to examine grid and timestep convergence. One can examine averaged flow properties in regions of interest where refinement is altered. For confidence in grid convergence to exist, there should be minimal discrepancy when increasing resolution of the baseline grid so long as statistics have been taken for a sufficient amount of time. The grid used to collect data is already at, or very near, the limit for what is possible with the software and computing resources available, therefore there must be some extrapolation from multiple systematically coarsened grids. The size of the discrepancies (if any exist) when progressing from the coarsest meshes to the data mesh should be a good indicator for grid dependency.

Some speculation has been made that looking at the one-dimensional energy spectra and the distribution of resolved turbulent kinetic energy (TKE) versus modeled TKE can be of some indication of Hybrid RANS/LES resolution; however, a study done by Davidson shows that this is inconsistent, especially for free shear turbulence[47]. The same study asserts that finding the integral length scale and determining number of cells that exist per length scale is a more accurate method to determine if grid density is sufficient for eddy resolution. This can be done through finding the integral timescales and using the convective velocity to determine the

streamwise distance between correlated values.

**Grid Convergence Results.**

First, the effect of directional grid density is examined. The data grid was systematically decimated to create two additional levels of grid resolution in each direction (spanwise, streamwise, and transverse), making for an additional six computational meshes. Mean surface and flow quantities were then examined to determine if the decreased resolution caused large changes in the solution. Specifically, time-averaged wall shear was used to find the skin friction coefficient, and the time-averaged fluctuation velocities were used to calculate turbulent kinetic energy. The TKE was scaled by the bulk kinetic energy of the core flow. Statistics were all compared at 2 $ms$ of collection time. Initially, a finer density was included in each direction, but the very large cell counts caused instabilities in high performance computing node communication and the runs would not start.

The spanwise direction is of particular interest due to the collection method this study is attempting to validate and reinforce. Spanwise turbulent features are an important mode for convection of primitives in any flow and any simulation that doesn't properly resolve the span will produce poor turbulent statistics[48]. With the HSC integrating features along the line-of-sight, it is especially important to be able to say with accuracy what effect the turbulence has on the span, and that enough of the large eddies are resolved that the turbulence is correctly representative of the real flow. The time-averaged skin friction coefficient on the cavity floor and ramp, extracted along the line shown in Figure 28, is shown in Figures 29 - 31 for every grid in the convergence study. This is plotted against $x$-location scaled by cavity step height. All three resolutions in all three directions predict close to the same magnitude of average and fluctuations away from that average. The medium grid is

further from the fine grid than the coarse is for prediction the local maximum of skin friction at the base of the ramp, or at about $x/h = 18$. The differences are at, or less than, 10% total magnitude from the fine case and are not a concern for quality of grid used.

The resolved time-averaged turbulent kinetic energy, extracted at three $x$-stations shown in Figure 32, is shown in Figures 33-35 for all grids. These are roughly equidistant and show three very different parts of the cavity. There is good agreement between all grids on the location of peak turbulent kinetic energy in the most upstream $x$-station, where the peak represents the beginning of the shear layer. The figures show resolved turbulent kinetic energy so it is expected to see that, as resolution decreases, the average energy also decreases. In all three refinement directions, the coarse grids showed lower kinetic energy than the medium and fine grids, which predicted almost the same values. In the second two $x$-stations there exists differences in magnitude between all three grids. This region of the flow is near the intersection of several major features of the flow, a relatively slow recirculation region, an oblique shock, and a boundary layer. The effect is a region that requires much more statistics time to converge to a stationary mean.

The grid refinement study shows that the coarse and medium grids are sufficient to capture the time-averaged surface characteristics in the cavity. The coarse grids under-resolve much of the shear layer and do not capture the correct values for TKE. The medium grids are much closer to the fine grid in this regard; however, the fine grid still resolves higher peak values of TKE in the shear layer and therefore is the appropriate choice for use as the data collection grid.

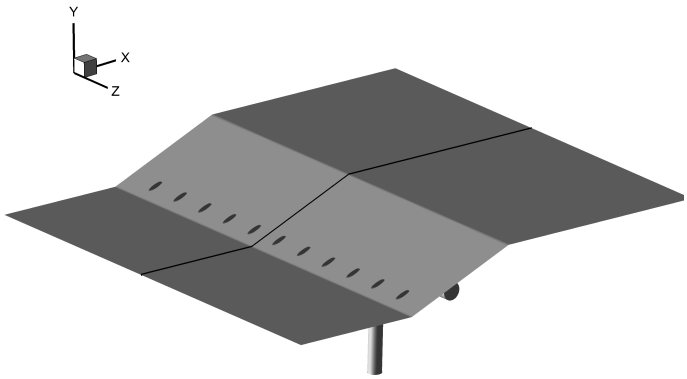


**Figure 28. Location for the skin friction coefficient extraction.**

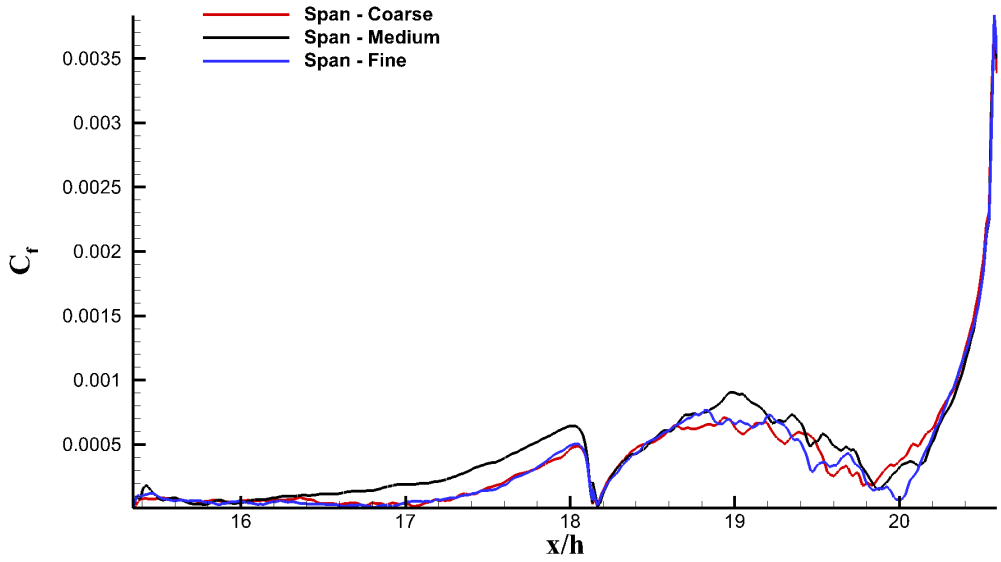


**Figure 29. Time Averaged Skin Friction Coefficient on the cavity floor and ramp for spanwise resolutions.**

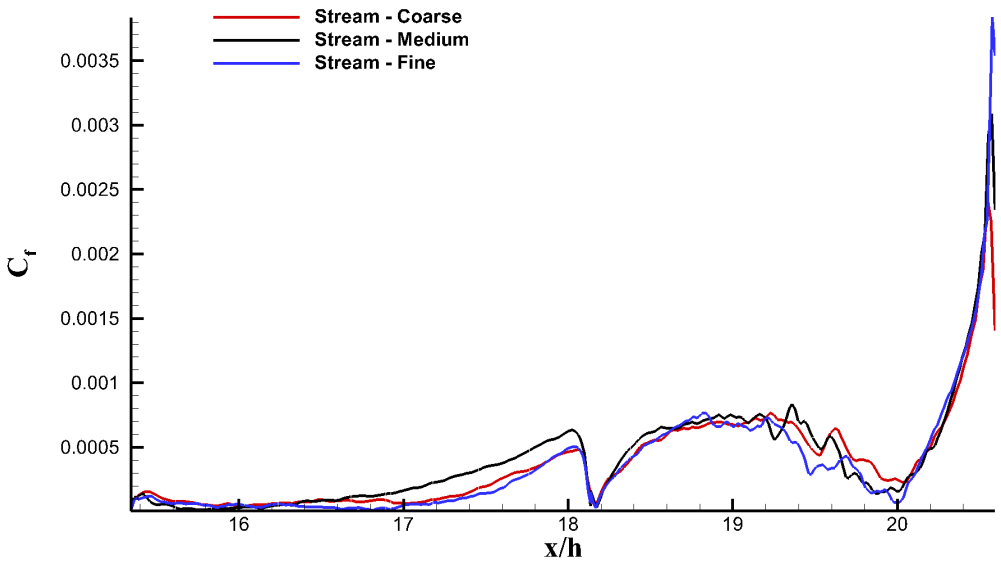


**Figure 30. Time Averaged Skin Friction Coefficient on the cavity floor and ramp for streamwise resolutions.**

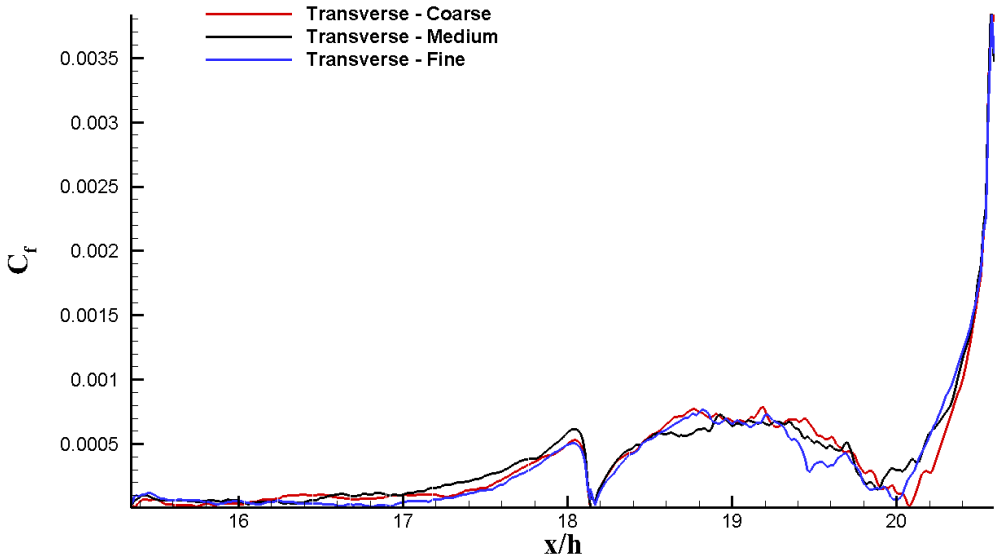


**Figure 31. Time Averaged Skin Friction Coefficient on the cavity floor and ramp for transverse resolutions.**

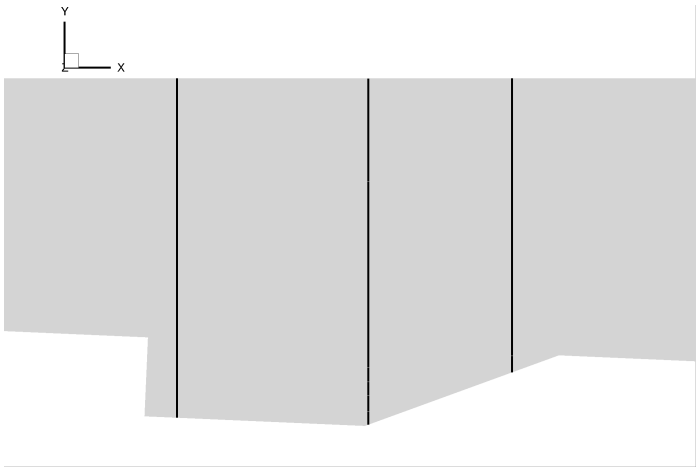


**Figure 32. Location of the X-Stations for the resolution studies.**

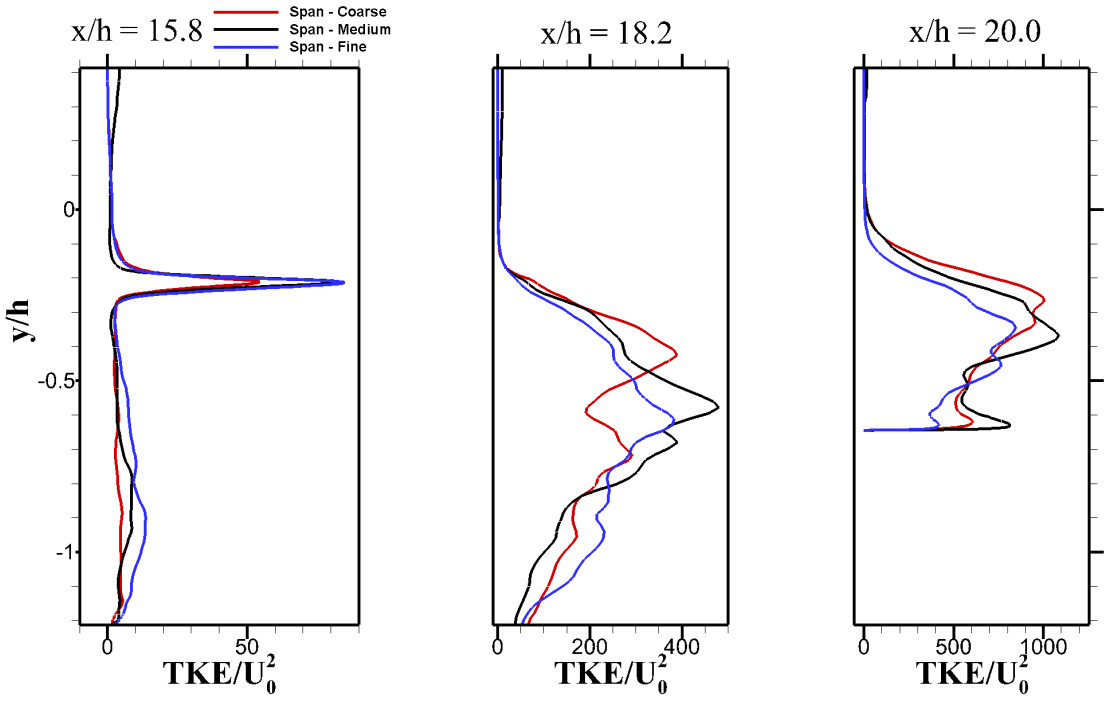


**Figure 33. Time Averaged Turbulent Kinetic Energy normalized by bulk kinetic energy at all three spanwise resolution levels. The red line is the coarse grid, the black line is the medium grid, and the blue line is the fine (and data) grid.**

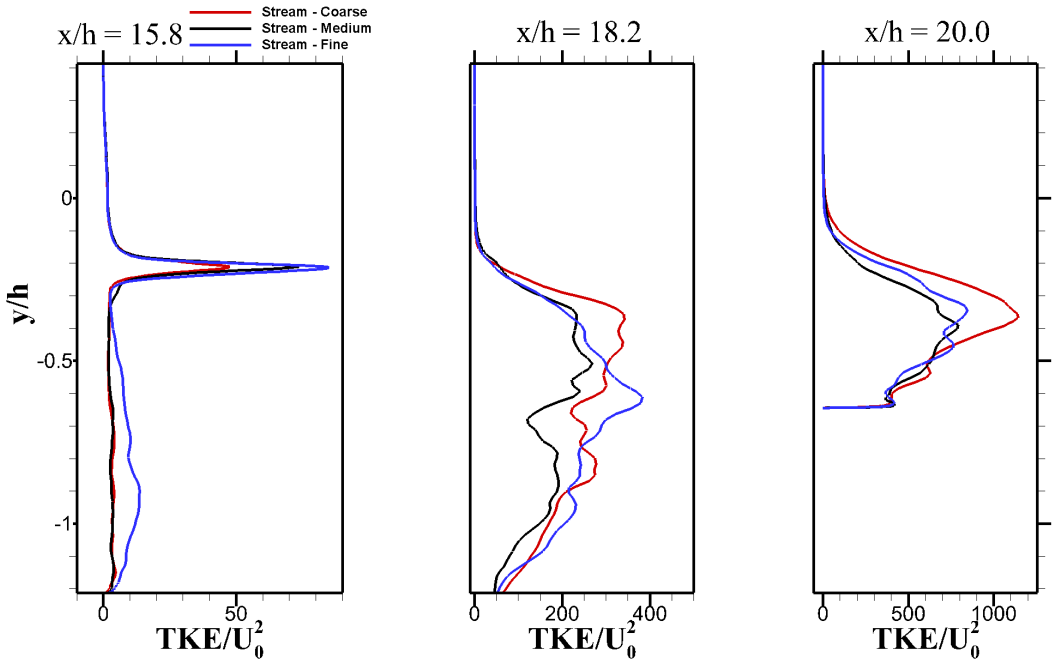


**Figure 34. Time Averaged Turbulent Kinetic Energy normalized by bulk kinetic energy at all three streamwise resolution levels. The red line is the coarse grid, the black line is the medium grid, and the blue line is the fine (and data) grid.**

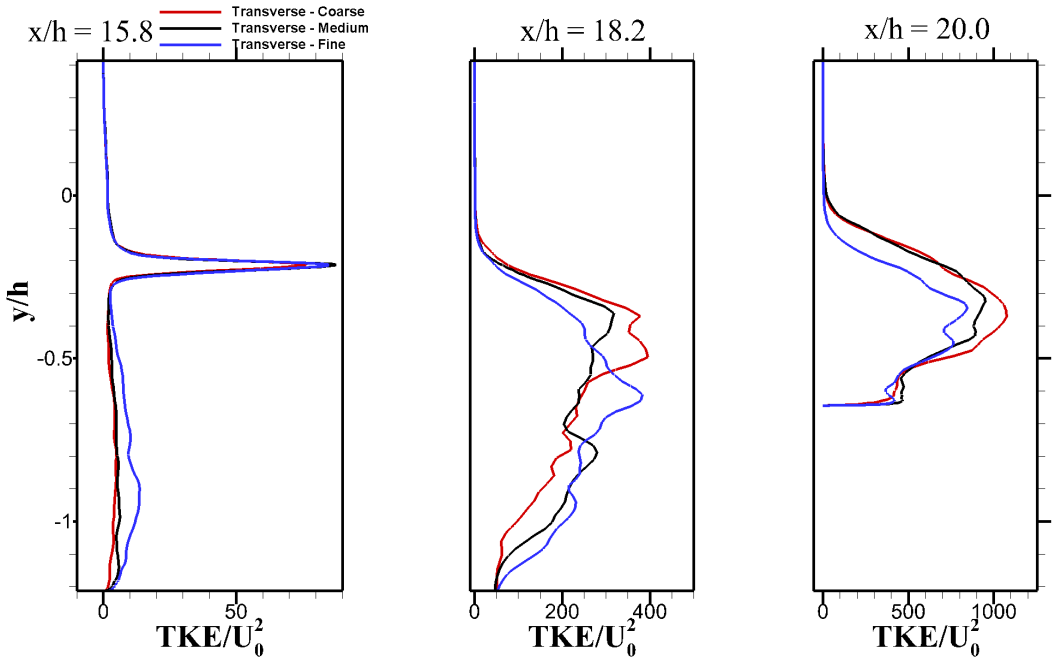


**Figure 35. Time Averaged Turbulent Kinetic Energy normalized by bulk kinetic energy at all three transverse resolution levels. The red line is the coarse grid, the black line is the medium grid, and the blue line is the fine (and data) grid.**

**Data and Statistics Collection.**

The combustor simulation was initialized at freestream conditions with the plenum starting at near running conditions. The plenum was "frozen" until the base flow through the cavity was setup in RANS. The plenum was unfrozen and injection was allowed to run for 10 $ms$ to allow the pressure-controlled mass flow rate to converge to the target value. The simulation was converted to IDDES and allowed to run for approximately 2 $ms$ to blow out any remaining transients before statistics were gathered.

**Table 7. Spanwise Line Locations**

| Line | $x/h$ | $y/h$ |
|---|---|---|
| 1 | 15.54 | 2.05 |
| 2 | 15.92 | -0.26 |
| 3 | 15.67 | -0.97 |
| 4 | 17.8 | -0.79 |

The experimental data of primary interest for comparison are the hyperspectral images. The information gathered with this device is integrated both over the spanwise distances as well as a finite amount of collection time. A full scan takes on the order of a few seconds, while each station of the moving mirror in the Michelson

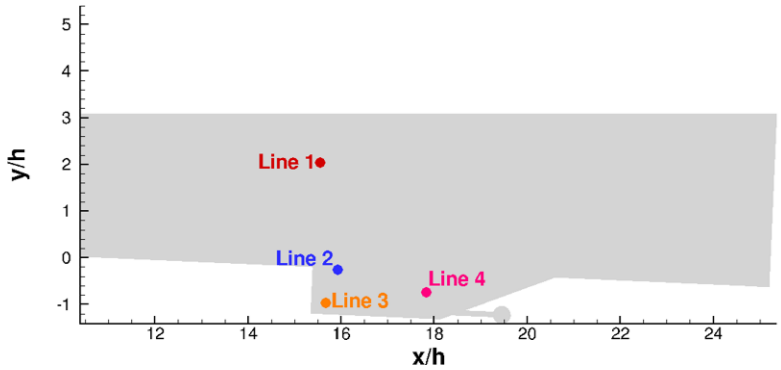


**Figure 36. Graphical representation of spanwise line placement in XY plane.**

interferometer takes approximately $200\mu s$. This motivates the collection of spanwise cells stacks, or lines, placed in regions of interest in which a complete time history of the primitives in each cell can be saved over the entire simulation. The coordinates of the lines are displayed in Table 7 and a graphical representation of the lines are shown in the XY plane in Figure 36. The origin of the $x$ axis is at beginning of the combustor section. This is directly analogous to the pixel-based data storage method used by the HSI. The collection of each wavelength through the Michelson interferometer takes some small quantity of real time (approximately 200 $\mu s$). This motivates the collection of arbitrary windows of this length of time being separated from the total simulation statistics for direct analysis. Figure 37 shows how these shortened windows of statistics compare to the total time history. The graph is zoomed in to 1ms so that the windows are visible, but the total statistics time included in the total mean is 4.64ms. The spatial resolution of this computational grid, and therefore these spanwise data, is much greater than that of the HSI, but no spatial averaging was performed to attempt to match this discrepancy of resolutions.

The size of the grids required for these simulations is almost too large to be tractable for the level of fidelity desired. The coupling of small timestep sizes and large cell counts with research questions that disallow the reduction of domain size

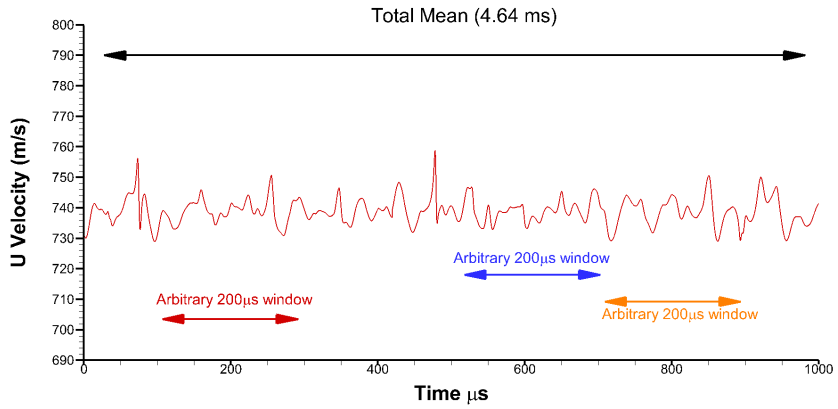


**Figure 37. Example of how the shortened statistics windows relate to the total mean.**

or Reynolds number leads to simulations that take on the order of one or two months to accumulate just a few milliseconds of statistics time per case. Ideally, more time would be available to continue the simulations and accumulate more statistics, but time and computational restraints limit the ability to do so. All assertions in this study are made with the possibility that statistics would continue to change, even if the change is likely small, if simulations were continued.

# IV. Results and Analysis

The fine grid was used to obtain all of the following results. The medium timestep of $4 \times 10^{-8}$ was selected. The core flow was Mach 2.0 with a total temperature of 589 Kelvin. Two injection rates of gaseous methane were run, 55 and 70 SLPM, and both are at a temperature of 540 Kelvin. Total statistics times ranged from $2 - 4.64ms$ depending on the injection rate and the feature.

## 4.1 General Flow Characterization

It is important to know what features make up the flow in question before looking more closely at quantitative results. In the experimental world, typically a shadowgraph or Schlieren image is used. These are both density-based visualizations of the flow. This is especially useful in shock-dominated flows, so the often CFD uses density gradient magnitude figures for the same purpose. Figures 38a and 38b show the instantaneous and time-averaged density gradient magnitude of the midplane, while Figures 39a and 39b show the instantaneous and 4.64 ms time-averaged pressure gradient magnitude at the same plane.

Examining these two sets of figures shows that the top and bottom turbulent boundary layers together occupy a large portion of the transverse height of the cavity. It also reveals the weak expansion fan at the beginning of the 2.5° divergence, and the oblique standing shock near the top of the ramp. It is also clear how quickly the shear layer expands after forming off the corner of the backward facing step. Comparing the figures shows that very few of these features are completely steady, with even the shock moving as the turbulent boundary layer and eddies from the recirculation region interact while passing through that region of the domain.

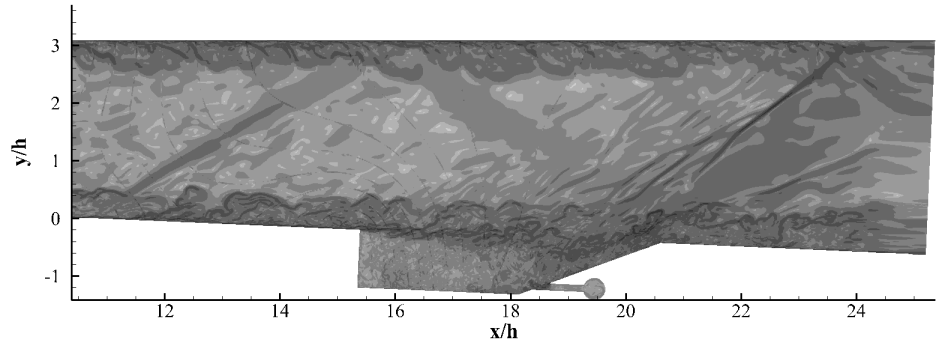


**(a) Instantaneous**

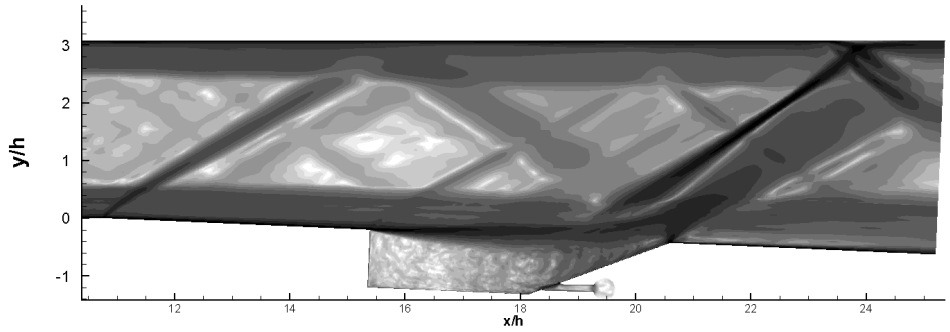


**(b) Time-Averaged**

**Figure 38. Density Gradient Magnitude using time-averaged density values at the combustor midplane.**

### Instantaneous Captures.

Visualization of the flow features provides a good qualitative understanding of the regime that serves as a basis from which to view the quantitative data later. For this reason, the first figures in this section are instantaneous snap shots of planes in significant regions of the cavity. These figures contain the same planes oriented the same way: the x-y centerline plane (top), the injector plane (bottom left, $y/h = -1.172$), the shear layer (bottom right, $y/h = -0.211$) and an arbitrary mid-cavity z-plane (bottom middle, $y/h = -0.737$). Figure 40 shows the instantaneous normalized temperature for an injection rate of 55 SLPM. Many of the very fine structures in the inertial sub-range normally physically present in the near-wall region are absent

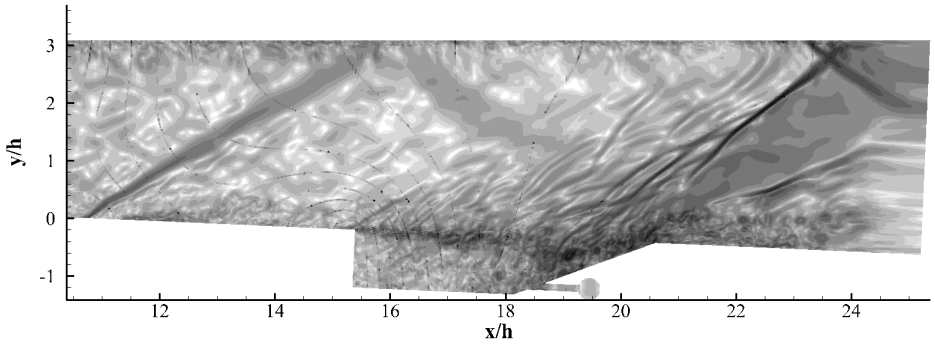


**(a) Instantaneous**

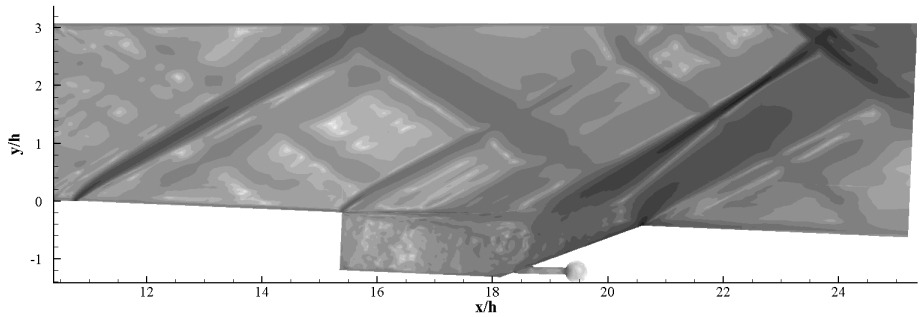


**(b) Time-Averaged**

**Figure 39. Pressure Gradient Magnitude using time-averaged pressure values at the combustor midplane.**

due to IDDES modeling these effects instead of resolving them, but more exist than otherwise would if using just DDES[32]. The massively separated regime in the cavity itself is well captured and the shear layer is well defined. The spanwise boundary layers are nearly indistinguishable from the eddy structures in the free shear layer across the span when considering just temperature. The non-mixing study done previously concurs with this observation on temperature[1], suggesting that injection does not significantly change the nature of the temperature distribution in the cavity prior to combustion.

When there is no combustion in the cavity, viscous heating is the largest source of a gradient in temperature. It is expected that the trends in spanwise variation of temperature are relatively negligible. Once combustion is initiated, the temperature

variation will vary sharply with combustion location and intensity. To get an idea of where combustion will occur in the cavity, fuel-to-air equivalence ratio is examined. Equivalence ratio, usually denoted by $\phi$, is the ratio of existing air-to-fuel in the cavity versus the stoichiometric conditions[13]. An equivalence ratio of exactly one means stoichiometric conditions exist at that location, while less than one means fuel lean and greater than one means fuel rich. Figures 41 and 42 show the equivalence ratio in the cavity when injecting at 55 SLPM and 70 SLPM respectively. From examination of multiple instantaneous slices, there is a large degree of unsteadiness in the cavity with respect to distribution of fuel which would heavily affect the temperature distribution once combustion is initiated. There also exists a high degree of unsteadiness of injection at the cavity-injector interfaces.

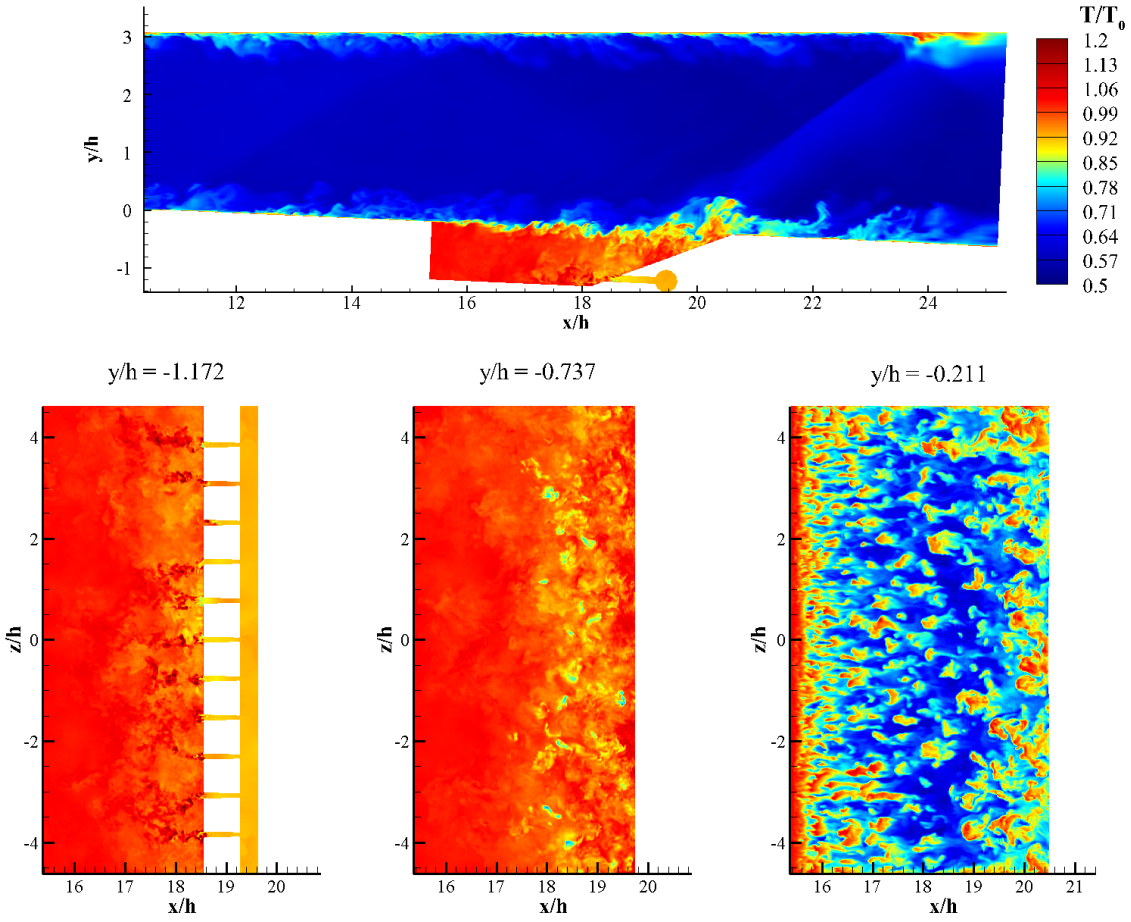


**Figure 40. Instantaneous snapshot of temperature with injection at 55 SLPM at the midplane (top) and three Y-planes (bottom) in the cavity, increasing in height from left to right. The far left image is on the injector plane, and the far right is in the shear layer.**

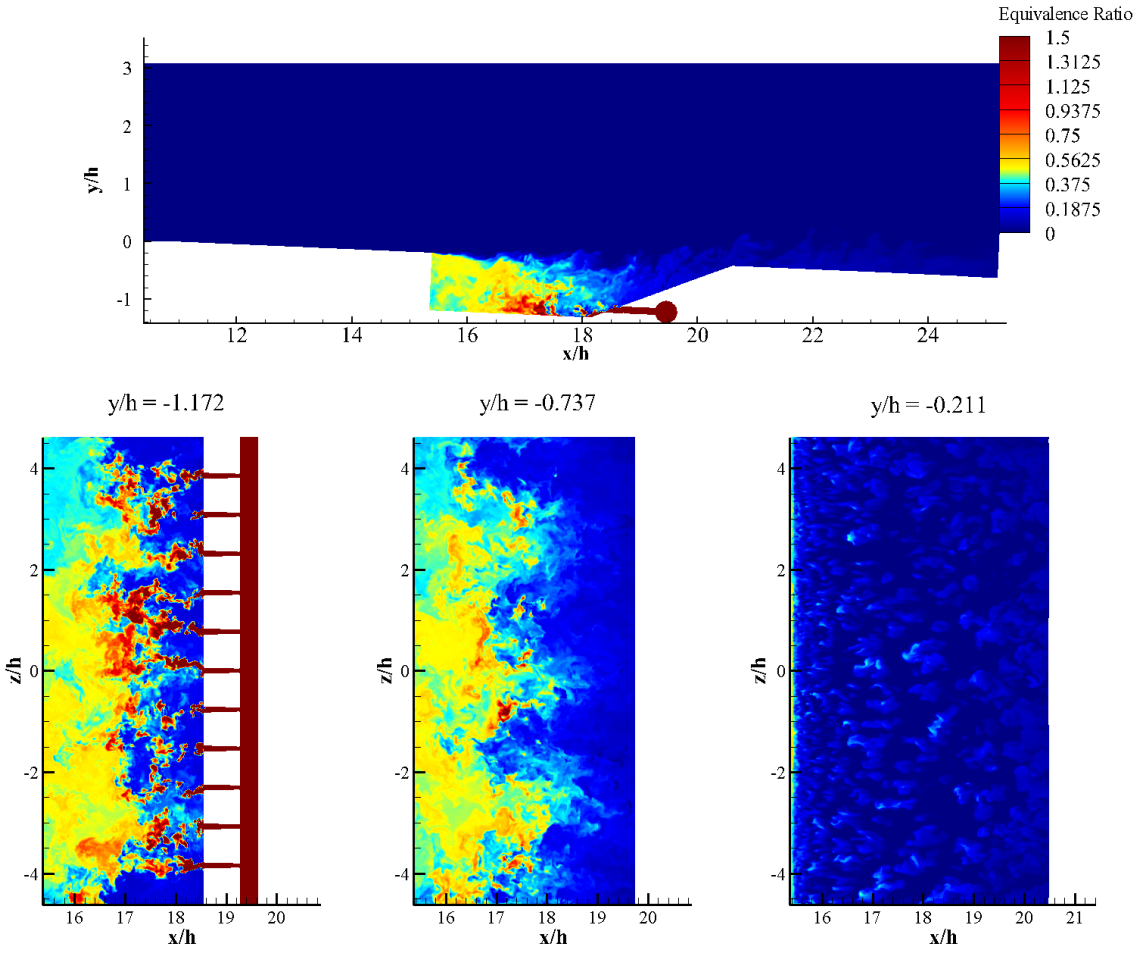


**Figure 41. Instantaneous snapshot of equivalence ratio with injection at 55 SLPM at the midplane (top) and three Y-planes (bottom) in the cavity, increasing in height from left to right. The far left image is on the injector plane, and the far right is in the shear layer.**

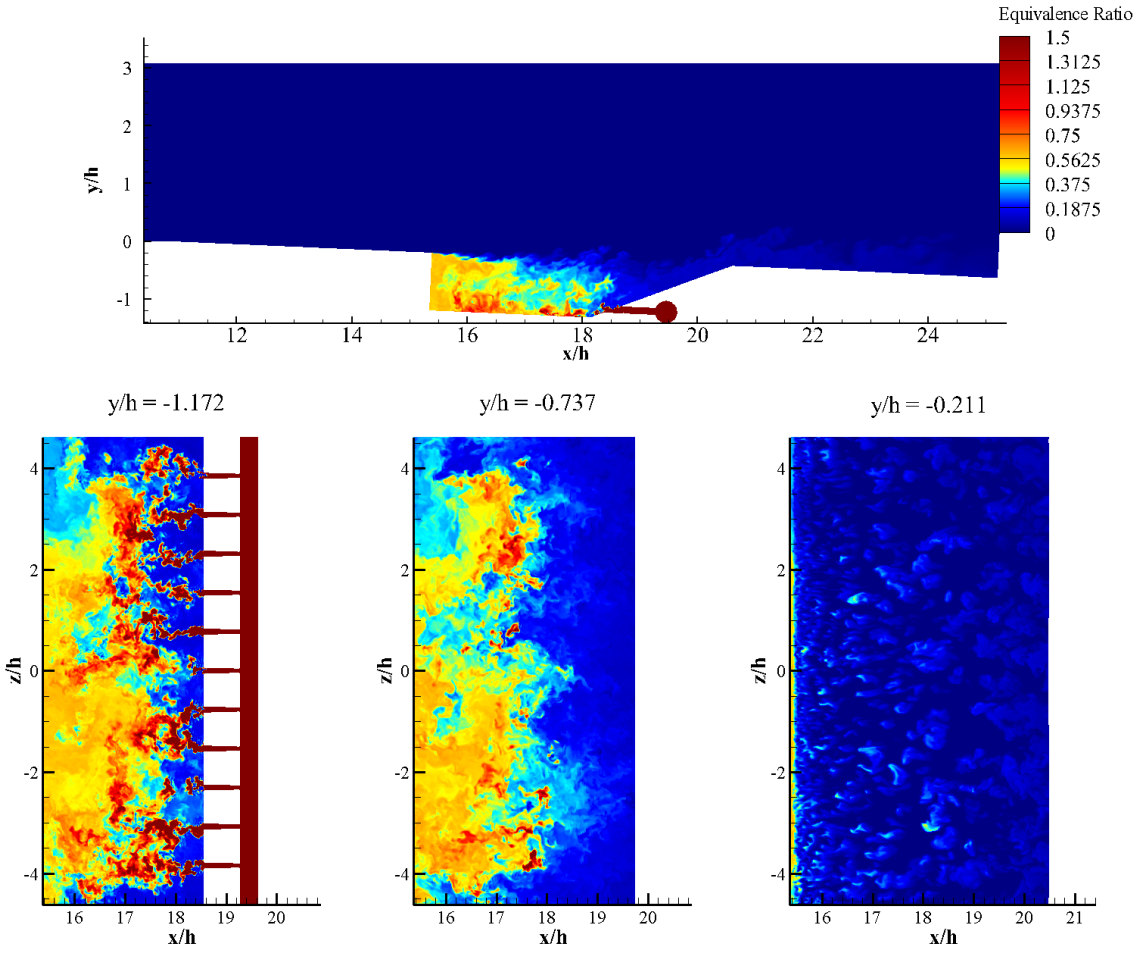


**Figure 42. Instantaneous snapshot of equivalence ratio with injection at 70 SLPM at the midplane (top) and three Y-planes (bottom) in the cavity, increasing in height from left to right. The far left image is on the injector plane, and the far right is in the shear layer.**

**Time-Averaged Captures.**

The processing of the HSI deals with time-averaged and ensemble-averaged data, so the HSI will only capture the unsteady and non-uniform features if they exist in the mean. Therefore, time-averaged statistics on the walls and in the domain were recorded while simulating. The same planes of interest from the instantaneous figures are used again for the time-averaged data for comparison. Temperature was examined along with equivalence ratio and the velocity fields. Lines were extracted from this data and compared against experimental data from Tuttle et al[10]. Figure 43 shows the time-averaged equivalence ratio with injection at 70 SLPM. The unsteadiness of the injection at the cavity ramp ports trends towards being statistically stationary in the mean. The non-uniformity in the spanwise structures in the mid-cavity plane at $y/h = -0.737$ that appeared in the instantaneous contours persist through the time-averaging of equivalence ratio. Three "lobes" standout as large spanwise inhomogeneous structures. It's possible these lobes develop as part of a spanwise non-uniform recirculation that traps fuel away from the wall and prevents even distribution of mixing in the cavity. The exact form that the lobes take could depend heavily on the length of the span, or the aspect ratio of the $x - z$ dimensions of the cavity. If the spanwise width is reduced without changing the streamwise depth, it's possible no lobes, or a single lobe, form in place of three. If the spanwise width is increased, more lobes could form or the lobes could simply increase in size. Studies with spanwise variation in length are required to determine the sensitivity of this phenomenon to changes in geometry.

The existence of these lobes of fuel answers the question of whether spanwise inhomogeneity exists in the cavity. Qualitatively, there are obviously large spanwise structures that are not approximated accurately by a 2D assumption. More importantly, these spanwise structures exist in fuel equivalence ratio, which is indicative

that, even if it does not take the exact same shape, there will be spanwise inhomogeneity in the location of combustion once it is initiated, leading directly to a large inhomogeneous temperature profile in the span.

**Velocity Field.**

The mean velocity field was compared to the experimental results from Tuttle et al[10]. Streamlines were calculated from the mean streamwise and transverse velocities at the midplane and compared to the experimental PIV measurements at the midplane. Both cases are non-reacting. The source of the experimental data is at the same flow conditions and injection rate; however, the non-reacting experimental data were gathered with no fuel injection and the previous periodic Hybrid RANS/LES simulations were run with ethylene injection. Ethylene is a heavier molecule than methane (an increase of about 12 g/mol), but the quantities represented in the simulation are low enough that it is unlikely that the flowfield will be altered in a significant way. One concern may be the difference in buoyancy between methane and ethylene. The flame Froude number, shown in Equation 34, is a formulation of the Froude number used to demonstrate the relative importance of inertial jet forces and gas buoyant forces for a turbulent flame[13]. This equation is not directly applicable, but it can be used to guide thought on whether buoyancy is a dominant factor in this flow.

$$Fr_f = \frac{v_e f_s^{3/2}}{(\frac{\rho_e}{\rho_\infty})^{1/4}[\frac{\Delta T_f}{T_\infty} g d_j]^{1/2}} \tag{34}$$

Assuming the three gases involved in this calculation (methane, ethylene and air) are at the same temperature and pressure, the individual gas constants can be used to compare their densities. The three gas constants are 287, 518 and 296 $(J/kg-K)$ for Air, $CH_4$, and $C_2H_4$ respectively.

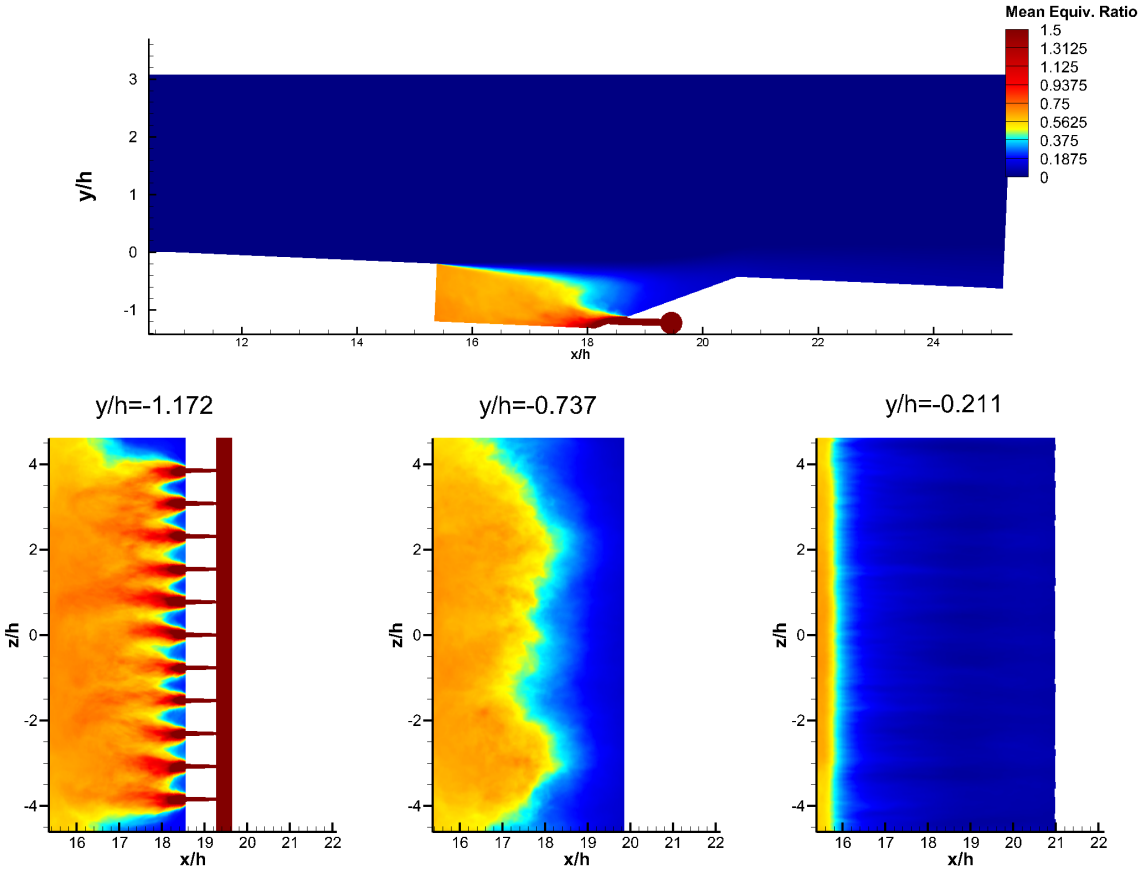


**Figure 43. Time Averaged equivalence ratio with injection at 70 SLPM at the midplane (top) and three Y-planes (bottom) in the cavity, increasing in height from left to right. The far left image is on the injector plane, and the far right is in the shear layer.**

Density is inversely proportional to the gas constant, so this means the $\frac{\rho_e}{\rho_\infty}$ term for methane to air is 0.554 and for ethylene to air is 0.970. This is not a large difference in the buoyancy term of $Fr_f$, especially considering the term has a power of $\frac{1}{4}$. The velocity of the injected gas exiting the injectors into the cavity is typically around $60 - 100$ m/s. Assuming all else is nearly the same, this flame Froude number would heavily favor inertial forces. Another concern may be the velocity change associated with fuels of different densities; however, because the fuel is held at a constant volumetric flow rate, the mass flow rate is adjusted and the required velocities (calculated through $\dot{m} = \rho A v$) change by less than 1% between the two fuels. This change is significantly less than the natural oscillation of the injection rate due to shifting pressure gradients. No matter which fuel is used, the injection rate is slow compared to the convective motion in the cavity. The recirculation is carrying air back down the ramp at more than twice the velocity and mass flow rate of the fuel is low. The injection of fuel should have little effect on the velocity field.

The simulation shows very good qualitative agreement with the experiment and the previous IDDES periodic simulation when considering the velocity fields (shown by streamlines in Figures 44a - 44b), especially with the main clockwise recirculation region. The exact location of the center of the primary recirculation as predicted by both simulations is very slightly shifted upstream and further down into the cavity than the experimental results. The secondary recirculation is less closely matched, but it is difficult to maintain consistent PIV particle density in that region of the flow. The result is PIV reporting a less defined recirculation than actually occurs.

Velocities scaled by freestream velocity were also compared at several $x$-stations to the experimental results, shown in Figures 45 and 46. The simulation agreed very well with the experimental data at all stations when considering the streamwise velocity component; however, the transverse velocity is further off for some of the downstream

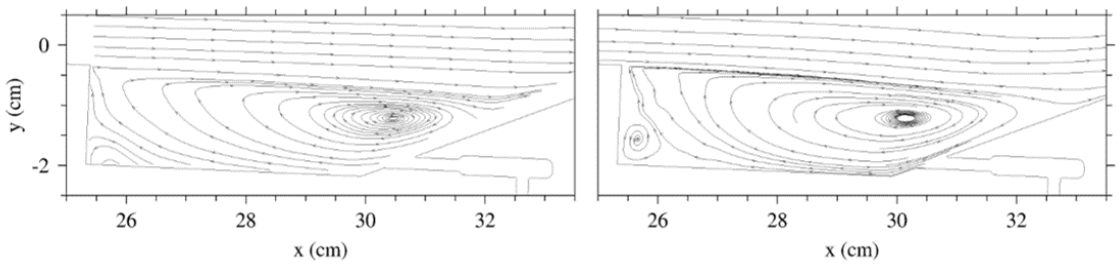


**(a) Experimental (left) and Periodic IDDES streamlines (right)**

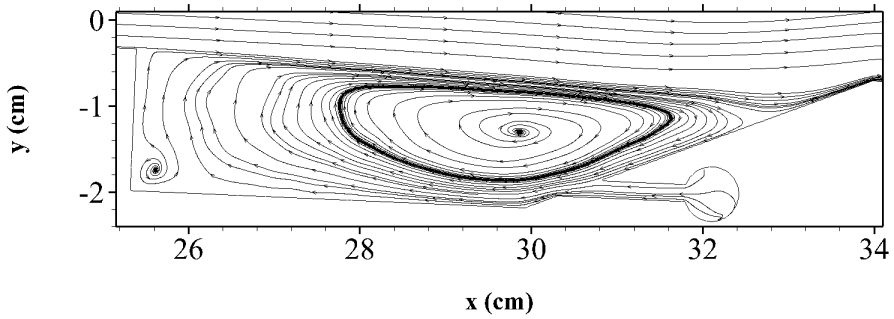


**(b) Full Span IDDES Simulation**

**Figure 44. Experimental (top) and simulation (bottom) streamlines on the midplane calculated with mean velocities.**

stations. The total magnitude of the transverse velocity is very low compared to the rest of the flow, and so larger differences are not unexpected. The differences seen here might be due to the center of the primary recirculation not matching with the experiment, as these last few $x$-stations are near the center. If the lines are now on slightly different parts of the recirculation, then the signs will vary slightly in the mean.

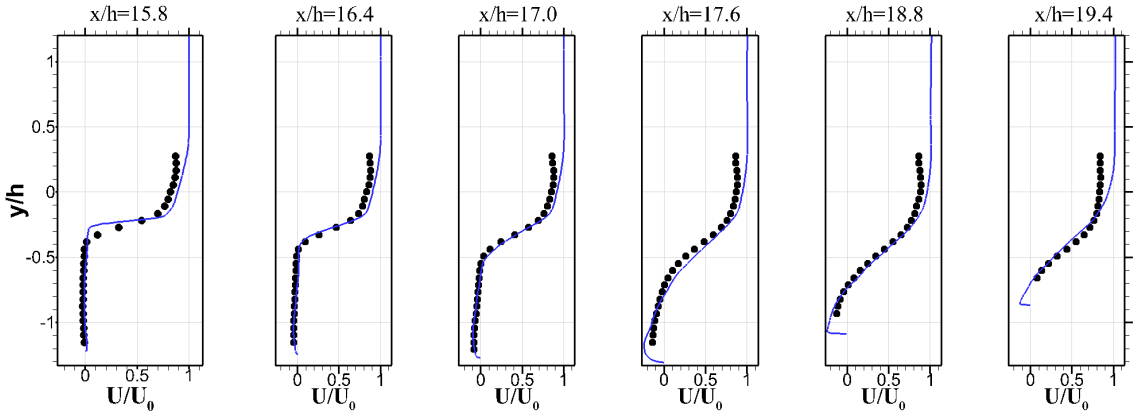


**Figure 45. Time-averaged streamwise velocity from the 70 SLPM $CH_4$ simulation (blue lines) compared to experimental results (black dots) from Tuttle et al. injecting $C_2H_4$[10].**

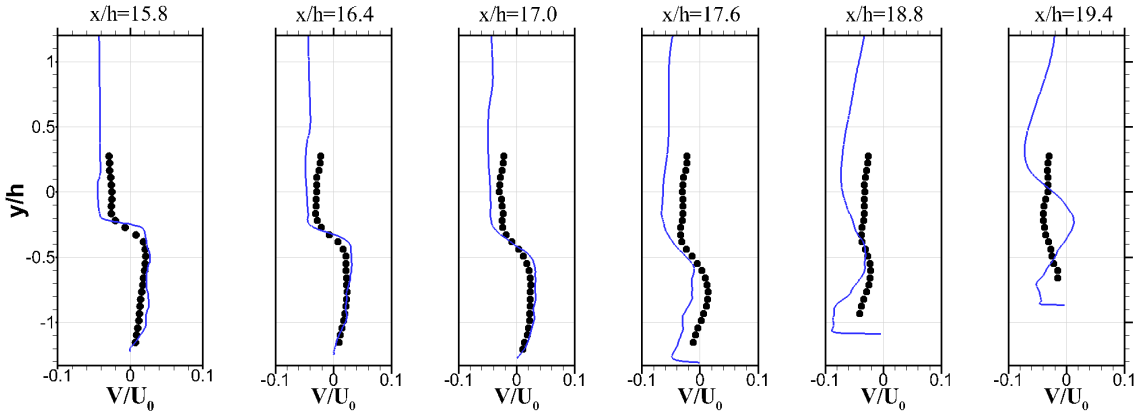


**Figure 46. Time-averaged vertical velocity from the 70 SLPM $CH_4$ simulation (blue lines) compared to experimental results (black dots) from Tuttle et al. injecting $C_2H_4$[10].**

**Spanwise Lines.**

To gain an understanding of what information may be line-of-sight integrated, spanwise lines were established across the cavity analogous to how the hyperspectral camera absorbs incoming photons. Complete time histories were saved at every cell across the line. Statistics were calculated, including mean temperature and mean equivalence ratio. The line locations are shown on the XY plane on Figure 36. Line 1 is in the core flow, Line 2 is in the shear layer, Line 3 is in the cavity near the corner between the backward facing step and the floor, and finally Line 4 is on the mid-cavity plane near the ramp. The total means were calculated along with windows of 200 $\mu$s to estimate what the HSC will see during each interferogram.

Figures 47a - 50 shows the temperature scaled by inflow total temperature of every line at both injection rates. Spanwise distance is normalized by the cavity height, $h$, and the mid plane is at $z/h = 0$. Temperature in every part of the cavity remains independent of volumetric fuel flow rate at the two injection rates simulated in this study. Line 1 in the core flow exhibits almost no turbulent fluctuation at all and each windowed mean is nearly identical to the total simulation mean.

Line 2 shows many small eddies affecting the short window mean, but seeing that the windowed means only "fluctuate" around the much smoother total mean, this indicates that more statistics time will make the total mean trend towards being statistically stationary. As $z/h$ moves towards either wall, there is a very slight increase in mean temperature, but the total effect is less than 5% of the total temperature of the core flow, so it is mostly negligible for spanwise averaging.

In contrast, the cavity corner (Line 3) exhibits large turbulent structures across the entire span that vary the profile with the eddies that are passing through the line of sight at the time of data collection, though the mean is still largely static near the total temperature.

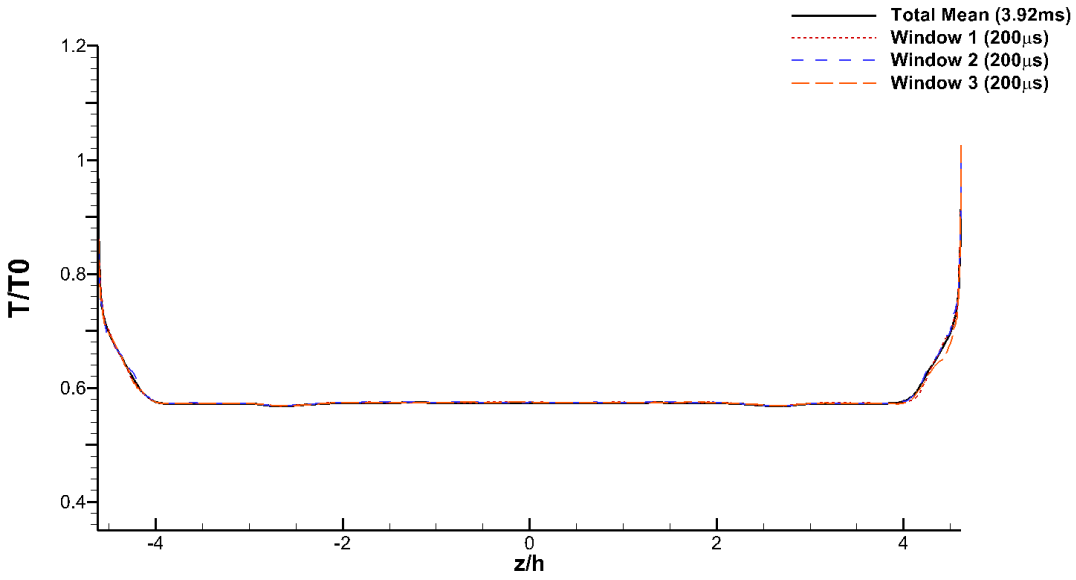


(a) 55 SLPM

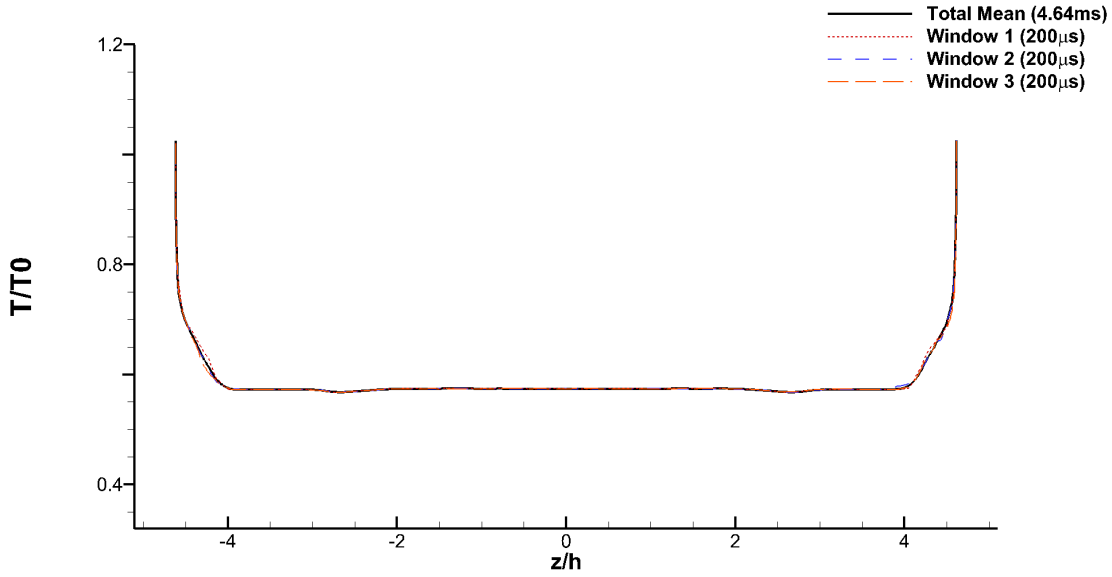


(b) 70 SLPM

**Figure 47. Spanwise variation along line 1 of mean temperature of both injection rates. Solid lines are the time-average for the complete simulation. Dashed lines are arbitrary 200 $\mu$s means.**

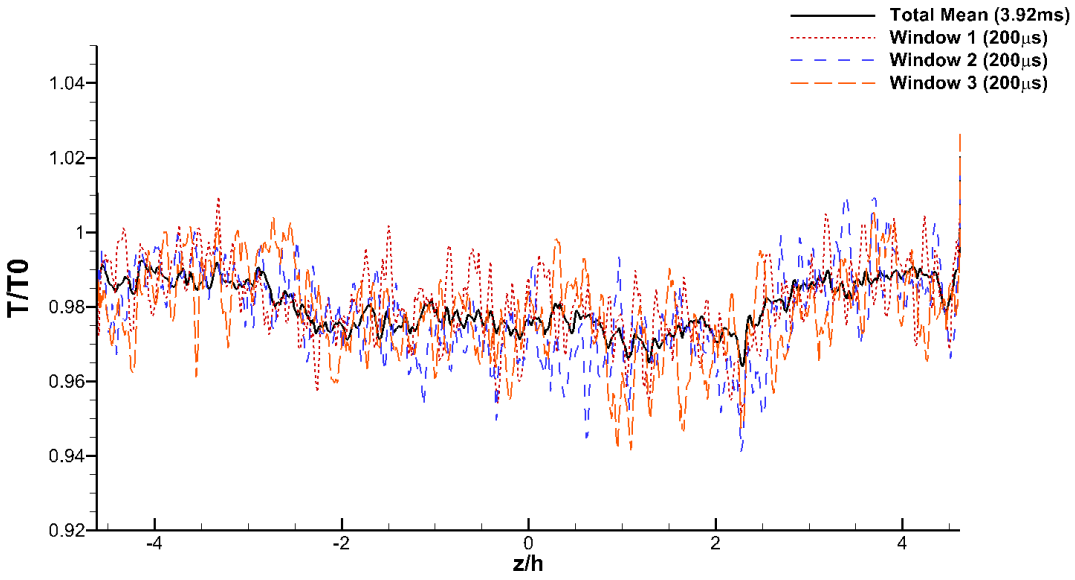


(a) 55 SLPM

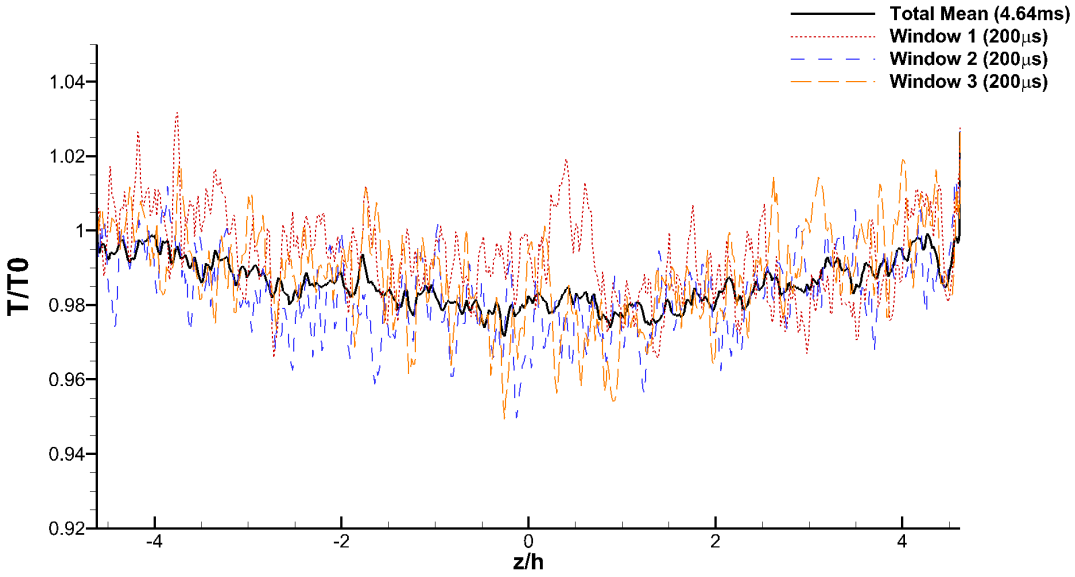


(b) 70 SLPM

**Figure 48. Spanwise variation along line 2 of mean temperature of both injection rates. Solid lines are the time-average for the complete simulation. Dashed lines are arbitrary 200 $\mu$s means.**

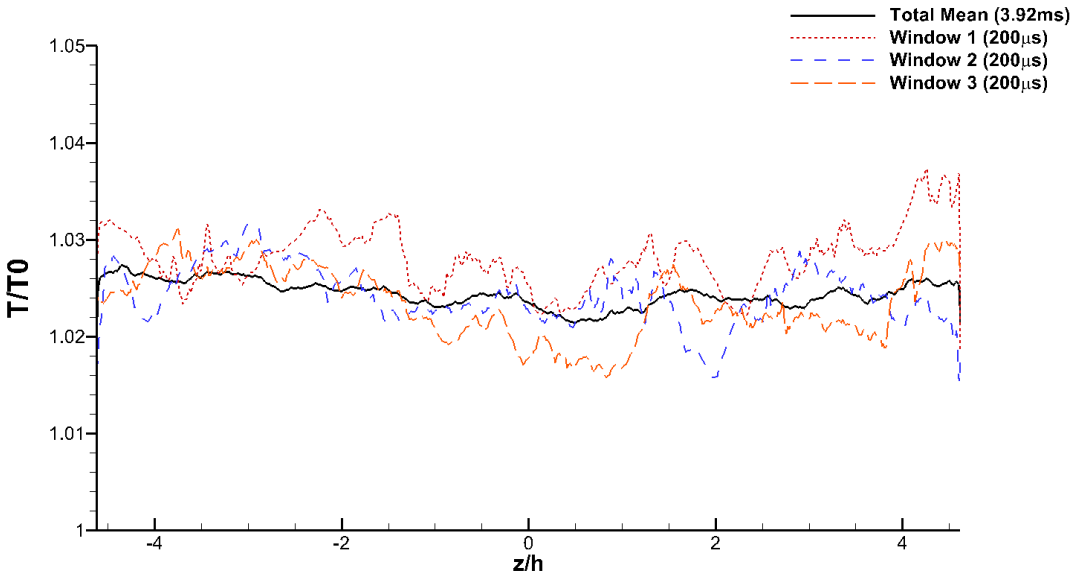


(a) 55 SLPM

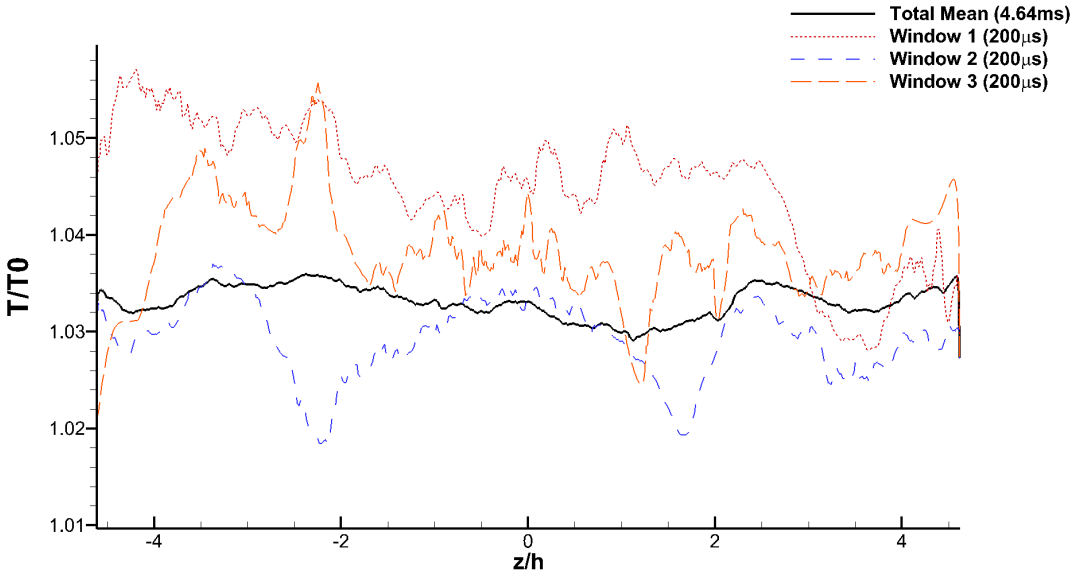


(b) 70 SLPM

**Figure 49. Spanwise variation along line 3 of mean temperature of both injection rates. Solid lines are the time-average for the complete simulation. Dashed lines are arbitrary 200 $\mu$s means.**

Line 4 was established as a location of interest after the 70 SLPM case was started, so it has less time simulated and there is only data for that injection rate. Figure 50 shows large, persistent spanwise inhomogeneities in the total mean corresponding to the same inhomogeneity seen earlier in the time-averaged contours of temperature. This is quantitative evidence that the spanwise homogeneity assumption is not valid.

Temperature is an incredibly important quantity to know when measuring for species concentrations, because radiation is proportional to $T^4$. However, because this is a non-reacting flow, the peak temperatures here are due only to aerodynamic heating. This can be significant, but combustion will be the largest effect on temperature in the combustor. To gain insight into how the combustor will behave once combustion starts, the equivalence ratio is examined on the same spanwise lines as temperature. Line 1 is disregarded as the fuel will not penetrate above and upstream of the cavity.

Figures 51a - 51b and 52a - 52b show the mean equivalence ratio of both injection rates for Line 2 and 3 respectively, and Figure 53 shows the equivalence ratio for Line 4 when injecting at 70 SLPM. The increase of fuel injection rate does not change the character of the fluctuations for any of the spanwise lines, only increasing the means around which the values fluctuate.

Looking at Line 2, the same observation of large numbers of small eddies being observed by the HSC on each interferogram window can be made. The fluctuations away from the mean; however, are much larger in terms of magnitude (up to 50% of the mean values). The fuel is, in the mean, evenly distributed over the shear layer.

Line 3 again shows fewer and larger fluctuations. The difference between the windowed means and the total mean tends to be much larger for equivalence ratio than the temperature, and there is some persistent spanwise inhomogeneity in the cavity where fuel fails to penetrate into the corners on both walls. This results in

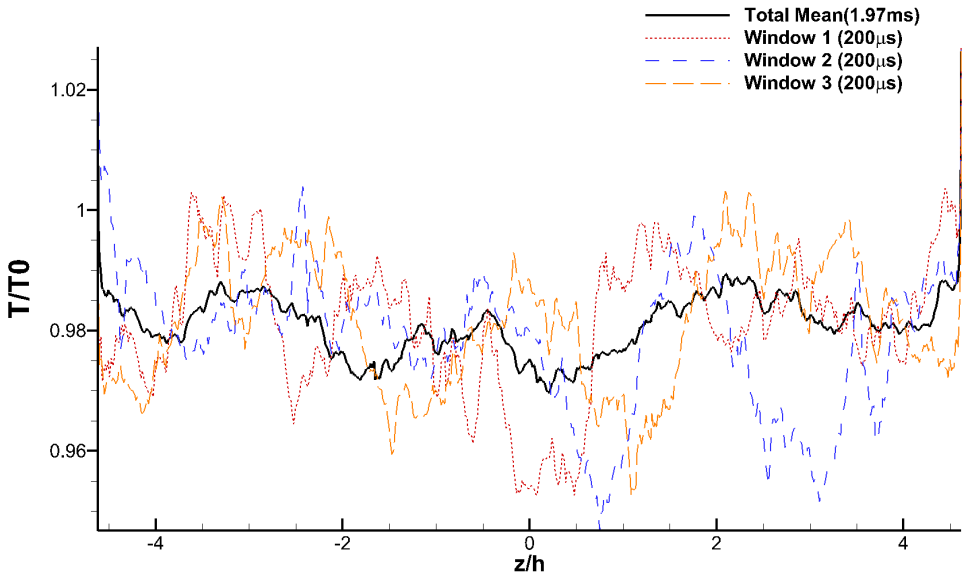


**Figure 50. Spanwise variation along line 4 of mean temperature with 70 SLPM injection. Solid line is time-average for complete simulation (1.97 $ms$). Dashed lines are arbitrary 200 $\mu$s means.**

about 15% lower equivalence ratio in the cavity corners than near the midplane.

Line 4 once again shows the most span inhomogeneity, with three peaks spread across the span. These peaks correspond with the three lobes of fuel discussed earlier in the qualitative analysis. Some window means see as much as a 100% difference from the total mean of equivalence ratio. This, coupled with the fewer, larger structures that exist in the low local Reynolds number flow in the cavity leads to questions about whether the timescales involved with the turbulent features are on the order of the each 200$\mu$s scan.

For this reason, time autocorrelations were taken for each line using the time histories of three points per line; two in the near-wall region, and one at the midspan. An example of this is shown in Figure 54.

The four lines see very disparate time scales due to experiencing much different turbulent features. Figures 55a - 55d demonstrate this clearly through the temporal autocorrelation functions calculated for three points along each of the four spanwise

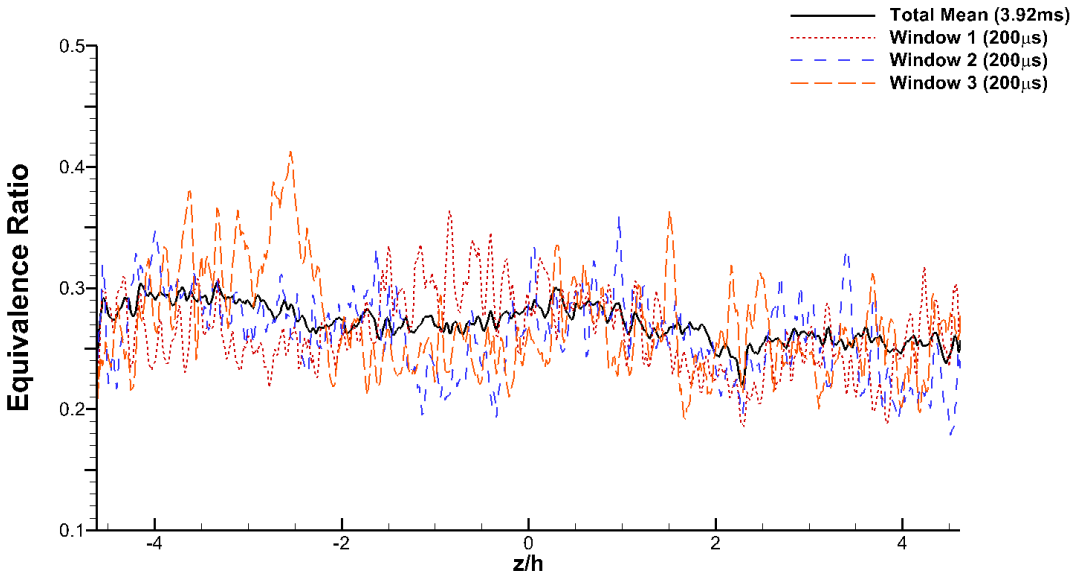


(a) 55 SLPM

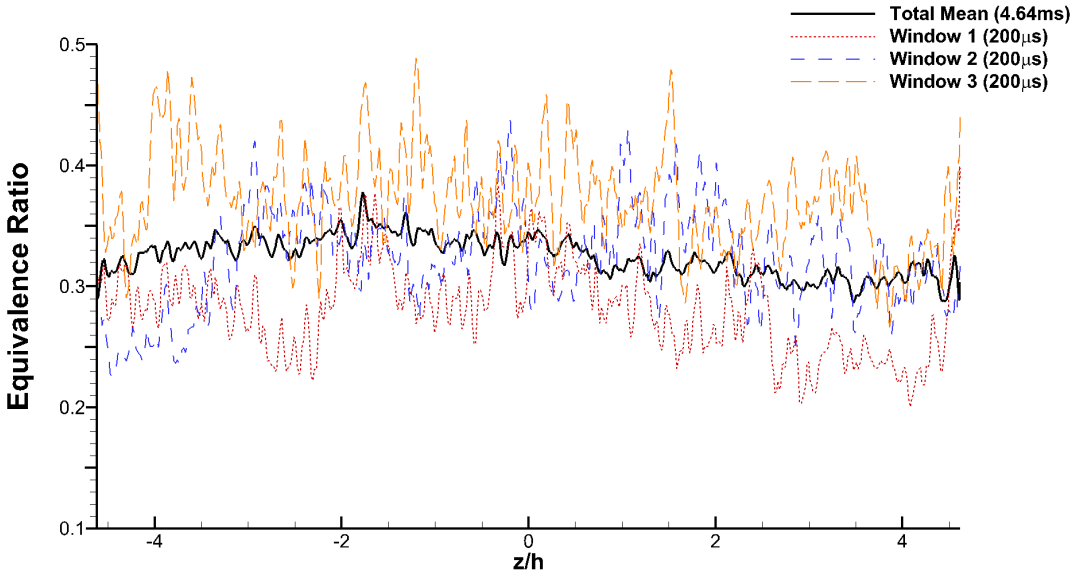


(b) 70 SLPM

**Figure 51. Spanwise variation along Line 2 of mean equivalence ratio of both injection rates. Solid lines are the time-average for the complete simulation. Dashed lines are arbitrary 200 $\mu$s means.**

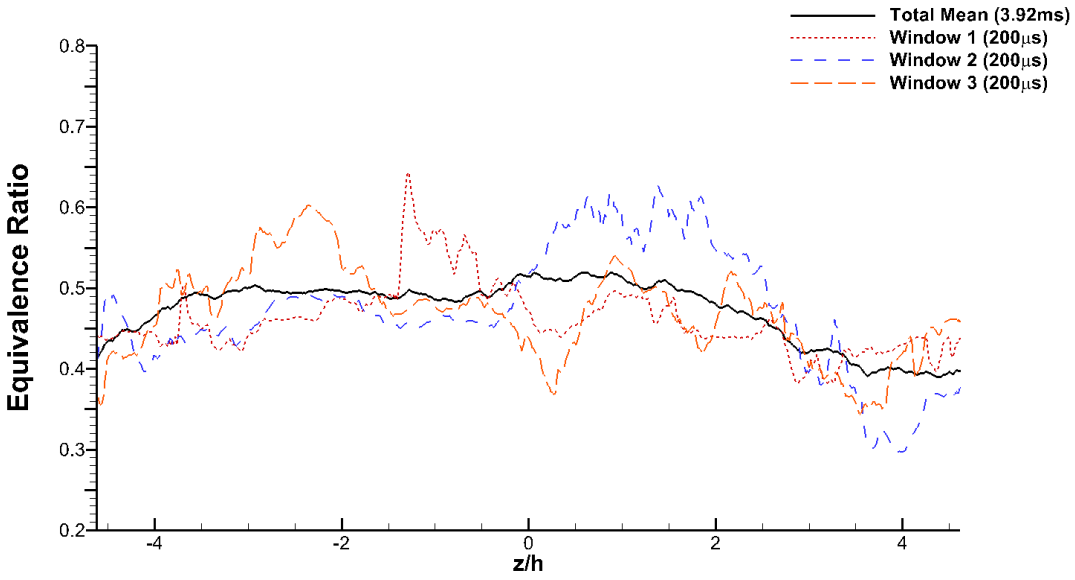


(a) 55 SLPM

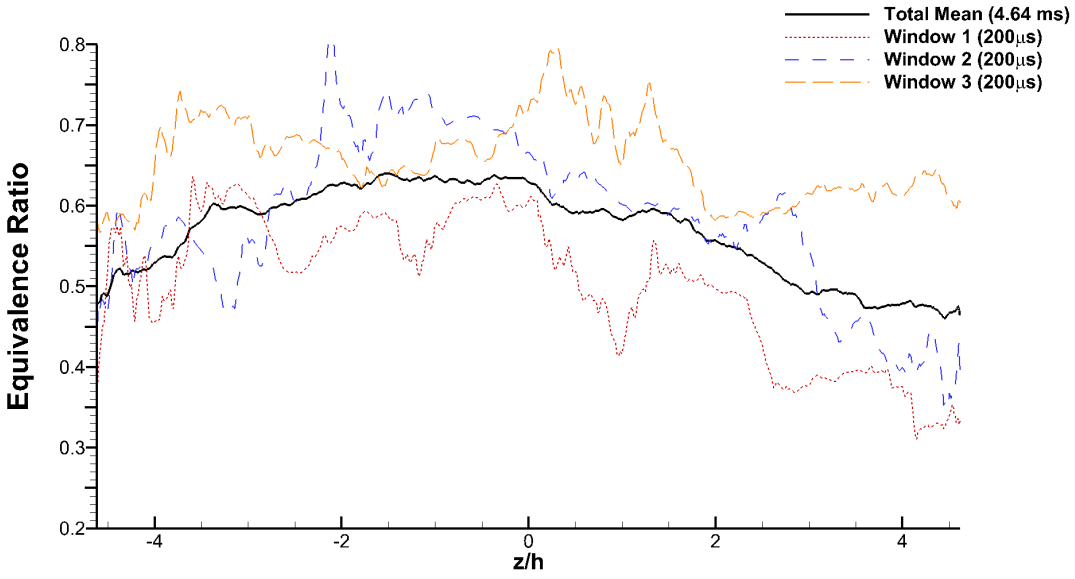


(b) 70 SLPM

**Figure 52. Spanwise variation along Line 3 of mean equivalence ratio of both injection rates. Solid lines are the time-average for the complete simulation. Dashed lines are arbitrary 200 $\mu$s means.**

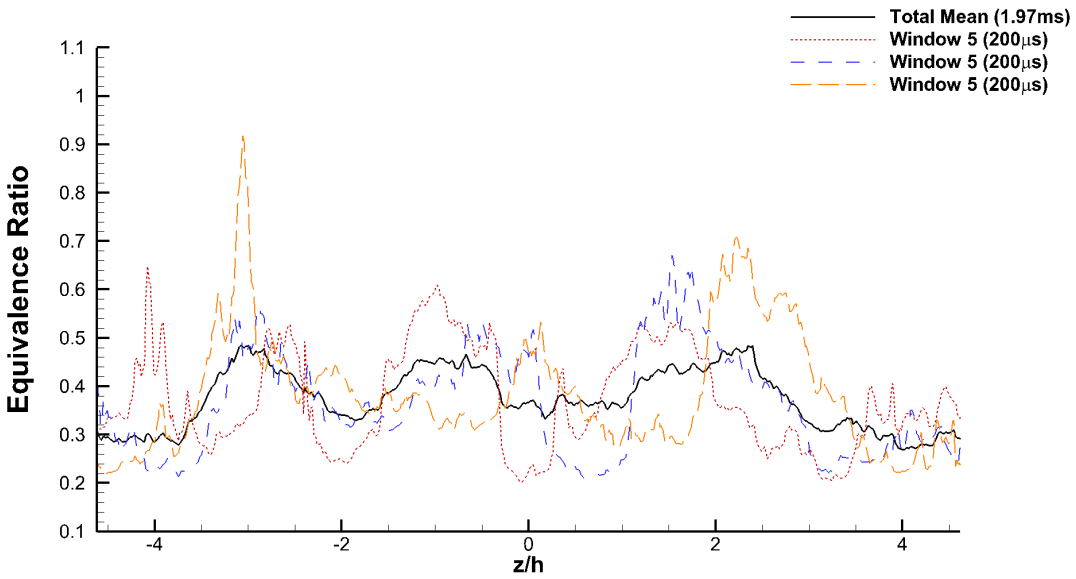


**Figure 53. Spanwise variation along line 4 of mean equivalence ratio with 70 SLPM injection. Solid line is time-average for complete simulation ($1.97ms$). Dashed lines are arbitrary 200 $\mu$s means.**

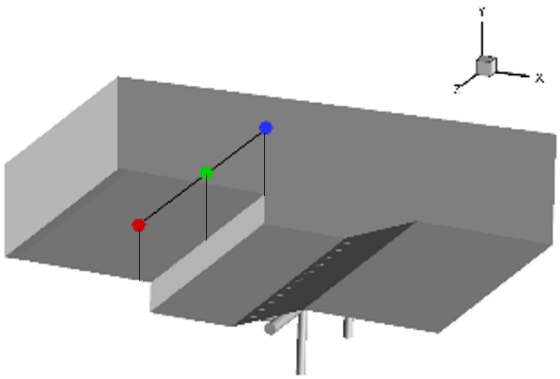

**Figure 54. Example line displaying the locations of the points used to calculate the time autocorrelations.**

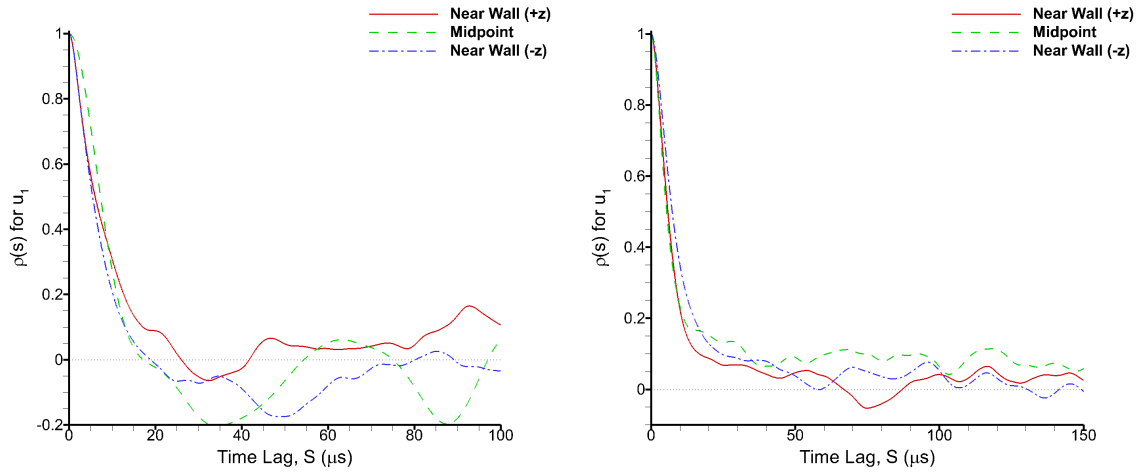


(a) Line 1




(b) Line 2

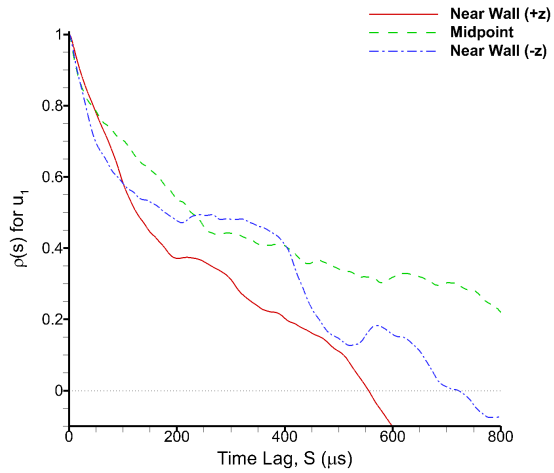


(c) Line 3

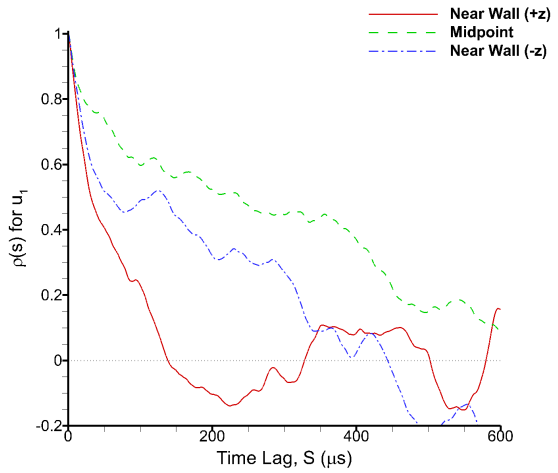


(d) Line 4

**Figure 55. Temporal Autocorrelation Function using velocity in three locations on lines 1-4. Each line has two locations in the sidewall boundary layers and one at the spanwise midpoint. This is done with the 70 SLPM injection case.**

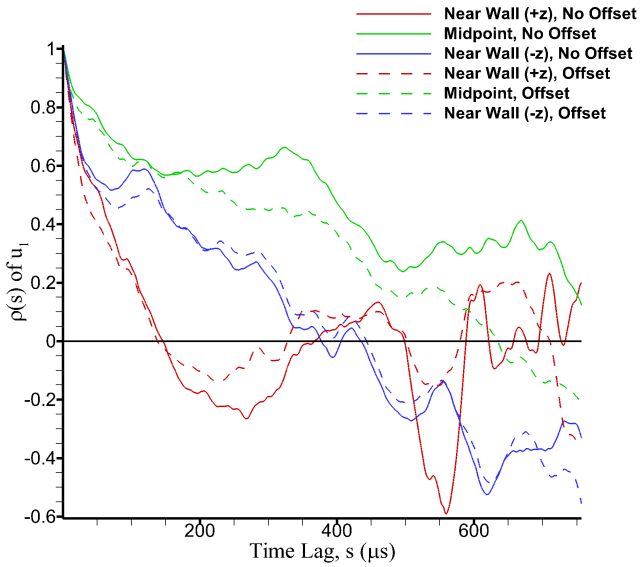


**Figure 56. Temporal Autocorrelation Function using velocity in three locations on line 4. Two windows of autocorrelation are included. Each line has two locations in the near-wall region and one at the spanwise midpoint. This is done with the 70 SLPM injection case.**

lines. Two of the points are in the sidewall boundary layers and one is at the midpoint of the line of sight. The integral time scales are approximated from these figures by integrating to the first zero crossing and then multiplying by a "safety factor" of 1.25. The safety factor is to ensure that the calculated timescale is large enough to separate highly correlated measurements as the turbulent features fluctuate in size slightly over time. The core flow and shear layer exhibit time scales on the order of 10$\mu$s, while the cavity sees an order of magnitude higher at 190$\mu$s, almost matching the collection time of 200 $\mu$s.

It is worth recalling that the the HSC is not really a time averaged view of the flow over its entire multi-second collection time, but rather a collection of images that contain multiple interferograms that are taken *sequentially*. This coupled with the knowledge of the timescales of the turbulent content in this regime raises questions on the repeatability of the hyperspectral camera measurements. During the 200$\mu$s

collection time, there has been sufficient time for the collection of many small eddies in the shear layer and, to a lesser extent, the core flow, however; only a few independent data points of the large structures responsible for transporting fuel and diffusing temperature in the cavity have been observed. The result could be highly correlated data between captures with statistics that are not actually stationary. Looking back at Table 1, one of the assumptions used in the HSI processing model is the scene is temporally constant. This is likely valid for a true time average, but because of the unique collection method discussed above, this assumption may not be applicable without careful ensemble averaging of the data.

Line 4 is unique in that the differences between the autocorrelation, and therefore the calculated integral timescales, at the two points in the near wall region are significantly different. This is unexpected considering that the cavity is symmetric in shape and the points in the near wall regions are expected to have similar turbulent timescales. This reinforces that the character of the turbulence is variable inside the cavity with respect to spanwise position, but more importantly that it could vary strongly with time on an order much larger than the turbulent scales. To examine this, Figure 56 shows the same time autocorrelation function as Figure 55d as well as a function calculated with an arbitrarily-chosen 0.6 $ms$ offset to the start of calculation. It appears, upon examination, that either 0.6 $ms$ isn't enough time to capture this long duration mode, or there is another cause for the large difference between "symmetric" features. Either way, more simulation time is desirable for this particular line examination.

These timescales can also be used to estimate if the resolution is sufficient to resolve the integral length scales. The smallest, fastest moving eddies will be in the shear layer, so those are of most interest. The average convective velocity in the shear layer is near 300 m/s. With each eddy being separated by approximately 10 $\mu$s, this

means the integral length scale is close to 3 $mm$. With an isotropic grid spacing of $2.5 \times 10^{-4}$, this means there is approximately 12 cells per integral length scale. The integral timescales of each line along with the number of cells per eddy are shown in Table 8. According to Davidson, there should be at least 2 cells per eddy, and it's best if there are 4 or more[47]. Clearly this requirement is exceeded by this resolution.

**Table 8. Integral Time Scales (midpoints)**

| Line | Timescale ($\mu$s) | Integral Length Scale (mm) | Cells/Eddy |
|---|---|---|---|
| 1 | 11 | 7.4 | 30 |
| 2 | 10 | 3.0 | 12 |
| 3 | 190 | 5.7 | 23 |
| 4 | 100-300 | 3.0-9.0 | 12-36 |

Figures 57a - 57d show the energy frequency spectrum plotted against wave number for each of the four lines. This was calculated by taking the fast Fourier transform (FFT) of the velocity fluctuations of the midpoints of each line. These lines represent the average transfer of energy from the largest scales of turbulence down to the small, universal scales. Some high-frequency content is lost from the IDDES SGS model, but the important mid-frequency content indicative of flows with high shear contributing to eddy development are present.

The previous analysis has shown that spanwise inhomogeneity exists in the fuel distribution in the combustor. The next step is to quantify the impact of the spanwise non-uniformity on the interpretation of the HSI. To analyze the possible effect that spanwise non-uniformity has on spanwise and ensemble averaged data, spanwise-averaged equivalence ratio is calculated in two distinct ways: The first is to approximate the method of HSI collection and interpretation, and the other is a simple computational comparison. The result of this calculation is the direct comparison of equivalence ratios that are computed from the ensemble averaged transmittances similar to the HSI collection process, and the time- and span-averaged transmittance

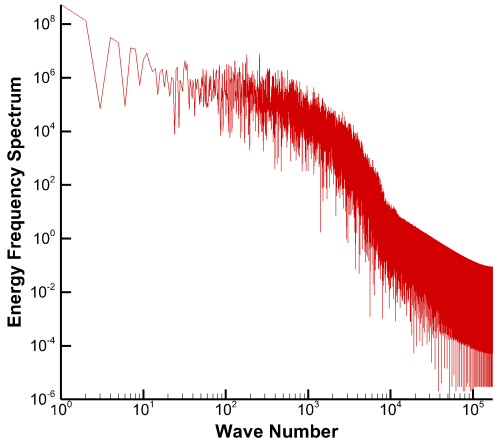


**(a) Line 1**

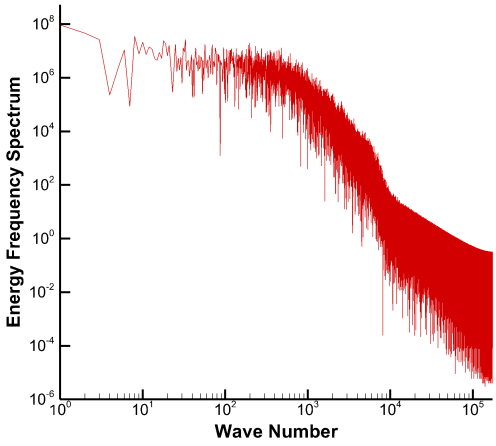


**(b) Line 2**

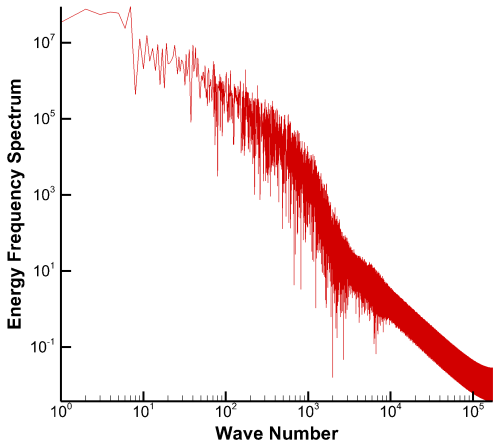


**(c) Line 3**

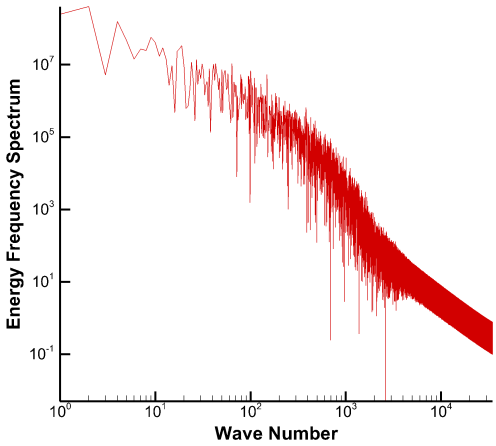


**(d) Line 4**

**Figure 57. Energy Frequency Spectrum of all four lines.**

directly available from the simulation. Transmittance is of special interest because when collecting photons from a black body radiator after passing through the cavity, the HSC is directly measuring transmittance of the gas between the camera and the black body. This calculation is designed to highlight what effect, if any, the non-linearity of the relationship between fuel number density and transmittance has on the post-processing of the HSI data when the spanwise uniformity assumption is violated. The nature of the non-linearity of the transmittance equations means that

$\langle\tau\rangle \neq e^{-\langle N\rangle\sigma l}$.

As a result of the temperature fluctuations being minimal in the span for the non-reacting case, $\sigma$ is assumed to be spanwise constant. For the HSI-surrogate calculation, the total time averaged methane number density, $\langle N\rangle$, is used to calculate the required value of $\sigma$ to achieve three transmittances corresponding to an optically "thin" (0.9), a "thick" (0.1), and a "balanced" (0.5) gas. This calculation is shown in Equation 35.

$$\sigma = \frac{-\ln(\tau_{prescribed})}{\sum_i N_i s_i} \tag{35}$$

The summation over $i$ is over all cells in the spanwise line, not a summation over species. The resulting values of $\sigma$ are then used to calculate the transmittances of each windowed mean for all lines. The transmittances are then ensemble averaged and the number density of methane is backed out for each case using:

$$N = \frac{-\ln(\tau)}{\sigma l} \tag{36}$$

The number density is then used to calculate equivalence ratios. The maximums, minimums, and standard deviations (SD) from the span average are compared for each window. Line 1 is not included due to the lack of fuel in that part of the combustor.

The results of the transmittance calculations are shown in Table 9. All calculations are using data from the 70 SLPM simulations. The difference between all of the backed-out and the span averaged number densities is negligible, with the max percentage difference being approximately 1.6%. This shows that the spanwise variation in the non-reacting case does not cause a significant difference in the observed transmittance resulting from the transmission of light through the regions with mixing. This indicates that, for the non-combusting case, the assumption of spanwise

**Table 9. Transmittance Calculations**

| | Enforced $\tau$ | Ensembled $\tau$ | Backed-out N (E+24) | Span Avg'd N (E+24) | Backed-Out $\phi$ | Span Avg'd $\phi$ |
|---|---|---|---|---|---|---|
| **Line 2** | 0.9 | 0.9001 | 0.2749 | 0.2728 | 0.3244 | 0.3221 |
| | 0.5 | 0.5014 | 0.2741 | 0.2728 | 0.3236 | 0.3221 |
| | 0.1 | 0.1027 | 0.2721 | 0.2728 | 0.3212 | 0.3221 |
| **Line 3** | 0.9 | 0.9001 | 0.4500 | 0.4438 | 0.5669 | 0.5577 |
| | 0.5 | 0.5017 | 0.4485 | 0.4438 | 0.5650 | 0.5577 |
| | 0.1 | 0.1033 | 0.4444 | 0.4438 | 0.5598 | 0.5577 |
| **Line 4** | 0.9 | 0.9006 | 0.2901 | 0.2867 | 0.3719 | 0.3667 |
| | 0.5 | 0.5022 | 0.2899 | 0.2867 | 0.3717 | 0.3667 |
| | 0.1 | 0.1018 | 0.2896 | 0.2867 | 0.3712 | 0.3667 |

| | Enforced $\tau$ | Stdev | Min $\phi$ | Max $\phi$ |
|---|---|---|---|---|
| **Line 2** | 0.9 | 0.052392 | 0.160976 | 0.522257 |
| | 0.5 | 0.052362 | 0.160976 | 0.522257 |
| | 0.1 | 0.052350 | 0.160976 | 0.522257 |
| **Line 3** | 0.9 | 0.098200 | 0.287355 | 0.815014 |
| | 0.5 | 0.098050 | 0.287355 | 0.815014 |
| | 0.1 | 0.097820 | 0.287355 | 0.815014 |
| **Line 4** | 0.9 | 0.103041 | 0.200062 | 0.917314 |
| | 0.5 | 0.103033 | 0.200062 | 0.917314 |
| | 0.1 | 0.103014 | 0.200062 | 0.917314 |

uniformity has no appreciable effect on the accuracy of the measurement.

The difference in transmittance makes little difference on the observed standard deviations. There is significant variation from window to window on every line, with the standard deviations ranging from $15.5 - 27.0\%$ of the mean values. Achieving good agreement on the spanwise mean is important; however, combustion is a three dimensional process and only accurately predicting the mean in a two-dimensional plane may not be sufficient in understanding the combustion in a scramjet. This is evident when looking at the statistics for Line 4, where the maximum equivalence ratio seen in the windowed means is more than five standard deviations away from the total mean.

The above observations are only applicable to the non-reacting case. Once com-

bustion is started, transmission will not be the only source of observed radiance, and much larger temperature gradients will exist in the cavity. In addition to introducing a temperature-sensitive emission calculation, this will invalidate the assumption that the attenuated cross section is uniform in the span of the cavity. Furthermore, the increased temperature variation in the cavity will directly effect the density variations through the equation of state. The density directly contributes to the observed transmission. These added factors will contribute more to HSI interpretation error than just the spanwise non-uniformity of fuel distribution. This method also shows that, while some concern existed over the timescales in the cavity being on the same order of the collection process, the proper handling of post-processing alleviates this issue. The ensemble averaging of a sufficient number of measurements should converge towards the time-average.

It is difficult to accurately predict the effect spanwise non-uniformity of equivalence ratio in the non-reacting case will have on the temperature in the cavity once burning is started, as combustion will effect the velocity fields and therefore the distribution of fuel. Estimating flame temperature with the assumption that the velocity field does not significantly change once combustion is initiated can still be useful to obtain qualitative knowledge of the possible resulting temperature distributions. Using NASA's Chemical Equilibrium with Applications (CEA) software to calculate adiabatic flame temperatures for the spanwise averaged, minimum, and maximum equivalence ratios displayed in Table 9 results in the flame temperatures shown in Table 10[49].

**Table 10. Flame Temperatures based on Equivalence Ratios**

| | Span Avg'd $T_f$ (K) | Min $T_f$ (K) | Max $T_f$ (K) |
|---|---|---|---|
| **Line 2** | 1123 | 741.1 | 1535.19 |
| **Line 3** | 1602 | 1045 | 2032 |
| **Line 4** | 1220 | 838.9 | 2162 |

It is clear from these projected temperatures that a combusting scramjet with a qualitatively similar flowfield to the observed non-reacting case will experience large gradients in temperature. At these temperatures, observed radiance from emitting particles will make up a much larger proportion of the total collected radiance because of radiation's non-linear dependence on temperature. The assertion that the existing spanwise inhomogeneity has little effect on HSI measurements that is possible in the non-reacting case is untenable without similar analysis of a combusting scramjet.

# V. Conclusion

**Summary.**

A full span, non-combusting scramjet cavity flameholder was simulated using Improved Delayed Detached-Eddy Simulation while injecting methane at two different rates. The results were compared to previous simulations as well as experimental PIV measurements to gain confidence in the methodology. Instantaneous data was compared to time-averaged data to determine if large-scale inhomogeneous features persist in the mean. Spanwise lines were established and complete time histories were recorded at these locations. Both total means and means of 200 $\mu$s windows were evaluated on these spanwise lines and some spanwise inhomogeneity was present when time-averaged. Temporal autocorrelations were calculated on the spanwise lines at several points along the lines. Vast differences in integral timescales exist depending on where in the domain the line is established. In the core flow and shear layer, the eddy timescales are fast enough that many eddies are accounted for in each interferogram recorded by the HSC; however, in the cavity recirculation only a few are recorded. A transmittance sensitivity test is conducted to examine what effects the observed spanwise uniformity assumption has on the interpretation of the hyperspectral measurement. Emission of the fuel is neglected as well as the effect of temperature on the attenuation cross section. While the non-reacting case seems to show very little sensitivity even when dealing with the non-linear equation for transmittance, once combustion is initiated these assumptions will be invalid and this evaluation will not accurately reflect a combusting flowfield.

**Initial Questions Answered.**

- Is the spanwise homogeneous assumption used by the experimental model valid?

- As a whole, approximating a non-reacting scramjet cavity flameholder as two-dimensional would be neglecting critical turbulent features that control the transport of important primitives, such as temperature and fuel density. While the HSI measurement of the non-combusting case does not exhibit strong sensitivity to this spanwise non-uniformity, the method used to test it do not include temperature's effect on the transmittance or any contribution from emission. These effects are non-negligible in a combusting environment.

- Are there specific regions of the domain in which the spanwise homogeneous assumption is valid?

  - While the 2D model is globally a poor representation of the scramjet combustor, there are certain locations in the *non-reacting* case, namely the shear layer and core flow, that the distribution of temperature and equivalence ratio are reasonably approximated by a 2D assumption. This is subject to change under the extreme heat release once combustion starts as, some low order calculations showed that the potential flame temperature could be on the order of 2100 K, with the difference between the maximum and minimum temperatures along a spanwise line of sight on the order of 1300 K.

- How do the timescales in the cavity affect the experimental data gathering and processing?

  - The HSC is not a true time average of the flow, but rather a collection of short time averages, all capturing at different wavelengths. The integral time scales of the turbulent eddies in the core flow and shear layer are short (about 10$\mu$s), and therefore many eddies will be captured at each

wavelength in this region. On the other hand, the time scales in the cavity are on the same order as the collection time for each mirror position (around $100 - 300\mu$s). This means that each interferogram may record one or two instances of uncorrelated data. When collecting data that are not truly instantaneous, typically you want a time-average that contains many time-independent samples that are resistant to low-frequency changes in the overall character of the flow. This ensures that the experiment is repeatable and correctly representative of the flow features. In addition to the vastly different timescales between spanwise lines in the cavity, Line 4 demonstrated significant timescale differences between the near-wall points. This could be an indication of very long period fluctuations that affects the smaller scale turbulent features, but if true, the timescale was too large for the amount of data collected in this type of simulation.

- Are there additional assumptions in the experimental model that are not valid?
  - The data that lead to the skepticism of HSC repeatability also calls into question another assumption in the experimental model, namely that the scene is temporally constant. While this is likely true when considering the actual flow through the scramjet cavity, what the HSC sees is actually a collection of short time-averaged data. As stated before, the features in the cavity have a long integral time scale (around 100-190$\mu$s, and on the order of the scan times) and the result may be that the data gathered here are not statistically stationary if not handled correctly. With ensemble averaging of a sufficient number of datasets, the non-reacting HSI observations can be used with confidence that the interaction of the long timescales in the cavity and the HSC scans is negligible.

**Research Significance.**

This one of very few full Reynolds number, complete geometry Hybrid-RANS/LES simulations performed of the scramjet RC-19 geometry. This also includes injection of fuel and analysis of the spanwise character of the domain. In addition to examining the assumptions of the model used to interpret this powerful flow examination tool, this study provides an initial examination of HSI accuracy and preliminary data that will help refine the model to produce more accurate information of the flow in question.

**Conclusions.**

The use of Improved Delayed Detached-Eddy Simulation produces closely matched velocity field predictions to similar experimental PIV measurements. The assumption of two-dimensionality of a non-reacting scramjet cavity flameholder with fuel injection does not hold up to scrutiny when examined with high-fidelity computational fluid dynamics. There are several locations in the flowfield that could be approximated as two-dimensional, but in the cavity, where the majority of fuel transport occurs, the assumption breaks down. In the case of the non-combusting scramjet cavity flameholder, the HSI measurements are not particularly sensitive to the spanwise inhomogeneity in the cavity. The assumptions used in this analysis do not reflect the flowfield once combustion is started, however; so a full combustion study must be accomplished to observe what error may exist for a burning scramjet.

Also, the timescales of the turbulent content in the domain demonstrates large variation based on cavity position. This calls into question the repeatability of the HSC measurements, because, even though the shear layer and core flow both experience many fluctuations for each 200 $\mu$s interferogram calculation, the recirculation region only sees a couple at the most. This means that each wavelength capture is

not observing a statistically stationary flow and differences between total flowfield measurements taken at different times could be statistically different. In addition, line 4 showed that there could be very large scale, long period character in the cavity that is not easily captured by these time-restricted simulation methods. The line had a significant difference in timescales between the near-wall points, where every other line had shown near-symmetry between the walls when considering timescales. Further analysis showed that the measurements are repeatable and a time-averaged result can be replicated so long as a sufficient number of observations are ensemble averaged.

**Future Work.**

Now that more confidence has been established in the HSI measurement and interpretation method, simulations of combustion of real system fuels, such as ethylene, should be performed. This would allow direct comparisons to be made to the experimentally-derived data as well as the analysis of the effect of heat release on HSI measurements. The effect of corner flow on boundary layer development before the cavity is also of some interest, especially when considering the recent work on the quadratic constitutive relations[50] where it has been shown that LES does not properly capture turbulent eddy development in corners. Side wall boundary layer adjacent to the free shear layer are directly dependent on the corner flows in the isolator and the expansion region of the combustor, this could have a significant effect on the spanwise character in the shear layer.

# Bibliography


1. Kevin C. Gross, Jeffrey R. Komives, Amy Kerst, and Evan P. Oren. Investigation of a Scramjet Flowfield with Hyperspectral Imaging Augmented by Large Eddy Simulation. In *53rd 3AF International Conference on Applied Aerodynamics*, 2018.

2. Sergio Pirozzoli and Matteo Bernadini. *Supersonic Turbulent Boundary Layers - DNS Database Up To RE=1110.*, 2011.

3. David Thompson, Eduardo Latorre Iglesias, Xiaowan Liu, Jianyue Zhu, and Zhiwei Hu. Recent Developments in the Prediction and Control of Aerodynamic Noise from High-speed Trains. *International Journal of Rail Transportation*, 3:1–32, Jun 2015.

4. David Wilcox. *Turbulence Modeling for CFD*. DCW Industries, La Canada, CA, 3rd edition, 2006.

5. Jiri Blazek. *Computational Fluid Dynamics: Principles and Applications*. Elsevier, Waltham, MA, 3rd edition, 2005.

6. David M. Peterson and Ez A. Hassan. Hybrid Reynolds-Averaged and Large-Eddy Simulations of a Supersonic Cavity Flameholder. In *55th AIAA Aerospace Sciences Meeting*, pages 1–20, January 2013.

7. R. A. Baurle. Hybrid Reynolds-Averaged/Large-Eddy Simulation of a Scramjet Cavity Flameholder. *AIAA Journal*, 55:1–17, 2016.

8. David M. Peterson and Ez A. Hassan. Implicit Large-Eddy Simulation of a Supersonic Cavity. In *55th AIAA Aerospace Sciences Meeting*, January 2017.

9. A. Kerst, K.C. Gross, E.P. Oren, and J.R Komives. Preliminary Investigation of a Scramjet Flowfield with Hyperspectral Imaging Augmented by Large Eddy Simulation. In *33rd AIAA Aerodynamic Measurement Technology and Ground Testing Conference*, June 2017.

10. S. Tuttle, M. Hsu, and C.D. Carter. Particle Image Velocimetry in a Nonreacting and Reacting High-Speed Cavity. *Journal of Propulsion and Power*, 30:579–591, May-June 2014.

11. A.D. Gardner, K. Hannemann, A. Paull, and J. Steelant. Post Flight Analysis of the HyShot Supersonic Combustion Flight Experiment in HEG. In *Proceedings of the Fifth European Symposium on Aerothermodynamics for Space Vehicles*, page 535, February 2005.

12. M.K. Smart, N.E. Hass, and A. Paull. Flight Data Analysis of the HyShot 2 Scramjet Flight Experiment. *AIAA Journal*, 44:2366–2375, October 2006.

13. Stephen R. Turns. *An Introduction to Combustion, Concepts and Applications*. McGraw Hill Education, 3rd edition, 1996.

14. Leslie A. Smith, Timothy Ombrello, and N. Sebastian Ohkovat. The Effect of Pulsed Injection on the Entrainment into a Cavity Based Flameholder in Supersonic Flow. In *55th AIAA Aerospace Sciences Meeting*, 2017.

15. M.T. Landhal and E Mollo-Christensen. *Turbulence and Random Processes in Fluid Mechanics*. Cambridge University Press, 2nd edition, 1992.

16. Stephen B. Pope. *Turbulent Flows*. Cambridge University Press, Cambridge, UK, 2000.

17. J.C. Rotta. Turbulent Boundary Layers in Incompressible Flow. *Progress in Aerospace Sciences*, 2(1):1–95, Jan 1962.

18. H. Schlichting and K. Gersten. *Boundary Layer Theory.* Springer, 9th edition, 2017.

19. Dean R. Chapman. Computational Aerodynamics Development and Outlook. *AIAA Journal, Vol. 17*, pages 1293–1313, 1979.

20. P.R. Spalart, W.H. Jou, M. Strelets, and S.R. Allmaras. Comments on the Feasibility of LES for Wings, and on a Hybrid RANS/LES Approach. In *Advances in DES/LES, Proceedings of the 1st Air Force Office of Scientific Research International Conference on DNS and LES*, January 1997.

21. Stephen B. Pope. Ten Questions Concerning the Large-eddy Simulation of Turbulent Flows. *New Journal of Physics*, 6, 2004.

22. J. Smagorinsky. General Circulation Experiments with the Primitive Equations. *Monthly Weather Review*, 91, March 1963.

23. U. Schumann. Subgrid Scale Model for Finite Difference Simulations of Turbulent Flows in Plane Channels and Annuli. *Journal of Computational Physics*, 18, 1975.

24. A.W. Vreman. An Eddy-Viscosity Subgrid-scale Model for Turbulent Shear Flow: Algebraic Theory and Applications. *Physics of Fluids*, 16, October 2004.

25. J.W. Deardorff. Three-Dimensional Numerical Study of the Height and Mean Structure of a Heated Planetary Boundary Layer. *Boundary Layer Meteorology*, 7:81–106, 1974.

26. D.K. Lilly. The Representation of Small-scale Turbulence in Numerical Simulation Experiments. *IBM Scientific Computing Symposium on Environmental Sciences*, 1967.

27. S.K. Robinson. Coherent Motions in the Turbulent Boundary Layer. *Annual Review of Fluid Mechanics*, 23, January 1991.

28. P. Spalart. Detached-Eddy Simulation. *Annual Review of Fluid Mechanics*, 41:181–202, 2008.

29. Russel M. Cummings, William H. Mason, Scott A. Morton, and David R. McDaniel. *Applied Computational Aerodynamics: A Modern Engineering Approach*. Cambridge University Press, May 2018.

30. P.R. Spalart, S. Deck, M.L. Shur, K.D. Squires, M.Kh. Strelets, and A. Travin. A New Version of Detached-eddy Simulation, Resistant to Ambiguous Grid Densities. *Theoretical and Computational Fluid Dynamics*, July, 2006.

31. Soshi Kawai and Johan Larsson. Wall-modeling in Large Eddy Simulation: Length Scales, Grid Resolution, and Accuracy. *Physics of Fluids*, 24(1), 2012.

32. Mikhail L Shur, Philippe R Spalart, Mikhail Kh Strelets, and Andrey K Travin. A Hybrid RANS-LES Approach with Delayed-DES and Wall-modelled LES Capabilities. *International Journal of Heat and Fluid Flow*, 29(6):1638–1649, 2008.

33. Sebastian Okhovat, Timothy Ombrello, and Michael I. Resor. Radiance of Select Species in a Scramjet Cavity. In *55th AIAA Aerospace Sciences Meeting*, pages 1–9, January 2017.

34. K. Busa, B. Rice, and J. et al. McDaniel. Direct Measurement of Combustion Efficiency of a Dual-mode Scramjet via TDLAS and SPIV. In *53rd AIAA Aerospace Science Meeting*, 2015.

35. K.C. Gross, K.C. Bradley, and G.P. Perram. Remote Identification and Quantification of Industrial Smokestack Effluents via Imaging Fourier-Transform Spectroscopy. *Environmental Science and Technology*, page 93909397, November 2010.

36. M.R. Rhoby, D.L. Blunck, and K.C. Gross. Mid-IR Hyperspectral Imaging of Laminar Flames for 2-D Scalar Values. *Optics Express*, September 2014.

37. J.L. Harley, D.L. Blunck, B.A. Rankin, J.P. Gore, and K.C. Gross. Imaging Fourier-transform Spectrometer Measurements of a Turbulent Nonpremixed Jet Flame. *Optics Letters*, 39:2350–2353, 2014.

38. A.M. Kerst. Investigation of a Scramjet Flowfield Temperatures at the Boundary Layer with Hyperspectral Imaging. Master's thesis, Air Force Institute of Technology, June 2018.

39. D.M. Peterson and E.A. Hassan. Simulating Turbulence and Mixing in Supersonic Combustors Using Hybrid RANS/LES. In *53rd AIAA Aerospace Sciences Meeting*, January 2015.

40. Nicholas J. Georgiadis, Donald P. Rizzeta, and Christer Fureby. Large-Eddy Simulation: Current Capabilities, Recommended Practices, and Future Research. *AIAA Journal*, 48(8):1772–1784, 2010.

41. D.R. Gonzalez, A.T. Mohan, and D.V. Gaitonde. Overview of the Curvilinear Digital Filter Implementation in FDL3DICE. In *HFCMPL Report, The Ohio State University*, January 2017.

42. I. Nompelis, T. Drayna, and G. Candler. A Parallel Unstructured Implicit Solver for Hypersonic Reacting Flow Simulation. *17th AIAA Computational Fluid Dynamics Conference*, 2005.

43. I. Nompelis, T. Drayna, and G. Candler. Development of a Hybrid Unstructured Implicit Solver for the Simulation of Reacting Flows Over Complex Geometries. In *34th AIAA Fluid Dynamics Conference and Exhibit*, 2004.

44. Pramod Subbareddy and Graham Candler. A Fully Discrete, Kinetic-Energy Consistent Finite-Volume Scheme for Compressible Flows. *Journal of Computational Physics*, 228:1347–1364, 2009.

45. G. Candler, H.B. Johnson, I. Nompelis, P.K. Subbareddy, T.W. Drayna, and V.M. Gidzak. Development of the US3D Code for Advanced Compressible and Reacting Flow Simulations. In *53rd AIAA Aerospace Sciences Meeting*, 2015.

46. Stéphane Catris and Bertrand Aupoix. Density Corrections for Turbulence Models. *Aerospace Science and Technology*, pages 1–11, January 2000.

47. Lars Davidson. Large Eddy Simulations: How to Evaluate Resolution. *International Journal of Heat and Fluid Flow*, 30:1016–1025, October 2009.

48. W. A. McMullan. Spanwise Domain Effects on Streamwise Vortices in the Plane Turbulent Mixing Layer. *European Journal of Mechanics*, 6, October 2017.

49. R.A. Svehla. Transport Coefficients for the NASA Lewis Chemical Equilibrium Program. *NASA Technical Reports Server*, May 1995.

50. T. Leger, N. Bisek, and J. Poggie. Supersonic Corner Flow Predictions using the Quadratic Constitutive Relation. In *22nd AIAA Computational Fluid Dynamics Conference*, June 2015.

# REPORT DOCUMENTATION PAGE

*Form Approved*
*OMB No. 0704–0188*



| 1. REPORT DATE *(DD–MM–YYYY)* | 2. REPORT TYPE | 3. DATES COVERED *(From — To)* |
|---|---|---|
| 08–28–2018 | Master's Thesis | Aug 2016 — Aug 2018 |

**4. TITLE AND SUBTITLE**

THREE-DIMENSIONAL WALL EFFECTS IN A SCRAMJET CAVITY FLAMEHOLDER

**5a. CONTRACT NUMBER**

**5b. GRANT NUMBER**

**5c. PROGRAM ELEMENT NUMBER**

**6. AUTHOR(S)**

Evan P. Oren

**5d. PROJECT NUMBER**

**5e. TASK NUMBER**

**5f. WORK UNIT NUMBER**

**7. PERFORMING ORGANIZATION NAME(S) AND ADDRESS(ES)**

Air Force Institute of Technology
Graduate School of Engineering and Management (AFIT/EN)
2950 Hobson Way
WPAFB OH 45433-7765

**8. PERFORMING ORGANIZATION REPORT NUMBER**

AFIT-ENY-MS-18-S-068

**9. SPONSORING / MONITORING AGENCY NAME(S) AND ADDRESS(ES)**

Air Force Research Laboratory, Aerospace Systems Directorate, Hypersonic Sciences Branch
2130 Eight Street
WPAFB OH 45433-7542
Email: Michael.Brown.191@us.af.mil

**10. SPONSOR/MONITOR'S ACRONYM(S)**

AFRL/RQHF

**11. SPONSOR/MONITOR'S REPORT NUMBER(S)**

**12. DISTRIBUTION / AVAILABILITY STATEMENT**

DISTRIBUTION STATEMENT A:
APPROVED FOR PUBLIC RELEASE; DISTRIBUTION UNLIMITED.

**13. SUPPLEMENTARY NOTES**

**14. ABSTRACT**

Scramjets, or supersonic combustion ramjets, are a key component for the development of long duration hypersonic vehicles. A novel optical observation technique called hyperspectral imaging has been developed to examine a scramjet combustion chamber. The hyperspectral camera is capable of generating an interferogram at hundreds to thousands of wavelengths. These data are integrated across the line-of-sight with no information on three-dimensional location. A model must be used to translate this data to three dimensions. With no *a priori* data to inform otherwise, the current model assumes that the scramjet is two-dimensional in nature. This does not agree with understanding of compressible flow theory of shock dominated and turbulent flows. This work simulates a non-reacting scramjet combustor using hybrid RANS/LES. The spanwise character is analyzed through instantaneous and time-averaged statistics.

**15. SUBJECT TERMS**

Scramjet, Cavity Flameholder, Turbulence, Spectroscopy, Hyperspectral Imaging (HSI), Computational Fluid Dynamics (CFD), Improved Delayed Detached Eddy Simulation (IDDES), Hybrid RANS/LES, Hypersonics

| 16. SECURITY CLASSIFICATION OF: | | | 17. LIMITATION OF ABSTRACT | 18. NUMBER OF PAGES | 19a. NAME OF RESPONSIBLE PERSON |
|---|---|---|---|---|---|
| a. REPORT | b. ABSTRACT | c. THIS PAGE | | | Maj Jeffrey Komives, AFIT/ENY |
| U | U | U | U | 114 | 19b. TELEPHONE NUMBER *(include area code)* (937)656-0850; evan.oren.1@us.af.mil |

**Standard Form 298 (Rev. 8–98)**
**Prescribed by ANSI Std. Z39.18**